Nonlinear Dynamics of Rotating Detonation Waves

James Koch

A dissertation

submitted in partial fulfillment of the

requirements for the degree of

Doctor of Philosophy

University of Washington

2020

Reading Committee:

Carl Knowlen, Chair

J. Nathan Kutz

Mitsuru Kurosaka

Program authorized to offer degree:

Aeronautics and Astronautics

University of Washington

Abstract

Nonlinear Dynamics of Rotating Detonation Waves

James Koch

Chair of the Supervisory Committee:
Carl Knowlen, Research Associate Professor
Aeronautics and Astronautics

The Rotating Detonation Engine (RDE) is a novel rocket combustor configuration that features a periodic, high aspect ratio (length of flowpath versus transverse thickness) combustion chamber designed to promote tangential high-frequency combustion instabilities typical of conventional rockets. Most RDEs are comprised of concentric cylinders whereby the annular gap between the cylinders constitutes the flow domain. The annular gap acts as geometric confinement suitable for robustly promoting the self-steepening of pressure and density gradients caused by combustion. The RDE's steady operation is the saturation of this highly nonlinear self-steepening process: a number of circumferentially traveling detonation waves. The benefits of the RDE include a larger stable operating envelope and potentially higher thermodynamic cycle efficiency over conventional rockets. However, the collective behavior of the detonation waves present in the RDE combustion chamber, while readily observable, is not well understood nor sufficiently characterized, especially with respect to engineering metrics such as thrust or engine stability. This dissertation is a comprehensive experimental, theoretical, and numerical study that aims to link observed the gasdynamic engine behavior to the nonlinear dynamics of the detonation waves.

The experimental test campaign features engines of two sizes: a 154-mm flowpath outer

diameter (OD) engine and a 76mm OD engine. A sweep of boundary conditions (inlet and outlet pressures) was conducted using the 154-mm RDE at reduced mass flux conditions to establish the engine's gasdynamic operating regimes, namely the attainment of a thermal choke at the exit of the annular duct. Similarly, using the 76-mm RDE at elevated mass flux conditions, the engine's response to the attainment of an axial thermal choke is investigated with respect to changes in total injection area. From both sets of testing, found is that the choked annular duct acts as a boundary condition that fixes the upstream pressure required to steadily deliver a given mass flow rate of propellant of a specified chemical energy potential.

By recording the space-time history of the detonation waves with a high speed camera, a diverse set of behavior was recorded and collected during the experimental test campaign. Such behavior includes wave nucleation, destruction, mode-locking of multiple waves, persistent wave modulation, and pulsating plane waves. By drawing upon the well-established fields of nonlinear waves and detonation analog modeling, a Rotating Detonation Engine analog system is proposed. This model system is an adaptation of the Majda detonation analog to a periodic domain with imposed dissipation and propellant regeneration. The dissipative process is constrained to enforce the same global behavior seen in experiments, namely the self-similar pressure operating profiles attained with a thermal choke point at the exit of the engine.

Within the reduced-scope of co-rotating detonation waves, the RDE analog system is found to qualitatively reproduce all transients and modes of operation seen in experiments. The propagating waves are classified as autosolitons, or localized structures with offsetting dominant balance physics. Within this context, the dominant balance physics are identified and found to be strongly influenced by input-output energy dynamics and act across several orders of spatial and temporal scales. In this manner, the global multi-scale balance physics give rise to the traveling detonation waves and their associated dynamics - not exclusively the frontal dynamics prescribed by classical detonation theory. Furthermore, the underlying fundamental Hopf bifurcation to time-periodic modulation of the collection of waves is confirmed to exist in the RDE analog. Comparisons between computed Hopf orbits of the model and experimentally-extracted kinematic traces are made showing good qualitative agreement.

Contents

List of Figures

List of Tables

Chapter 1

Introduction and Fundamentals

1.1 The Rotating Detonation Engine

Combustion instabilities are a universal phenomenon in aerospace propulsion systems. In rockets, combustion chambers can exhibit coupling between combustor geometry, propellant injection, and local heat release [17, 18, 19, 20, 21] which can lead to instabilities that are capable of inducing mechanical failure [22], constituting a major risk to the propulsion system. Historically, to abate this risk, significant resources have been devoted to engineer systems that damp or limit the mechanisms responsible for the formation of instabilities. These engineering tasks are not trivial: the physical processes responsible for the instabilities are highly nonlinear and intricately coupled, often making the unit processes inseparable. Consequently, the physics exploration of these nonlinearities is often constrained to hardware-specific studies.

The rotating detonation engine (RDE) (see Fig. 1.1) was first conceptualized as an alternative to standard rocket engine designs in the late 1950's to early 1960's [23, 24]. In the RDE, instead of the suppression of combustion instabilities, the combustion chamber was designed to leverage and promote a specific and ubiquitous instability which generated rotating combustion fronts whose growth produced a number of discrete co- and counter-propagating traveling detonation waves that consumed injected propellant. The RDE is therefore anomalous in that its steady operation is the saturation of a nonlinear combustion instability, namely the promotion of the self-steepening of the

pressure and density gradients caused by heat release in an annular combustion chamber. The collection of detonation waves travel in-sync with the coupled injection and exhaust processes.

However the RDE is not free from its own set of instabilities: the balance between the nonlinearity of the fluid medium and the competing physical processes of combustion, injection, and exhaust is delicate. Rotating detonation waves have experimentally been found to be very sensitive to combustor boundary conditions (such as inlet pressure and exit plane pressure), propellant heat release, and the geometric parameters of the engine, such as engine length and annulus circumference. For certain conditions, rotating detonation waves have been observed to exhibit a number of remarkable properties that differ significantly from the freely-propagating detonations of conventional theory. A prototypical detonation wave is a *front* that connects the states of unburnt and completely burnt mixture. Rotating detonation waves differ in that they are *pulses*, where the start and end states of the wave are the same. The 'tail' of the detonation decays as the burnt gas can expand perpendicularly to the propagation direction of the pulses. Likewise, at a particular point in the annulus, the reactant mixture is regenerated within the transit time of a wave. This balance of heat release (gain), exhaust processes (dissipation), propellant injection (gain recovery), and nonlinearity of the medium governs the pulse shape, number, and behavior [25]. Should these physical processes be unbalanced, spatially or temporally, a wide array of spatiotemporal dynamics are known to exist and persist, as observed in experiments and detailed computational studies. Such dynamics include mode-locking of pulses [25], modulation of the pulse train [25, 26], and bifurcations to different numbers of pulses [25, 27, 28, 26]. The physical mechanisms and engineering implications of these transients and instabilities are not well understood, especially with regard to operational stability and performance.

In this dissertation, investigated are the properties of these detonation waves with respect to the interplay of the physical unit processes that govern the pulse behavior. A brief review of literature regarding detonation theory, detonation dynamics, and combustor dynamics is given in the latter portion of this chapter. This study's research effort begins with a suite of experimental testing (Chapter 2) of two rotating detonation engines with respect to their inlet and outlet boundary conditions and their operating set points.

From experiments, dynamics across several spatial and temporal orders of magnitude are observed and presented, linking system-wide, large-scale steady operating profiles to the behavior of the fast-traveling detonation waves. From these observations, in Chapter 3 a reduced-order mathematical description is proposed that captures the coupling of the physical processes within the combustion chamber. The model properties are examined in Chapter 4. Found is that the collection of detonation waves exhibit solitonic properties in their interactions and balance physics. Within this context, presented is the *fundamental instability* of the rotating detonation wave, namely a Hopf bifurcation from the steadily propagating wave to the time-periodic wave modulation as seen in experiments. The engineering implications of the proposed model are discussed in the latter half of Chapter 4.

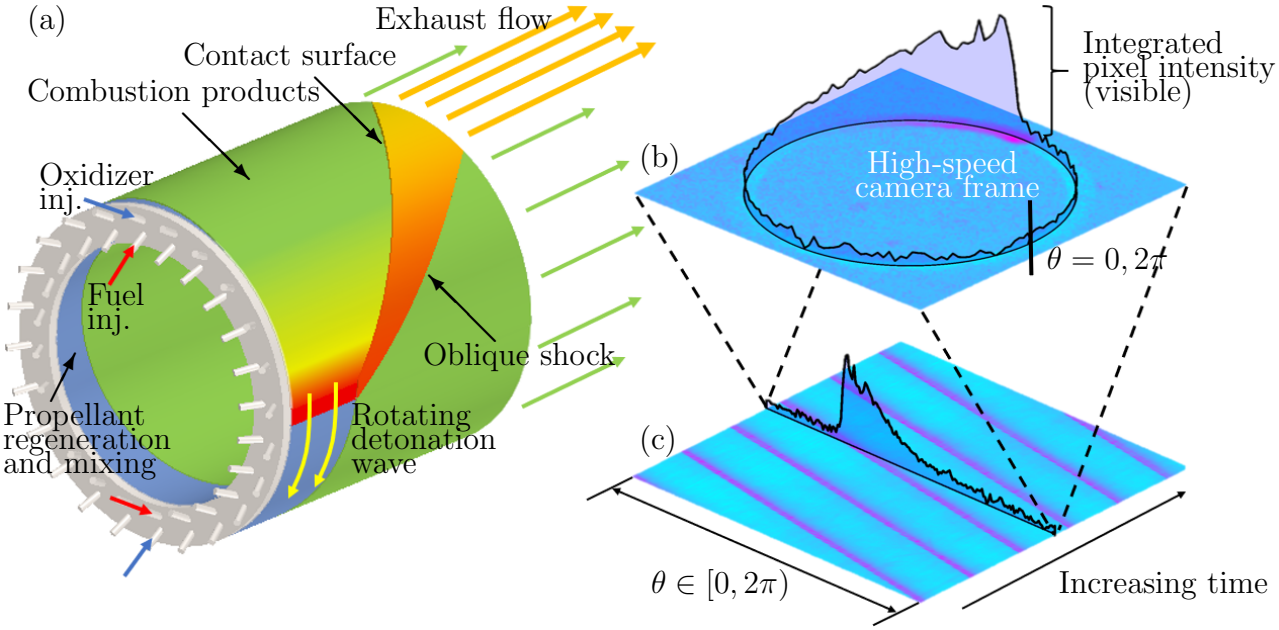

Figure 1.1: A sketch depicting the flowfield of the Rotating Detonation Rocket Engine is shown with the major features annotated. Gaseous fuel and oxidizer are injected through a number of discrete orifices that rapidly mix inside an annular combustion chamber. A supersonic, circumferentially-traveling, reaction wave consumes the newly-mixed propellant, sustaining the motion of the reaction wave. Emanating from this front is an oblique shock wave that sweeps the downstream flowfield. A contact surface marks the location separating the combustion products of this particular reaction front from those of other waves or, in this case, previous round-trips of the same wave. As the reaction front passes over the propellant injectors, the injectors become blocked, as the reaction wave pressure is typically higher than that of injection. A time lag therefore exists before propellant can be re-introduced to the combustion chamber. This time lag is depicted as distance behind the reaction front before the blue reactant zone reappears. Thrust is produced from expelling the hot exhaust products rearward at high velocity and by producing a time- and spatially- averaged high chamber pressure acting on a thrusting wall (in this cartoon, this is the injector face). In the experimental set-up of this study, direct optical access of the annulus allows for the complete space-time history of the detonation waves to be recorded with a high-speed camera. A single frame from an experiment is shown in (b) with the annulus integrated pixel intensity overlaid the annulus location. Stacking each high-speed camera frame gives (c), where line slopes correspond to wave speed. The integrated luminosity trace in (b) corresponds to the trace shown in (c).

1.2 The Detonation Phenomenon

A brief derivation of the detonation condition is provided here for the 1-D case. This derivation is based on the non-dimensionalization given in [29].

1.2.1 Jump Conditions

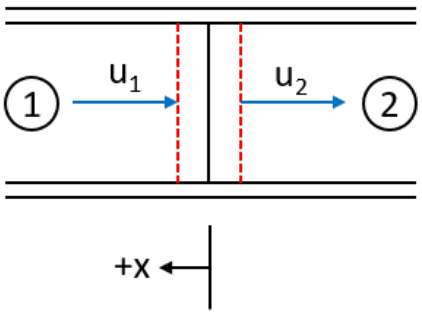

Figure 1.2: Control volume for the 1-D detonation formulation. The reference frame is fixed to the leading shock.

The jump conditions for a steady detonative process are derived from the continuity, momentum, and energy equations. Assume 1D, adiabatic, constant area duct flow with negligible body and viscous forces. Assume the fluid considered is calorically perfect and has a constant specific heat. States 1 and 2 are upstream and downstream of the steady detonation wave, respectively. The mass flux ($\frac{\dot{m}}{A}$) through the control volume (Figure 1.2) is defined as:

$$\frac{\dot{m}}{A} = \rho_1 u_1 = \rho_2 u_2, \tag{1.1}$$

where $\dot{m}$ is mass flow rate, A is the cross-sectional area of the domain, ρ is density, and u is velocity.

The conservation of momentum, given the assumptions, reduces to a balance of pressure forces and difference in momentum flux in the axial direction:

$$p_1 + \rho_1 u_1^2 = p_2 + \rho_2 u_2^2, \tag{1.2}$$

where p is pressure. Lastly, the energy balance is written using enthalpy (h) immediately:

$$h_1 + \frac{u_1^2}{2} + q = h_2 + \frac{u_2^2}{2}. \tag{1.3}$$

The heat release per unit mass between the two states is denoted by q. For closure, the equation of state for a perfect gas is given:

$$p = \rho RT, \tag{1.4}$$

where R is the specific gas constant and T is the fluid temperature.

1.2.2 Rayleigh Lines

Continue by substituting (1.1) into (1.2):

$$p_2 - p_1 = u_1^2 \rho_1^2 \left(\frac{1}{\rho_1} - \frac{1}{\rho_2} \right) = \frac{u_1^2}{v_1^2} \left(v_1 - v_2 \right), \tag{1.5}$$

where v is the specific volume $v = \frac{1}{\rho}$. This relationship is the locus of states satisfying both the conservation of mass and conservation of momentum. It is called a *Rayleigh Line*. An extra step is taken to non-dimensionalize this line:

$$\hat{v} = \frac{v_2}{v_1}$$

$$\hat{p} = \frac{p_2}{p_1}$$

$$M_1^2 = \frac{1 - \hat{p}}{\gamma \left(\hat{v} - 1 \right)} \qquad M_2^2 = M_1^2 \frac{\hat{v}}{\hat{p}}, \tag{1.6}$$

with Mach number introduced as $M = \frac{u}{u_{sound}} = u/\sqrt{\gamma RT}$. The non-dimensional form gives quick access to inlet and outlet Mach numbers for the control volume. In the $\hat{v}$-$\hat{p}$ plane for a fluid moving with positive velocity, (1.6) restricts the space of physical solutions to those of positive mass flux. Such regions in the $\hat{v}$-$\hat{p}$ plane are displayed in Figure 1.3.

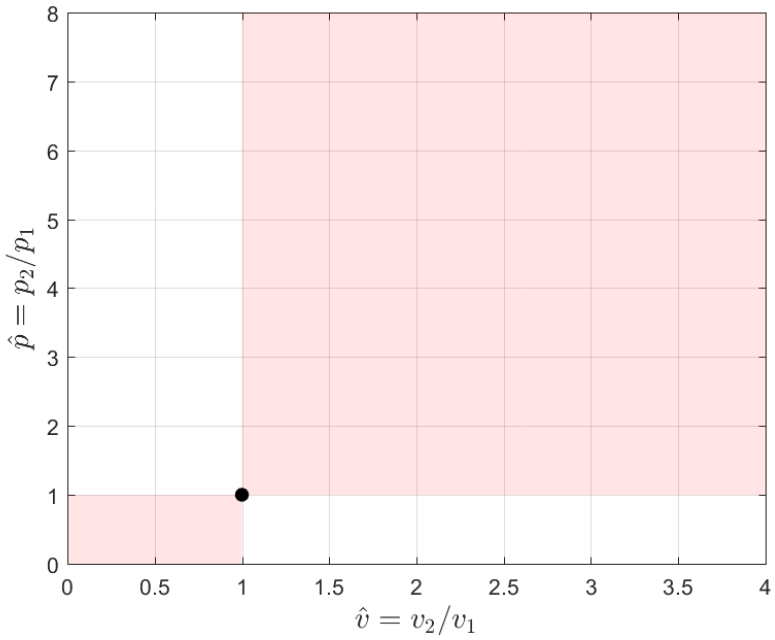

Figure 1.3: Regions of positive mass flux ($M_1 > 0$) in thermodynamic coordinates. State 1 is the point ($\hat{v} = 1, \hat{p} = 1$). Nonphysical regions are shaded in red.

1.2.3 Hugontiots

The Rayleigh relation is substituted into the energy equation to give an analogous curve satisfying the conservation of mass, momentum, and energy. After some algebra, this relation becomes:

$$h_2 - h_1 = (p_2 - p_1)\frac{v_1 + v_2}{2} - q \tag{1.7}$$

Invoking a calorically perfect gas argument ($h = c_p T$) and non-dimensionalizing:

$$\left(\hat{p} + \frac{\gamma - 1}{\gamma + 1}\right)\left(\hat{v} - \frac{\gamma - 1}{\gamma + 1}\right) = \frac{4\gamma}{(\gamma + 1)^2} + 2\hat{q}\left(\frac{\gamma - 1}{\gamma + 1}\right) \tag{1.8}$$

In this relationship, $\hat{q}$ is defined as $\hat{q} = (\rho_1/p_1)q$. In the thermodynamic plane, sets of these curves for given heat releases are shown in Figure 1.4.

1.2.4 Solutions

A process satisfying the aforementioned assumptions and jump conditions must lie on a Rayleigh Line and Hugoniot Curve. Therefore, solutions exist at their intersection(s).

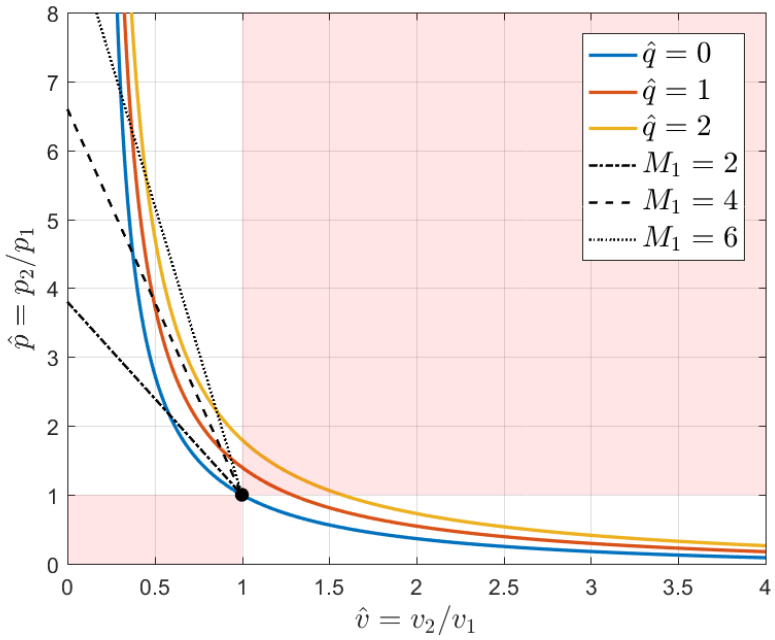

Figure 1.4: Example Hugoniot curves superimposed on thermodynamic plane with physical and non-physical regions. The portions of the Hugoniots passing through the shaded areas are not physically reachable. Two example Rayleigh Lines are also given. Intersections of a Rayleigh Line and Hugoniot are solutions to the 1-D jump conditions.

This solution is not unique. In Chapman's original paper [30], Chapman reasons that one must look for the detonation wave with minimal velocity, since there is no reason for a detonation wave to accelerate past this minimum attainable speed. From a geometric argument, one can see that the velocity minimum satisfying the Rayleigh and Hugoniot curves corresponds to the Rayleigh line tangent to a given Hugoniot, as shown in Figure 3. Enforcing the tangency requirement makes the steady, 1-D detonation problem unique and analytic. Such an example is given in Figure 1.5.

The point at which the Rayleigh Line and the Hugoniot Curve are tangent is called the Chapman-Jouguet point on the supersonic branch of the Hugoniot (note that an additional point of tangency exists for $\hat{v} > 1$ - this is Chapman-Jouguet point on the subsonic branch of the Hugoniot). Analytic expressions for the states corresponding to this tangent point can be retrieved from the dimensionless equations by deriving the

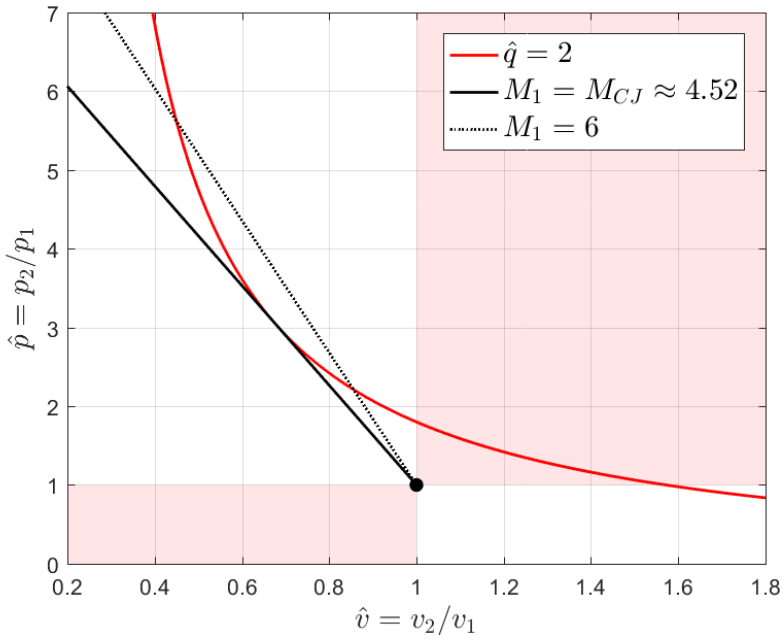

Figure 1.5: Unique solution to Rayleigh-Hugoniot relations for a given heat release. The point at which the Rayleigh Line is tangent to the Hugoniot is called the Chapman-Jouguet point on the detonation branch of the Hugoniot. Also pictured is a Rayleigh Line with a greater slope than that of the CJ detonation. Two solutions exist for this Hugoniot, a strong solution above the CJ point and a weak solution below the CJ point.

slopes of the lines and equating them:

$$M_2^2 = \left(\frac{\hat{v}}{\hat{p}}\right)\left(\frac{1}{\gamma}\right)\left(\frac{\hat{p}-1}{1-\hat{v}}\right) = 1 \tag{1.9}$$

Equation 1.9 succinctly states that the flow behind the detonation wave is sonic relative to the wave. Solving the Rayleigh relation and Hugoniot curve subject to the tangency restriction gives an expression for the inflow Mach, though a symbolic equation solver is recommended for derivation from this non-dimensional form. Replacing $\hat{q}$ with $(\rho/p)q$ concludes the derivation for the condition of the 1-D steady detonation:

$$M_1 = M_{CJ} = \sqrt{1 + \frac{q\left(\gamma^2-1\right)}{2a_1^2}} + \sqrt{\frac{q\left(\gamma^2-1\right)}{2a_1^2}} \tag{1.10}$$

As one can see from Figure 1.5, any Rayleigh Line with a slope (inlet Mach) greater than

that of the CJ detonation will not have a unique solution. In general, two solutions exist for a generic Rayleigh Line projected onto a Hugoniot.

1.2.5 Entropy

Considering the rise of entropy in the process of the detonation will provide clues as to why the steady detonation phenomenon adopts the aforementioned conditions. The starting point for an entropy analysis is the T - dS relationship:

$$\frac{ds}{R} = \frac{\gamma}{\gamma - 1} ln\left(\frac{T_2}{T_1}\right) - ln\left(\frac{p_2}{p_1}\right) \tag{1.11}$$

The pressure and temperature ratios in (1.11) can be recast as functions of inlet Mach and heat release. First, the entropy along the process line, the Rayleigh line, is calculated. The hypothetical process is shown in Figure 1.6. The reaction starts after a sufficiently strong shock initiates combustion. Combustion completes at the Hugoniot $\hat{q} = 1$. The entropy rise along this process (Figure 1.7) reaches a maximum when combustion is completed - the steady state. From this observation, one can claim that the steady 1-D CJ detonation occurs at the point of maximum entropy for the process.

The entropy rise along the Hugoniot (Figure 1.8) further describes this process. For the CJ detonation, the entropy rise observed is minimum relative to other detonation conditions. This *minimum* entropy rise (equivalent to the process entropy maximum of the Rayleigh Line) corresponds to the thermal choking of the downstream products relative to the front of the wave. This is evidenced by Figure 1.9, where the locus of inlet and outlet Mach numbers reaches an absolute minimum downstream Mach when $M_1 = M_{CJ}$. Note that the minimum entropy rise occurring for the $\hat{q} = 1$ Hugoniot corresponds to the maximum entropy condition for the process.

1.2.6 Summary

To summarize, the claim is that the following statements are equivalent (enforcing one enforces all others) for the 1-D steady detonation wave with the stated assumptions:

- The unique solution to the steady, 1-D detonation exists at the tangent point of a given Hugoniot and Rayleigh Line (Figure 1.5).

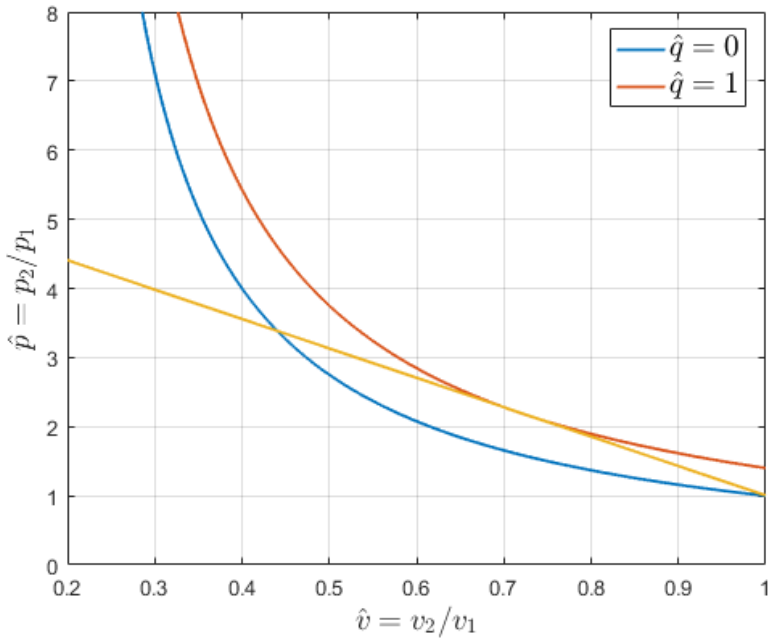

Figure 1.6: Hypothetical detonation process for $\hat{q} = 1$. The $\hat{q} = 0$ is the adiabatic shock Hugoniot. Combustion lifts the process line to the $\hat{q} = 1$ curve.

- Entropy rise for the detonation process is maximum at condition of complete combustion for given heat release (Figure 1.7).
- The CJ detonation occurs at the condition of minimum entropy rise along the Hugoniot (Figure 1.8).
- The CJ detonation occurs at the condition where the products of combustion are sonic relative to the front of the wave (Figure 1.9).

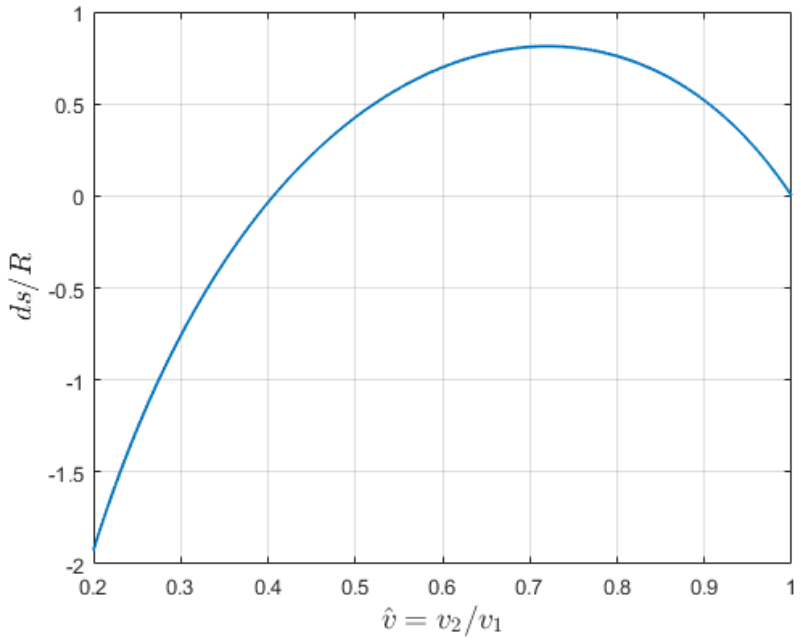

Figure 1.7: Non-dimensional entropy rise along Rayleigh Line for hypothetical detonation, corresponding to Figure 1.6.

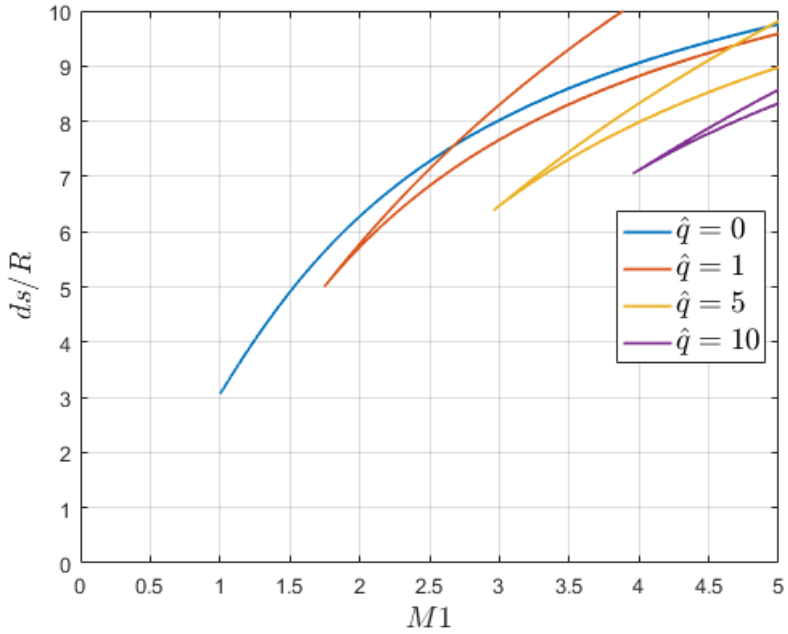

Figure 1.8: Non-dimensional entropy rise along Hugoniots for different heat releases.

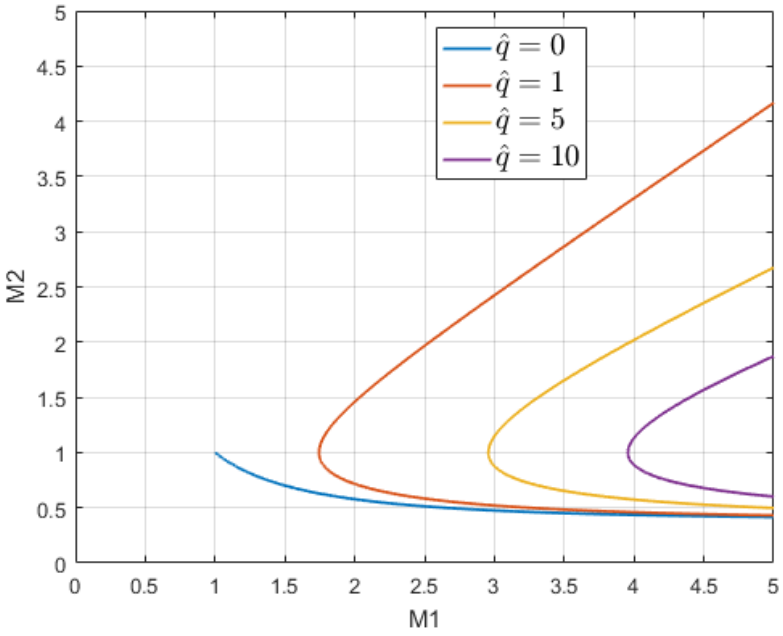

Figure 1.9: Variation of downstream Mach for varying detonation conditions.

1.3 Detonation Dynamics

Detonations exhibit complex dynamical behavior. In one-dimensional tubes, steady Chapman-Jouguet detonations can be shown to bifurcate into periodic limit cycles or decay further into chaotic regimes [31, 32, 33]. In two dimensions, the instabilities associated with the detonation wave front form a set of transverse waves that create intricate fish scale-like patterns [34] as the detonation propagates through the reactive medium. These dynamics are inherent to the detonation process. In describing the dynamics of RDEs, the *system architecture* becomes relevant in addition to classical detonation dynamics. Under the umbrella of *system architecture* is the injection and mixing scheme, combustor boundary conditions, and combustor geometry, all of which provide a *feedback mechanism* to alter the state of the RDE. Presented in this section is a brief review of literature regarding detonation dynamics. The interplay between classical stability arguments and RDE dynamics is explored. Comparisons between premixed combustors, rockets, detonations, and detonation engines are made. Finally, efforts to model detonation dynamics, including reduced-order mathematical models and detailed computational fluid dynamic RDE simulations, are discussed.

1.3.1 Classical Detonation Dynamics in Literature

The idealized steady detonation exists as a strong normal shock to which a induction and reaction zone is attached. This model of the detonation wave is called the Zeldovich-von Neumann-Doring (ZND) model [35] - a model proposed simultaneously but independently by these three researchers in the mid-1940's. ZND-type waves are excellent approximations of the underlying processes in a detonation wave. However, unless stabilized by some means (such as a geometric wedge [36], for example), these steady detonations are rarely seen in experiment [37]. Instead, detonations have been observed to propagate with multiple fronts, with transverse waves, and/or with "galloping" shock fronts [34, 37, 38]. These structures and phenomena develop because of instabilities associated with the detonation structure. A set of instabilities of relevance to the reduced-scope discussion of RDE dynamics is discussed in this section.

The hydrodynamic instability of the one-dimensional detonation wave front is tied to the nature of the strong normal shock preceding the combustion region. For strong normal

shocks, the region immediately behind the wave is subsonic and the shock is vulnerable to decay through interaction with rarefaction waves (as seen in Figure 1.9). Erpenbeck in the early 1960's [31] performed the first linear stability analysis on a perturbed detonation shock front. By attaching the reference frame to the perturbed shock, he derived the linearized and transformed Euler equations of motion with a global single-step exothermic reaction. Stability in this study was defined as exponential growth or decay of perturbations of the shock front. Regions of stability and bifurcation parameters, namely overdrive ratio $\epsilon = D/D_{CJ}$ (the shock front was assumed to be piston-driven) and heat release, were identified and explored theoretically. He noted, however, that the lack of computational tools precludes him from attempting more complex studies at the time of publication of the study. Several years later, armed with a computer, Erpenbeck included nonlinear effects as perturbations of the linearized terms from [31]. The linear stability analysis performed in this study was in two-dimensional phase space. Fixed points in this space gave rise to closed orbits, or stable limit cycles. Erpenbeck extended his analysis to Arrhenius-type kinetics [39] shortly thereafter, where he identified activation energy as a critical parameter in predicting the onset of 1-D detonation instabilities. This expanded the known dependence of the dynamics to chemical reaction rates in addition to the well-characterized hydrodynamic instability related to the preceding shock. Erpenbeck's mathematical methods for determining regions of stability are complex and tedious, requiring Laplace transforms of the linearized and perturbed initial value problem. Lee and Stewart [40] reproduced Erpenbeck's original results using a straightforward and readily applied Normal Mode approach, in which solutions in the form of a exponential with linear coefficients are sought and analyzed. This study presented growth rates of instabilities in 1-D detonations in the activation energy - overdrive parameter phase space.

Fickett [41] introduces the *eigenvalue* or weak detonation in his studies and subsequent monograph. With eigenvalue and other pathological detonations, the stability argument becomes more complex as the steady CJ solution is no longer unique. Rather, chemical equilibrium and loss effects (he includes endothermic reactions as a loss mechanism) open up the steady solution to the weak branch of the Hugoniot with products traveling away from the wave front at supersonic velocities, thereby increasing the distance between the reaction front and the fictitious 'piston' of [30] and [31]. Linear stability analysis of these

pathological detonations was executed by Sharpe [42] who showed that the qualitative behavior of pathological detonations followed that of perturbed CJ detonations. These effects are not confined to 1-D detonations. For completeness, noted is that Erpenbeck, Fickett, Sharpe, Lee, and Stewart all extended their analyses to higher dimensions.

Note that these studies do not identify any behavior through time. Rather, these studies aimed to identify stability criteria and limits for the detonation phenomena. There exists a great body of literature on the numerical simulation of, most generically, combustion instabilities. To exemplify the limit cycle behavior of detonations, only a small subset of available literature is presented here.

He and Lee [1] presented the first comprehensive study of the dynamical limits of the 1-D detonation wave. This study performed both numerical simulations of the reactive Euler equations as well as a linear stability analysis (analogous to that of [40]). Found were three regimes of dynamics, demarcated by the value of activation energy used in the models. For small activation energy (beneath some critical value), the detonation wave is stable to perturbations. For activation energies above this critical value but less than a second critical value, a galloping instability develops (as the strength of the preceding shock directly affects reaction rate). Lastly, for activation energy above both critical values, a series of period-doubling bifurcations occur, leading to a prototypical chaotic structure. This route to chaos is postulated to be the effect of the decay of the leading shock and the subsequent increase in required induction time. The pressure-time traces from [1] are reproduced in Figure 1.10.

Kasimov and Stewart [2] expanded on the work in [1] by performing high-order accurate numerical simulations in the shock-attached reference frame. The function of the sonic locus (location of thermal choke, or where $M_2 = 1$) of the detonation was explored. Their findings indicate that the location of the sonic locus relative to the wave front is intimately coupled with the detonation dynamics, since the sonic locus acts as a communication barrier between regions in the fluid domain. For galloping detonations, the location of the sonic locus is found to be phased-locked with the preceding shock pressure. The phase portrait is for this stable limit cycle is reproduced in Figure 1.11.

More recent efforts including multi-stage chemical models and effects of dissociation have yielded another set of dynamic-rich behavior. Borisov and Kudryavtsev [3] have shown

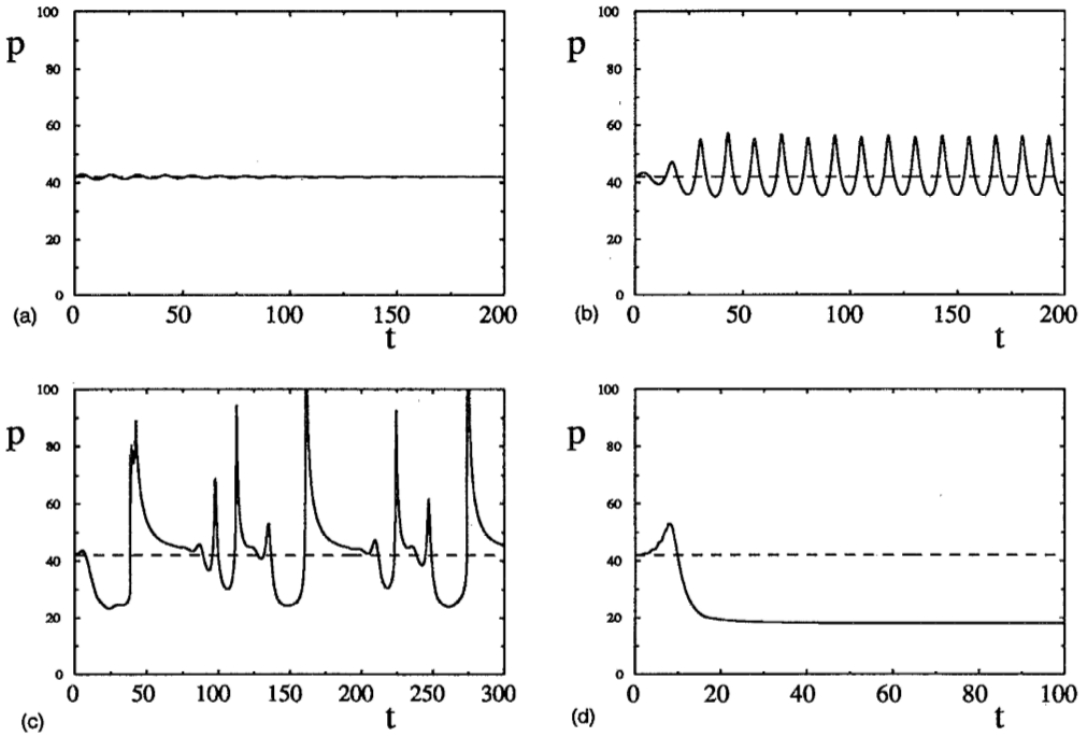

Figure 1.10: Traces of the von Neumann pressure spike of the preceding shock front reproduced from [1]. Activation energies of a) $E_a = 25$, b) $E_a = 27$, c) $E_a = 31$, and d) $E_a = 35$. In (a), the detonation is stable with respect to perturbations of the shock front. In (b), the perturbations grow exponentially until saturation, where a stable periodic structure is formed. In (c), a series of bifurcations leads to a chaotic pressure-time trace. Lastly, in (d) the strength of the shock is too weak for autoignition of the mixture.

that activation energy and dissociation energy have opposite effects on stability: an increase of activation energy leads to a greater degree of instability while an increase of dissociation energy leads to the weakening of the instability. The relationship between the two produce intricate phase portraits as shown in Figure 1.12.

Instabilities in higher dimensions have been simulated numerically primarily within the context of detonation cell investigation. While these studies are relevant in the broader context of detonation stability, they are not immediately of value in this dissertation. As such, their review is not presented here.

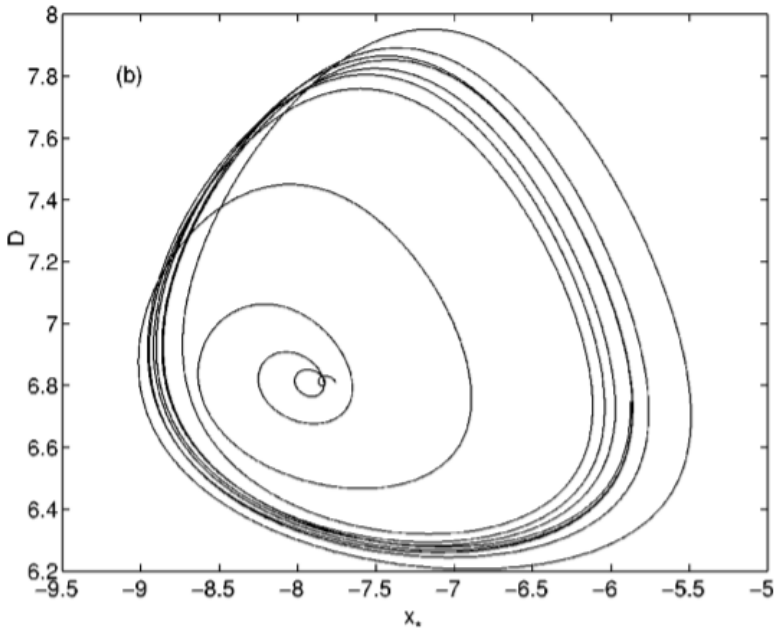

Figure 1.11: The phase plane of detonation velocity, D, and position of sonic locus, x_*. Reproduced from [2].

1.4 Self-excited Combustor Dynamics in Literature

Shifting focus to engine-level dynamics, the scope is broadened to include considerations from premixed combustors (such as those found in the gas turbine community), rocket combustors, and pulsed detonation engines. Within these systems, coupling of heat release processes with the state of the system can cause the self-excitation of dynamics. In some scenarios, these dynamics are negligible and can be considered purely acoustic. In others, the dynamics can grow exponentially and cause catastrophic mechanical failure. Each combustor type has its own set of literature regarding the engine-specific dynamics. Presented here are a small subset of studies that are of relevance to this dissertation.

1.4.1 Premixed Combustors

Lean premixed combustors, such as those used in gas turbines, are desired for their low emissions. However, when operating in a lean combustion mode, such combustors often experience large-amplitude pressure and heat release fluctuations that are self-excited and periodic. Over time, these fluctuations reduce the overall lifespan of the combustor.

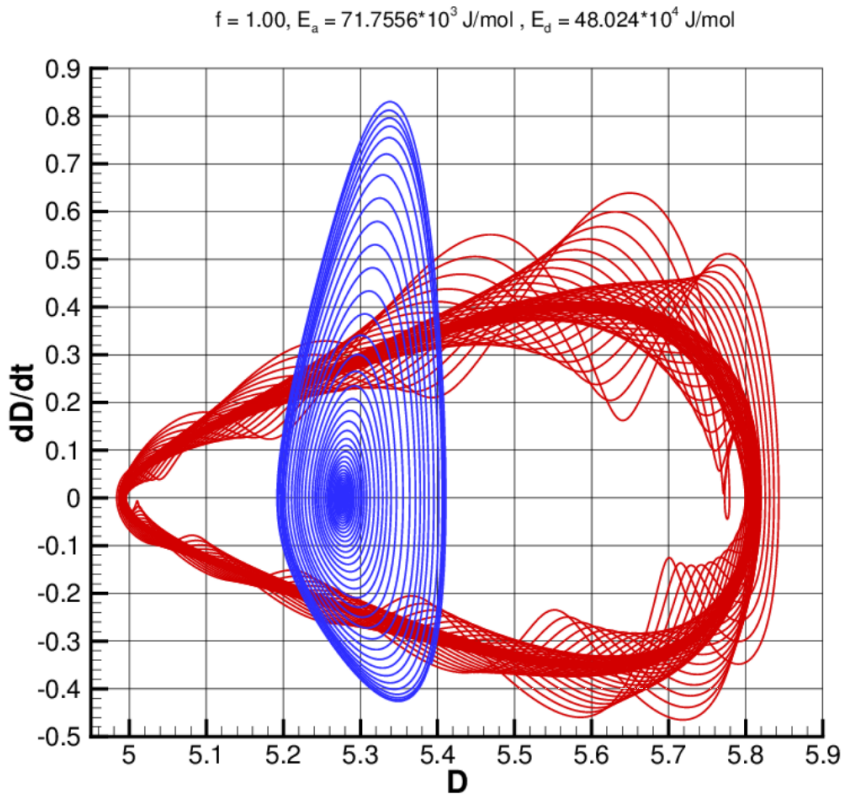

Figure 1.12: Phase portrait showing complex transition from damped oscillations about the limit cycle to a final periodic structure. Reproduced from [3].

Within this community, it is common to analyze a gas turbine combustor as a bluff-body stabilized turbulent premixed flame, both in experiments and models. One such experiment that observed self-excited dynamics is that of Schadow and Gutmark [43], where they observed the coupling of vortex shedding with the combustion or heat release process, in turn affecting the shedding of vortices off of the bluff body. In a separate study [44], the same authors linked acoustic resonance in the combustor to the heat release process, which resulted in the driving of large-amplitude pressure fluctuations.

Dowling [4] was the first to present a kinematic model for describing the dynamics of the self-excited lean premixed combustor. Her model is built around the notion of a *Flame Transfer Function* (FTF) - a function of frequency that describes the pressure fluctuations observed in the combustor. This FTF is the combination of a nonlinear flame kinematic model (based on the turbulent flame surface area) with chamber acoustics. She showed that an imbalance of acoustic energy (into the domain versus out of the domain) leads

to growth in disturbances that eventually saturate into limit cycle oscillations because of nonlinear effects. Example limit cycle trajectories from her paper are shown in Figure 1.13.

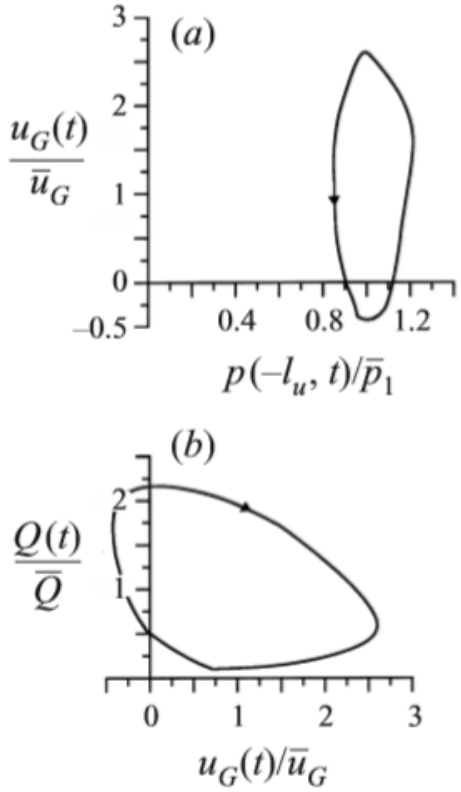

Figure 1.13: Limit cycle orbits in phase space describing the coupling of velocity and pressure fluctuations with heat release. Reproduced from [4].

Lieuwen [45] conducted a study where the transfer function between pressure oscillations and heat release was experimentally found. This study is unique in that the combustor studied was acoustically forced. The limit cycle behavior of the pressure and heat release coupling were shown to mode-lock with the acoustic forcing or take on the acoustic resonant frequency of the combustor.

Simplified quasi-1-D CFD models have also been used to describe the limit cycle behavior of lean premixed combustors. Paxson [46] uses the quasi-1-D reactive Euler equations to correctly predict limit cycle behavior in a stepped combustor. Similarly, Cohen [47] uses the same formulation for a contoured combustor subject to variations in fuel-air equivalence ratio. While these modeling efforts are ultimately slower than the analytic

counterparts, they are of a higher fidelity and capture the nonlinear effects (such as those inherent to fluid dynamics and chemistry-flowfield coupling) quite well.

1.4.2 Rockets

The discussion on rocket dynamics is limited to chugging-type instabilities in liquid propellant rockets. 'Chugging' is the term used to describe the low-frequency combustion lag associated with the coupling of heat release with propellant injection. Summerfield in 1951 [48] was one of the first researchers to observe and investigate the chugging phenomenon. In his study, he identified several influencing parameters on the chugging instability: length of the feed line, feed velocity, injector pressure ratio, and injector-to-chamber volume ratio. Each of these influencing parameters were found to enhance or damp the oscillations in pressure and heat release experimentally. Summerfield derived expressions for the chugging instability that agreed reasonably well with his experience at the Jet Propulsion Laboratory with an experimental rocket.

Crocco and Cheng [49] produced a comprehensive monograph on the subject of liquid rocket instabilities. In this text, they give mechanisms for low and high-frequency longitudinal instabilities in rocket chambers, taking into account the time and space lags associated with liquid injectors and unsteady combustion. Although their discussion was purely within the linear context (growth or decay of linear disturbances), they acknowledge the presence of nonlinear effects (such as shocks or other high-amplitude phenomena) observed in their experiments. In these experiments, the growth of the disturbances are similarly curtailed and the dynamics saturate into limit cycle behavior.

1.4.3 Pulse Detonation Engines

A pulse detonation engine (PDE), like a rotating detonation engine, features detonative heat release. A PDE, however, operates (like its name implies) with a low frequency longitudinally-pulsed operation. This pulsed operation is the manifestation of valve timing (poppet or reed valves) or combustor geometry (such as in a valveless pulse-jet engine). In a valveless PDE, the detonation expels combustion products out of the combustor. Because of the shape of the combustor, namely the different lengths and volumes associated with intake and exhaust ports, the rapid exhausting of the products

in turn creates a slight vacuum within the chamber, allowing for a fresh intake charge to enter into the domain through the shorter intake port. The self-excited pulsed operation is an example of saturated nonlinear effects resulting in a limit cycle. The explosion associated with the heat release stops the inflow of fresh propellant, leading to oscillations in the flow properties that are coupled with the pulsed detonations [50].

1.5 RDE Dynamics in Literature

A large number of experimental studies have observed and documented detonation wave dynamics within RDEs. Primary reported metrics are detonation wave speed (often transformed into frequency as the detonation travels around the annulus periodically) and peak pressure through time. The strength of the detonation wave and the associated heat release is directly related to the detonation velocity (see Section 1.2). System-level parameters that are most often controlled in these studies are mass flow rate and fuel/oxidizer equivalence ratio.

Two recent studies exemplify the diverse behavior of rotating detonation waves: that of Chacon and Gamba and that of Bohon [6]. Chacon and Gamba created a set of spectral analysis tools to fully characterize the wave structures present in their experimental rig. By attaching the reference frame to the experimentally found dominant propagation speed, the frequency of the wave becomes zero. In this framework, secondary and tertiary wave structures (speed and direction) are extracted (Figure 1.14). Counter-rotating and acoustic waves were found to exist and interact with the primary detonation wave. In experiments with counter-rotating waves, the velocity of the primary wave is seen to modulate, implying a direct impact on the strength of the preceding shock front of the detonation wave, much like that of the galloping detonation.

In Bohon's study [6], fast-response piezoelectric pressure sensors and luminosity measurements were used to characterize the detonation waves in their RDE on a cycle-to-cycle basis. Periodic oscillations in luminosity and pressure (Figure 1.15) were observed for some modes of operation, consistent with Chacon's observations. Bohon documented the detonation wave properties through a parametric sweep of combustor mass flow rates and fuel/oxidizer equivalence ratio. The study again identified several

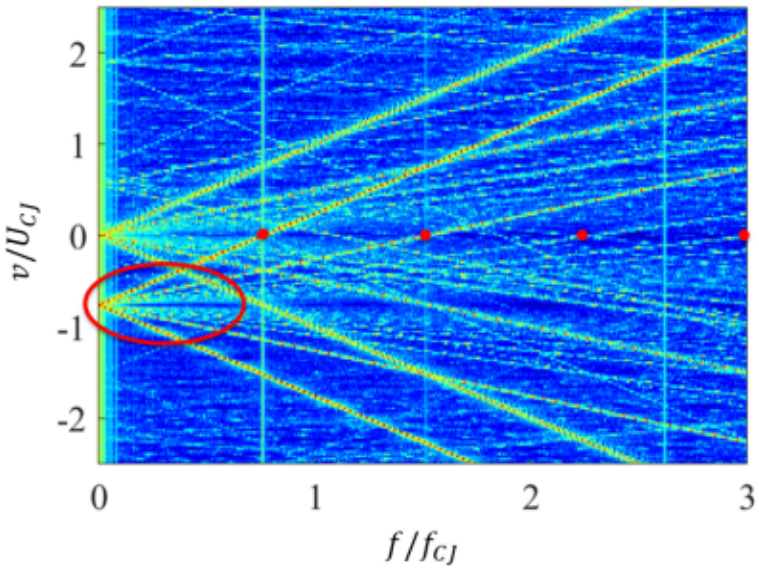

Figure 1.14: Wave structures present in experimental study of a RDE combustor. The spectral analysis is shifted to the wave reference frame such that the detonation wave appears steady. The Red dots are harmonics of the primary detonation wave. The red circle shows the location of the y-intercept of the main detonation wave. Reproduced from [5].

modes of detonation propagation, from the presence of counter-rotating detonation waves to weaker secondary wave structures (whose origin is unknown). Stability limits, defined by 'clean' frequency content in pressure-time traces, were given with equivalence ratio as a parameter. Stability suffered towards propellant mixture extremes (lean and very rich mixtures).

In addition to the detonation wave properties and dynamics, the manner in which fuel and oxidizer is fed into the combustion chamber plays a significant role in the behavior of the RDE. Most injection schemes in laboratory-scale gaseous RDEs use *nominally* choked injectors. Both experimental [51, 52, 53] and numerical studies [54, 55] conclude that the passage of the high pressure detonation waves over the nominally choked orifices temporarily block the flow of fresh propellant. If the passing wave is strong enough, backflow is possible. This is a negative feedback process by which the inlet mass flux into the combustion chamber is limited by the periodic choking/unchoking/backflow of the injectors, in turn limiting the heat release rate of the device. As reported, this

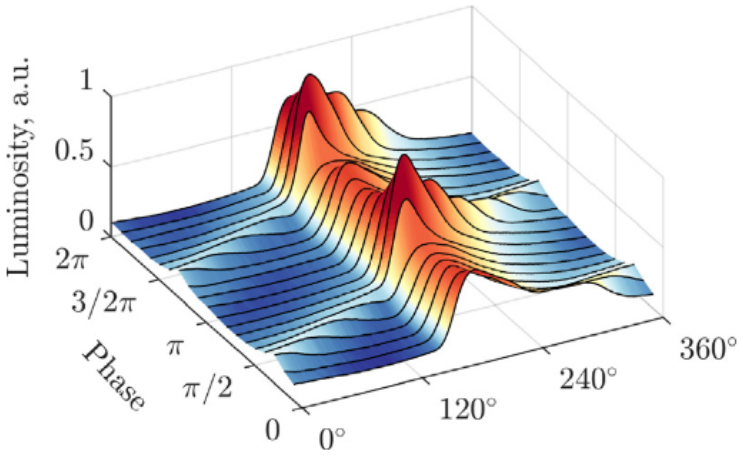

Figure 1.15: Phase-averaged measured luminosity shifted to the wave reference frame. Reproduced from [6].

phenomena is common among different engines and configurations, but the quantitative measurements of the phenomena are divergent and engine specific. The mixing scheme for any particular RDE cannot be de-coupled from the injectors. Because of the introduction of injector blockage, the mixing is now necessarily a function of the state of the RDE in addition to the design of the injection system, regardless of the mixing strategy (impinged jets, radial, axial, etc.). Anand [56, 57] further describes RDE dynamics by categorizing RDE operating modes into four groups. This categorization was based on wave number, observed transients, presence of sidebands and/or harmonics in the frequency spectra, and longitudinal pulsing. Anand concluded that inadequate mixing is the cause of aperiodic wave structures, leading to pulsating in the amplitude of the detonation waves. He also found that higher wavenumber modes of operation are less sensitive to perturbations.

How these dynamics change with varying outlet boundary conditions is of great importance to the RDE rocket community. An experimental study by Smith of GHKN Engineering [7] showed supersonic exhaust plumes without a mechanical choke (Figure 1.16). The implication of the supersonic plume is that a sonic point exists somewhere in the combustor, isolating the front of the combustor from characteristics originating from downstream of the sonic position. The presence of a sonic line is critical. Just as the presence and location of the sonic locus is a controlling parameter in galloping detonations, the presence, or lack of, a sonic locus in the RDE combustor can influence engine dynamics.

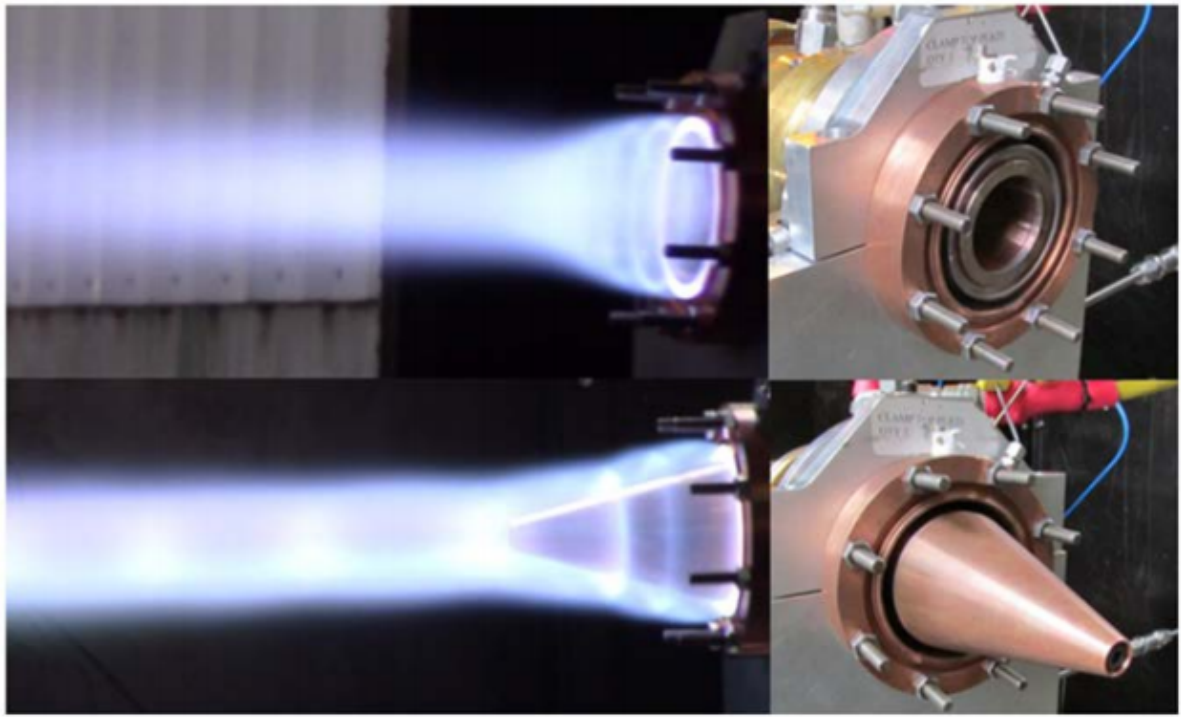

Figure 1.16: Exhaust plumes from methane-ox RDE. Reproduced from [7].

Recent years have seen a surge in numerical simulations of RDEs, with increasingly complex domains as computing resources become cheaper and more widespread. The hallmark RDE flowfield was given by Schwer and Kailasanath [8]. This was a 2-D reactive Euler simulation. The 2-D domain was assumed to wrap around the mean annular diameter cylinder with periodic boundaries on its left and right sides (see Figure 1.17). The outlet boundary was modeled as a spatially varying subsonic/supersonic outlet, depending on the state of the internal domain. The inlet was modeled as a total pressure inlet, unless the pressure inside of the domain was higher than that of the assumed plenum. In this scenario, the inlet was modeled as a wall.

The flowfields in Figure 1.17 show the major features present in all RDEs - the detonation wave, the oblique shock attached to the wave front, the contact discontinuity, and shear layer. In this study, and similar studies by Paxson [58] and Schwer [59, 54], it is important to note that the dynamics are assumed to be a single wave wrapped around the annulus prescribed by the physical dimension of the domain. In this manner, the dynamics are assumed and not simulated. Still, these studies provide a great amount of detail about

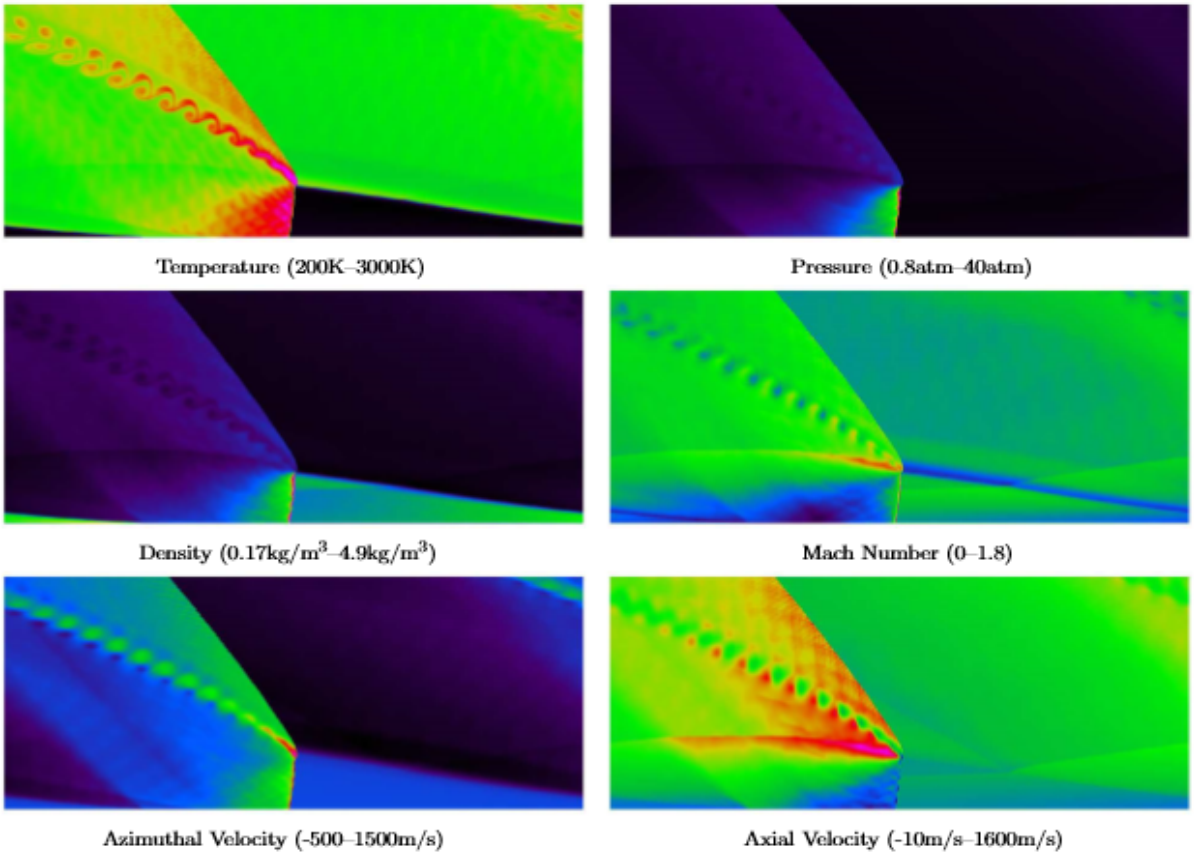

Figure 1.17: Snapshots of the RDE canonical flowfield. Reproduced from [8].

the structure of the RDE flowfield and detonation propagation characteristics. Such metrics include detonation velocity (a key metric of comparison between experiments and models), propellant fill height, and pressure and temperature traces.

Several research groups have made advancements in 3-D numerical simulations. Lietz [9] constructed a full 3-D model of a laboratory-scale RDE, complete with detailed chemistry and actual injector and combustor geometry. Snapshots of the solution are given in Figure 1.18. In this study, the simulation was able to capture the wave number (7 waves in simulation versus 8 in experiment) and detonation wave speed. Because the injectors were modeled, the relationships between the detonation wave and the injectors were implicitly modeled. Blockage and backflow can be observed in the study's results. This study can be considered the current - as of this writing - state of the art in CFD for RDEs. A drawback to the high-degree of fidelity is the computational cost. The simulation required several thousands of CPU cores over the course of about a week.

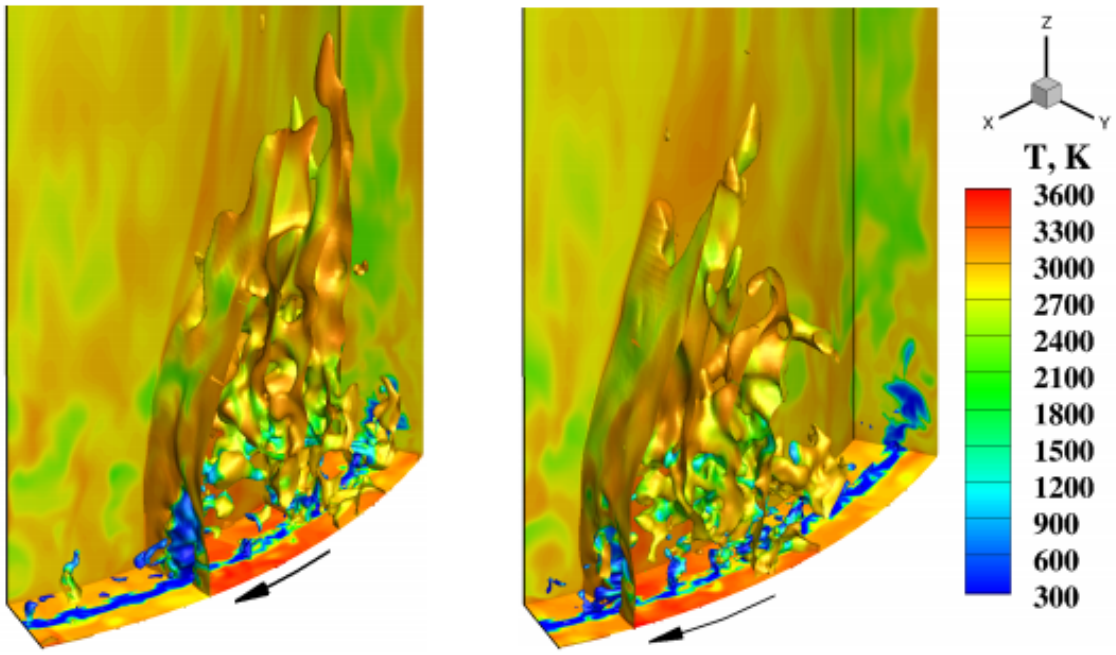

Figure 1.18: Snapshots in time of full 3-D numerical simulation with detailed chemistry and geometry. Reproduced from [9].

The prohibitive computational cost of high-fidelity 3-D simulations have driven other research groups in the opposite direction towards reduced-order models. These models aim to capture the major components of the RDE flowfield at a fraction of the computational time required by 3-D simulations. Humble [60] created a reduced-order model for a RDE flowfield by using a 1-D shock tubes to approximate the flow at a singe azimuthal slice. Fievisohn and Yu [61] created a method-of-characteristics analysis tool to accurately model the quasi-steady RDE flowfield. Similar to both [60] and [61], Kawashima [62] created a quasi-1-D reduced order model for the RDE flowfield by dividing the 1-D domain into regions of constant properties through a characteristic analysis (shock tube problem with contact discontinuities). The study is able to reproduce CFD by Schwer [8] in significantly less time. However, the quantitative pressure and temperature traces associated with the detonation wave passage were not in close agreement with higher-order CFD results. Nevertheless, the qualitative behavior was shown to be correct and the authors plan to use the model as the basis for control algorithms.

There still exists a gap between numerical simulations and experiments for capturing

physical dynamics of the combustor. While experimental studies have shown a great variety of operating modes (slapping, amplitude modulation, wavenumber variation, etc.), most computational studies can only reproduce the quasi-steady limit cycle for an assumed wavenumber. Only recently have researchers begun to investigate instabilities within the RDE. Paxson and Schwer [10], within their 2-D computational framework, have investigated thermoacoustic instabilities associated with high injector-to-annulus area ratio (AR) combustors. In their study, the authors found that reflected waves off of the rear boundary caused destructive interference with the traveling detonation wave. The influence of the reflected waves in the combustor was found to be parameterized by AR. For a sufficiently large AR, the perturbations to the refresh process grew with time (leading to longer refresh times), eventually prohibiting the propagation of the detonation wave. The destructive interference is shown in Figure 1.19.

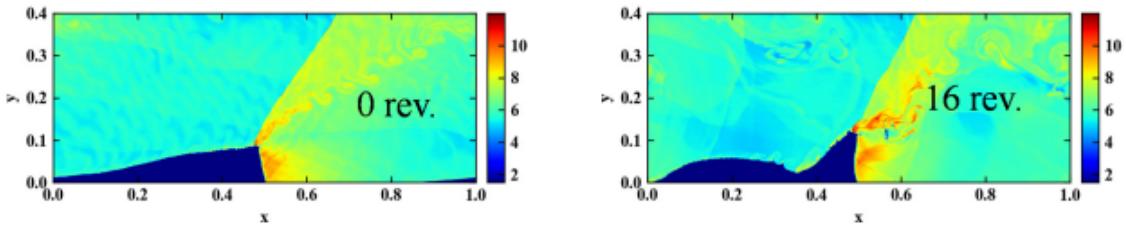

Figure 1.19: The development of a thermoacoustic instability in a 1-wave, 2-D RDE simulation. The reflection of outgoing characteristics destructively interferes with the traveling detonation wave. This instability was found to be parameterized by injector-to-annulus area ratio. Reproduced from [10].

1.6 Summary

Themes of self-excited dynamics and limit cycle behavior are consistent at all levels of abstraction: from classical detonation stability arguments through to system-level injector-combustion coupling. The key takeaways from this literature survey are as follows:

- In certain settings, detonation fronts are unstable to perturbations.
- Self-excited oscillations can occur when there is a coupling of the heat release process and the state of the flowfield. This has been observed to be true in RDEs.

- Limit cycle behavior occurs when nonlinear dynamics saturate. Limit cycles are common among low-dimension detonation experiments through to system-level RDE dynamics.
- Within RDEs, injector-detonation dynamics, detonative heat release, and combustor boundary conditions have all been identified as potential feedback mechanisms.
- The effects of various modes of operation in RDE on performance metrics are not well quantified or understood.

Chapter 2

Experiments

The goals of the experimental portion of this dissertation are to (i) survey RDE operability and with respect to engine geometry and boundary conditions and (ii) capture and document trends in detonation wave behavior. Here, a database of engine dynamics is created to aid in the creation of a nonlinear dynamical model in Chapter 3. In this chapter, the RDEs and test stand are detailed, along with the relevant instrumentation. Following the description of the experimental apparatus, the data reduction techniques are presented. Three sets of experiments are presented: (i) effects of backpressure (154-mm RDE), (ii) effects of total injection area on operability (76-mm RDE), and (iii) a survey of wave dynamics with four injector configurations in the 76-mm RDE. This chapter concludes with a summary of the experiments performed and major takeaways.

2.1 Apparatus

Two separate engines were tested in this study - a 154mm (6 inches) flowpath outside diameter (OD) engine and a 76mm (3 inches) OD engine. Their mechanical designs and features are presented here.

2.1.1 154-mm RDE

The 154-mm RDE is a legacy engine constructed to establish rotating detonation waves as an internal proof of concept. The complete details of this engine are presented in

[63] and [64], though a summary of the features are presented here. Table 2.1 details the major dimensions of this engine. This RDE (Fig. 2.1) is an in-house designed and machined stainless steel apparatus with a nominal 154-mm (6") flowpath OD.

The propellant injection scheme is radial. Along the circumference of the annulus, orifices for fuel (outside) and oxidizer (inside) direct propellant perpendicular to the axis of the annulus. The orifices are staggered to promote vortical structures, which entrains fuel and oxidizer and is the dominant mechanism for mixing [63, 65]. Because the scheme does not use any axial injection, the front endwall (the thrusting plane) of the 154-mm-RDE can be instrumented.

Ignition is provided by the Wave Generator (WG). Twelve circumferentially mounted spark plugs are 'fired' sequentially. The WG driver deposits up to 10 mJ per spark per plug at rates up to 8 kHz. The number of induced shock waves, along with the desired spin, can be controlled by the user by simultaneously sparking multiple plugs at a specified firing frequency. These initiation control techniques have been demonstrated in [65].

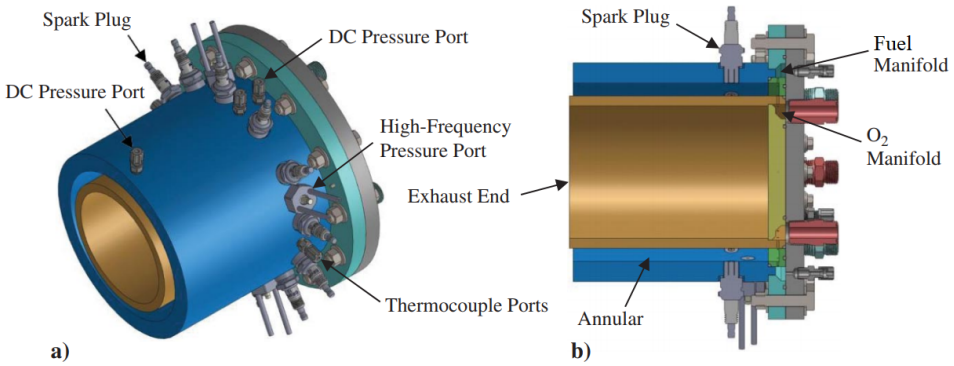

Figure 2.1: Isometric and cutaway views of UW 154-mm RDE.

The RDE is a passively cooled (heat soak) 304L stainless steel device. The inner annulus has a 23° conical nozzle fixed to its end, extending into the piping that routes combustor effluent to a large dump volume. Instrumentation ports line the circumference of the engine near the spark plug axial plane, as well as strategically placed ports on the front endwall and along the axial length of the combustor. These locations are shown in Fig. 2.2.

Table 2.1: 154-mm RDE specifications

Mean diameter	142.8 mm
Flow OD	154.0 mm
Flow ID	131.6 mm
Annular gap	11.2 mm
Annular cross sectional area	5020 mm^2
Combustor length	182.0 mm
Fuel orifice diameter (24x)	1.19 mm
Oxidizer orifice diameter (24x)	1.78 mm

2.1.2 76-mm RDE

A 76-mm RDE was purpose-built for this study. The design goals for the 76-mm RDE were to create a laboratory-scale RDE with high instrument density that could be easily modified to test different injection schemes, injector-to-annulus area ratios, and combustor geometries. The RDE flowfield is a harsh environment with exceedingly high temperatures and pressures: this harsh environment makes design and instrumentation of RDE combustors a non-trivial task, despite the apparent mechanical simplicity of an annular combustion chamber. For laboratory-scale research engines, a common practice is to use heat-sink metallic construction (such as the 304L stainless steel of the 154-mm RDE) to allow for extended duration run times before ablating flowpath material or losing mechanical integrity. A consequence of design for heat-sink hardware is difficulty instrumenting regions of interest in the engine, namely the area around where the detonation waves travel, the plenums, and the front end of the combustion chamber. The 76-mm RDE overcomes these design challenges with careful systems integration and partitioning of the RDE hardware into modular sections.

A rendering of the assembled engine is shown in Figure 2.3. The engine is constructed of a 304L stainless steel shell that is sleeved with oxygen-free, high thermal conductivity (OFHC) copper. The high thermal conductivity of the copper allows for experiments with high mass flux without the need for active cooling. Additionally, the choice of a sleeved combustor transfers responsibility of load containment from the copper sleeve to the stainless steel shell.

The containment shell is comprised of two flanges and a cylinder in a welded assembly. The rear flange (standard 6" steam flange) is the attachment point to the test cell dump

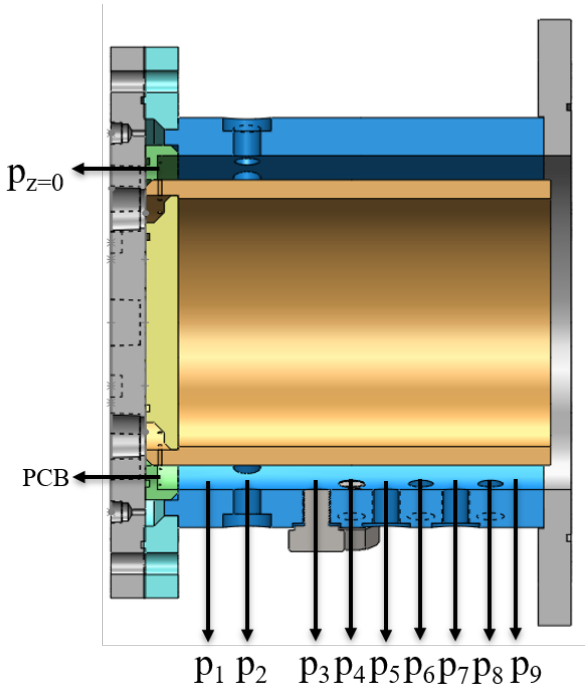

Figure 2.2: Location of static pressure sensors for 154-mm RDE.

volume. The negative volume between the front plate and the front flange form the plenum chambers for the fuel (inside) and oxidizer (outside). Injection is handled with discrete injection rings that are secured by the engine core and engine sleeve. Lastly the engine core is affixed with a center-running bolted connection. Redundant seals are present on all leak paths.

The RDE features 24 instrument ports along the combustor, 5 instrumentation ports on the combustor front endwall, and 4 ports in the propellant plenums. With a suite of fast-response piezoelectric pressure sensors, simultaneous monitoring of detonation wave dynamics in the combustor, along the front endwall, and within the plenums is possible. Arrangement of the instrumentation ports allow for co-located static pressure and static temperature measurements with 12.5 mm axial resolution.

The engine is modular in that the inner core and injectors are replaceable. This allows for quick setting of the injector to annular area ratio as well as tailoring injectors to specific propellants. The design can accommodate injection schemes using radial injection, transverse injection, and axial injection, in both discrete injection rings (Figure 2.4) and in injector blocks (Figure 2.6). Provisions are included for further modifications

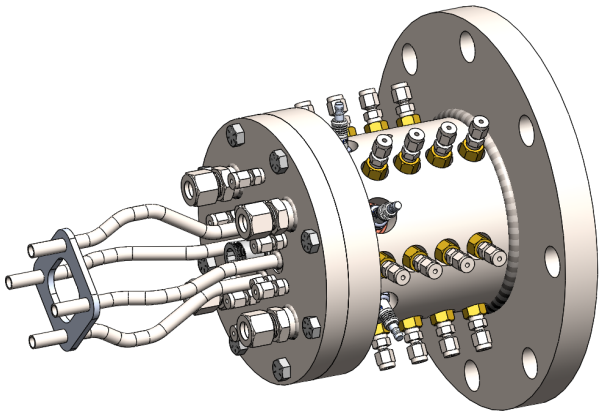

Figure 2.3: CAD rendering of the 76-mm RDE. The engine is a copper-sleeved stainless steel construction. Along the side of the engine are 24 instrumentation ports (3 sets of 8 axial stations).

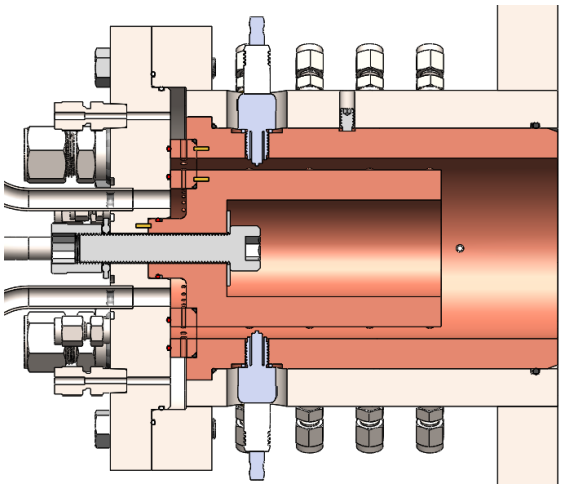

Figure 2.4: Cutaway view of the RDE with radial injectors and medium length core.

including changing the annular gap (from 5 mm to 3 mm or 7 mm), adding nozzles to the engine core, and altering the injectors to allow for liquid injection.

An example drop-in injector modification is shown in Figs. 2.6 and 2.7. This is a 72-element impinging-type injector designed as a 'drop-in' modification to the engine. Complete machining drawings for the 76mm RDE and the impinging-type injector are given in the Appendix.

Figure 2.5: Manufactured hardware and swappable engine cores.

2.1.3 Test Stand

The test stand in which the RDEs are operated is a backpressure-controlled and optically accessible test chamber. The RDEs attach directly to transitional piping that directs all exhaust gases to a dump volume of approximately 4 m^3. The basic layout is shown in Figure 2.8. The engine centerline is offset from the dump volume. This enables optical access via the leg of the wye in the transitional piping (Fig. 2.9). The significant thermal mass in the test stand piping and dump volume enables safe testing of the RDE for extended durations runs. The limiting factor is the heat soak of the engine. Current pumping capabilities allow for testing from atmospheric pressure down to 2 kPa, absolute.

A plumbing and instrumentation diagram (PID) of the test cell is given in Fig. 2.10. Note that this PID is for *either* fuel or oxidizer flow - the accompanying gas is handled through a symmetric system. The fuel and oxidizer are supplied with standard commercial compressed gas cylinders manifolded together. Nitrogen 6-packs are plumbed into the separate fuel and oxidizer lines (1x each) for pre- and post- purging of the experiment with inert diluent. Mass flow rates are set with hand-set pressure regulators. The mass flow rates are measured with a venturi meter on the supply lines leading to distribution manifolds on the mounted engine.

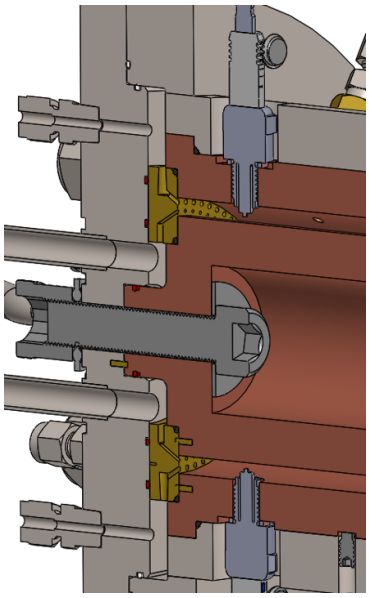

Figure 2.6: CAD showing the inclusion of a impinging type injector with 72 orifice pairs.

Table 2.2: Description of instrumentation.

Venturi - fuel	Badger Meter: VBR Brass 1/2”
Venturi - oxidizer	Badger Meter: VBR Brass 3/4”
Venturi DP	Omega PX419-500DDU5V
Venturi P1	Omega PX319-1KA5V
Plenum P	Omega PX319-500A5V
Combustor P	Omega PX319-500A5V
Temperature	Type-K thermocouples (all)
High Speed Camera	Phantom Camera v1211
Piezoelectrics	PCB 111A24

The instrumentation used for this study does not require signal conditioning as all outputs from sensors are zero to five volts (on-board conditioning), with the exception of the piezoelectrics and thermocouples. Piezoelectrics were conditioned with Kistler and PCB-amplifiers. The “slow response” sensors (including the thermocouples) were sampled at 2kHz by a desktop PC-mounted NI DAQ card.

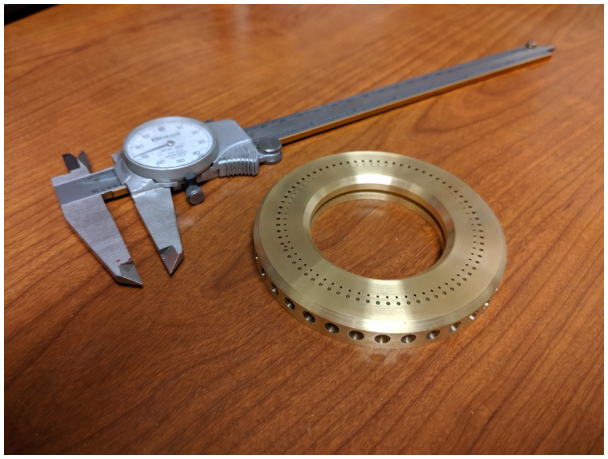

Figure 2.7: Manufactured impinging injector hardware

2.1.4 Data Processing

Automated Data Acquisition and Processing

The entirety of the experiment is run and post-processed automatically within Matlab. By using a standard input format (for example, an Excel spreadsheet detailing the experiment to be run), the Matlab scripts build the specified experiment and submit the commands to the National Instruments queue to be executed at the user's command. Once executed, all data is immediately calibrated according to calibration sheets unique to each sensor used. The Matlab scripts navigate these tasks through carefully encoded input files that contain maps from DAQ channels to sensors and their associated calibration sheets. The most immediate benefit of such a system is that the post-processing of the data becomes automatic: all experiment data is automatically in the workspace immediately after running each experiment. Should multiple experiments be run, the data is stacked and readily plotted and exported.

Image Processing

For experiments in which there is high-speed footage, an image processing routine was created to facilitate the extraction of the features from the video. The routine is based off of concepts presented in [66]. For each video, several frames of steady operation are averaged to give a representative location of the annulus in the video frame. Figure 2.11 displays the output of frame-averaging. By using Matlab's built-in Hough transform

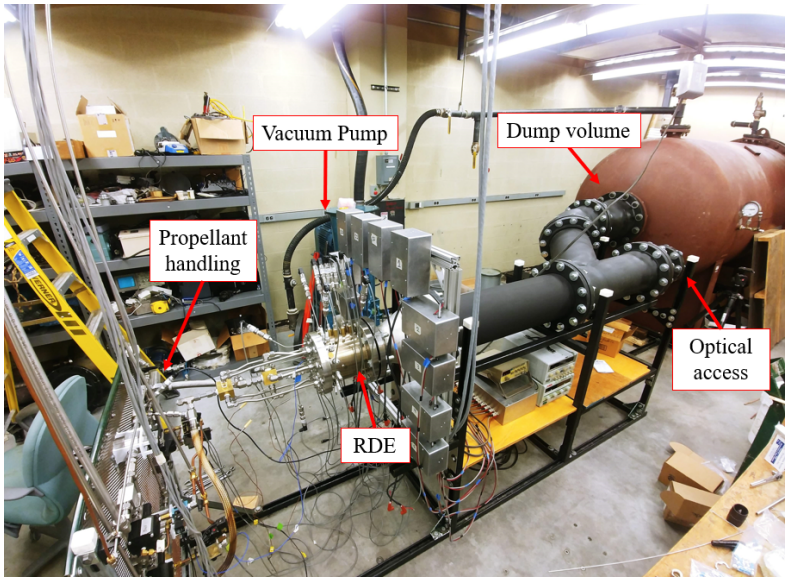

Figure 2.8: View of UW High Enthalpy Flow Laboratory test cell.

routines, the location of the annulus can be bounded by two circles of different polarity (a 'bright' circle of the OD and a 'dark' circle of the ID). Averaging the circle centers but retaining the radii, these can be plotted over top of the averaged video frames, as in Fig. 2.12. The circles are converted to a polar mesh with a specified number of bins (180 are shown in Fig. 2.12). The pixel intensity in each element of the polar mesh is integrated over the area of the element. This is done in a loop for each video frame, yielding a 1-D matrix of element-wise pixel intensities stacked frame-by-frame. Displaying these matrices (as a pseudocolor plot, for example) give spatio-temporal behavior of the luminosity content in the videos.

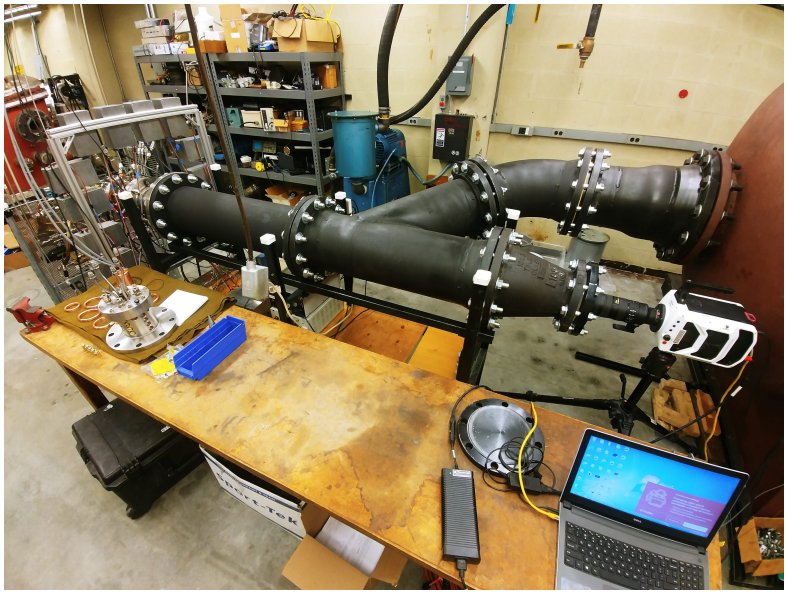

Figure 2.9: Optical access afforded by diversion of exhaust gases through a wye section.

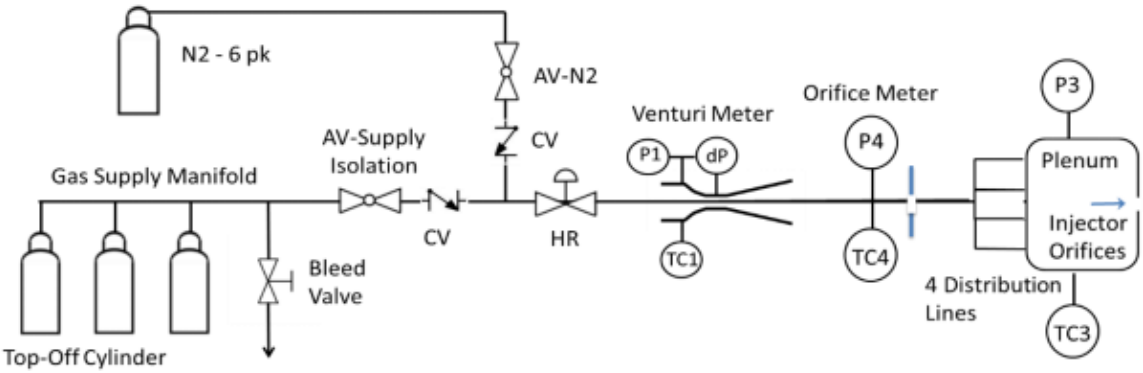

Figure 2.10: PID of experiment for *either* gaseous fuel or oxidizer. The same system is mirrored for the complementary gas.

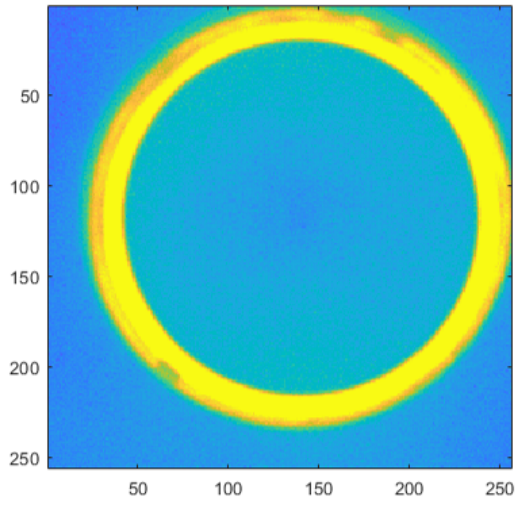

Figure 2.11: Raw pixel intensity of a high-speed camera frame. This image is 256-pixel square. The annulus location can be extracted via a Hough Transform.

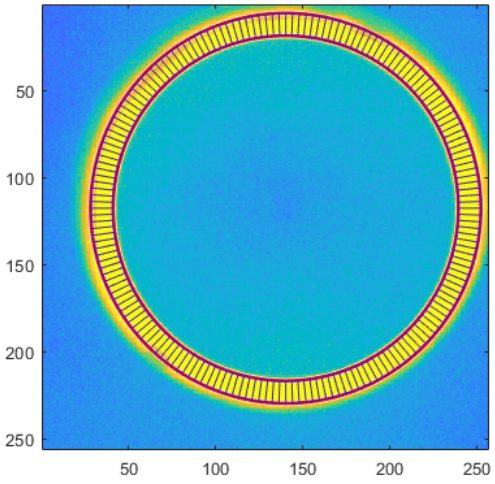

Figure 2.12: The extracted annulus location superimposed of the averaged high-speed video frames. A polar mesh is built between the two circles. For each video frame, the pixel intensity within each polar element is integrated and stored in a matrix.

2.2 Backpressure Effects

2.2.1 Procedure

The goal is to establish the operating envelope of the 154-mm RDE where the conditions in the combustor are independent of downstream pressure. The implication is that backpressure insensitivity points to the existence of a sonic point in the annular duct system (since the downstream pressure fluctuations are not communicated upstream). This set of experiments consisted of fixing the dump volume pressure to a known sub-atmospheric value while operating the engine at different mass flow rates for 0.9 second pulses. Presented here is a complete sweep of backpressure from ambient (1 atmosphere) to approximately 5 kPa performed at nominal mass flow rate of 130 g/s (26 $kg/m^2/s$). All experiments used methane and oxygen for the fuel and oxidizer. Chemistry variations were not within the scope of this study. As such, the target equivalence ratio was 1.1 for all experiments. Similarly, no high-speed camera footage was recorded for this portion of the study.

For each experiment, there is pre and post-purging with nitrogen with the sequence shown in Fig. 2.13. The ignition system is switched on while fuel is flowing until the oxidizer has ramped up to its steady flow rate, when ignition is expected to occur. There is a period of roughly 0.5 seconds when the ignition system is off and fuel and oxidizer are flowing. It is within this window that the data of record are taken. For axial profile plots, this is at 2.5 seconds. Following the shutoff of fuel and oxidizer is a nitrogen purge of 1 second duration.

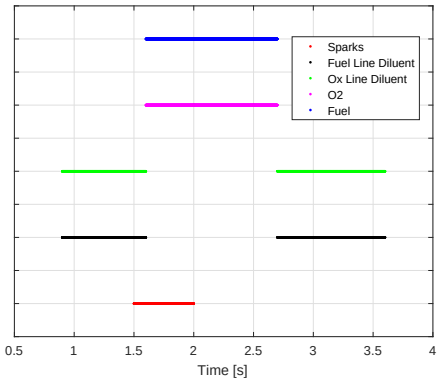

Figure 2.13: Valve states through the experiment.

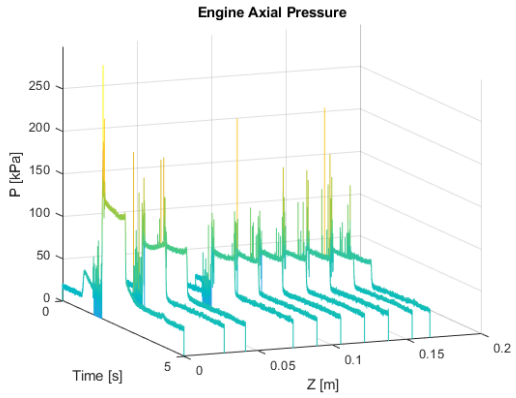

Figure 2.14: Static pressure through the combustor for the duration of the firing.

2.2.2 Results

The primary metrics for analysis and comparison in this study are the amplitudes of the slow-response pressure signals and frequency content of the fast-response pressure signals. The slow-response pressure data give insight into the axial variation of the static pressure in the annulus. These slow-response measurements are the main diagnostics for system-level properties. Fast-response piezoelectric pressure response data monitor the detonation wave arrival times and are the primary diagnostic for wave amplitude and speed. First, typical data generated from a single experiment is presented as a baseline for comparison of the data sets.

The combustor static pressure history for a single experiment is shown in Fig. 2.14. Each of the axial stations, as measured from the front endwall of the annulus, is displayed to scale with static pressure magnitude (in absolute units) throughout the duration of the experiment. In general, the static pressure signals from the combustor all exhibit the same characteristics in this firing. There exists a period of ramp-up in pressure during the diluent purge followed by a sharp rise in pressure when ignition and DDT occur, followed by a plateau. Once the propellant feed is switched to diluent, the pressure returns to that of the dump tank. Figure 2.15 provides a more detailed look at the pressure trace for a single sensor - in this case, the pressure at 2.7cm downstream of the front endwall. Displayed in this figure are two pressure signals, one in blue (detonation) and the other in red (without combustion), with the experiment flow control valve states overlaid in color. The regions shaded in blue correspond to the pre- and post-purging

with nitrogen, which occur from $0.9 < t < 1.5$ s and from $2.5 < t < 3.1$ s. The red region indicates the flow of propellant, which is sandwiched between the diluent purges. The half-second of 'sparks on' is the region bounded by the vertical dashed lines. Note that because of the finite volume of the dump tank, the beginning and end pressures are not equivalent, because a significant fraction of the combustion products are noncondensible and extra nitrogen is added to the system. Likewise, the pressures during the pre- and post-purges of nitrogen relate to the pressurization of the combustor from the flow of the diluent only - there is no combustion during these phases.

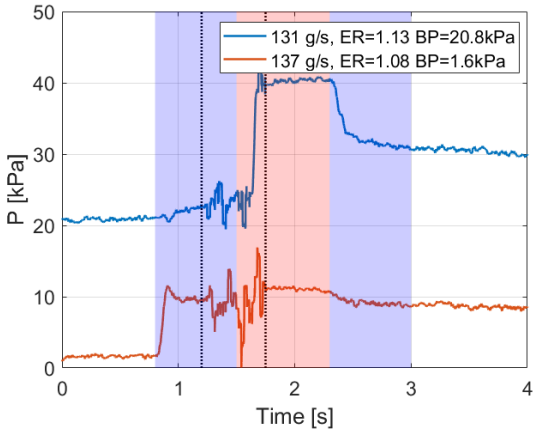

Figure 2.15: Time history of pressure signal $P_{z=2.7cm}$ for a reactive and non-reactive case. The non-reactive case is plotted in red and does not exhibit a pressure jump in the time history.

The axial static pressure profile of the engine is plotted for a reactive and non-reactive experiment in Fig. 2.16. The static pressure decrease indicates axial acceleration, whereas a relatively flat profile indicates nearly constant flow. Taking the static pressure as measured on the front endwall as a reference pressure ($P_{z=0cm}$), the pressure can be normalized and re-plotted, as in Fig. 2.17. This non-dimensional representation is the basis upon which different experiments are compared on a macro scale. Note that in Figs. 2.15-2.17, the non-reactive case shows significant pressure gradient through the axis of the engine. However, this is capturing the flow expanding to the ambient pressure of the system (i.e., to the set backpressure in the dump volume).

Inferences are made about the detonation wave structure from the fast-response PCB data. The sampling rate (1.25 MHz) of the PCB is sufficient to detect the passage

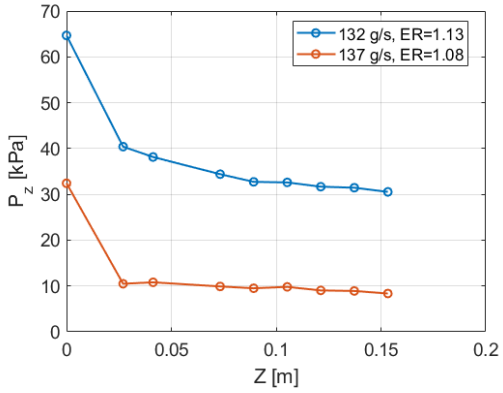

Figure 2.16: Static pressure profile at a slice in time. The red profile is a non-reactive case. The blue profile is typical of a experiment with stable detonative operation. (Run # 739 (reactive) and # 740 (nonreactive))

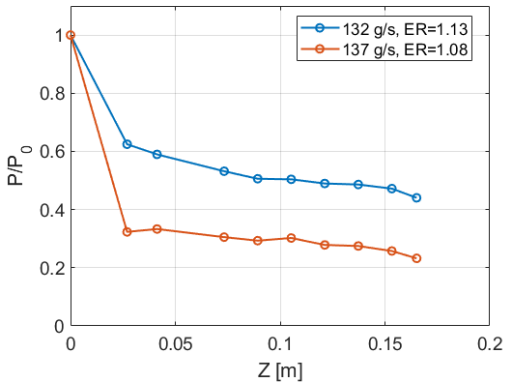

Figure 2.17: Normalized static pressure profile for reactive (blue) and nonreactive (red) experiments. (Run # 739 (reactive) and # 740 (nonreactive))

of the detonation waves. An example of the raw voltage output from the PCBs is shown in Fig. 2.18. The regularity of the phase lags between the front and side-wall PCB signals indicate that they are locked with constant time delay. This constant-phasing is interpreted as the front endwall sweeping of oblique shock waves emanating from the spinning detonation waves [65]. Time-frequency data are extracted from the fast-response pressure signals through the short-time Fourier transform, yielding a spectrogram corresponding to each experiment. The power spectral density and spectrogram for this experiment are given in Figs. 2.19 and 2.20, respectively. The PSD shows clearly the dominant frequency at a slice in time, which has an assumed relationship to detonation wave speed when interpreted as the frequency of detonation wave arrival. For this experiment, the dominant frequency is 9.2 kHz, which corresponds to 1380 m/s or 57% of D_{CJ} for three co-rotating detonation waves for the fueling conditions of this experiment. Visible on the spectrogram is the period of 'sparks on', during which ignition and detonation stabilization occurs. A shutdown transient in frequency content is also apparent at the end of the combustion phase of the experiment corresponding to when the propellant injection valves are closed.

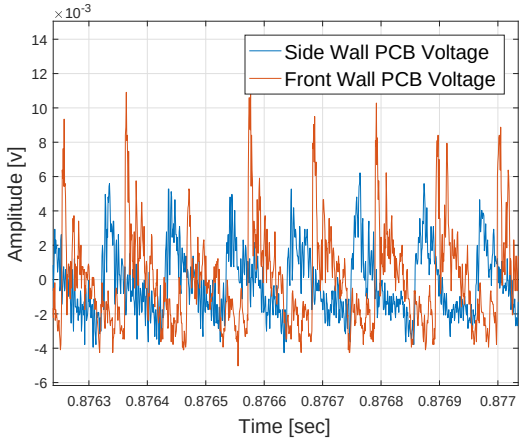

Figure 2.18: Raw signal from front and side wall PCBs.

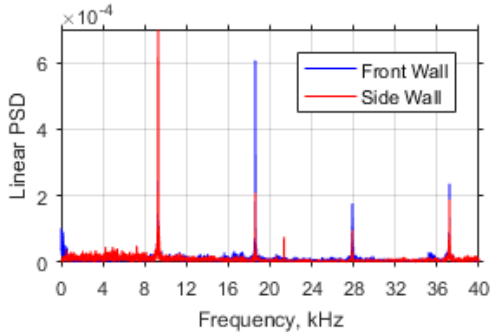

Figure 2.19: Linear PSD of PCB time signal. Dominant frequency is 9.3 kHz, corresponding to 86% of D_{CJ} with two co-rotating waves.

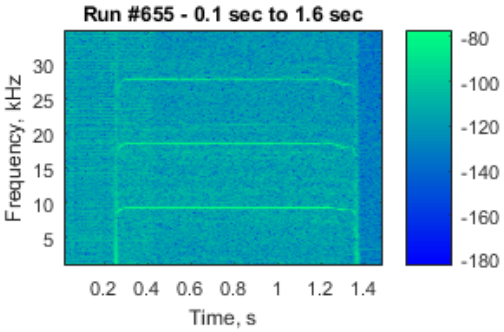

Figure 2.20: Spectrogram showing frequency history throughout the experiment.

2.2.3 Backpressure Sweeps

In this sweep of backpressures, several experiments were conducted from atmospheric pressure down to 3.7 kPa at a nominal mass flux of 26 kg/m^2/s (130 g/s). The pressure history for axial pressure stations are given in Fig. 2.21. At the axial station at the front endwall ($z = 0$cm, Fig. 2.21), the operating pressures are consistently independent of backpressure (within noise). At the next axial station, $z = 2.7$cm, the operating conditions are still consistent with the exception of the experiment that began with the highest backpressure. For this case, the pressure during steady operation is slightly higher than those of the other runs. Furthermore, this pressure tends to track upwards through time, ending at a pressure level about 10% higher than at the onset of combustion.

At the end (temporal end, not spatial end) of the experiment, the pressure level at this axial station assumes that of the dump volume. Moving further downstream, the collection of pressures remain qualitatively unchanged until the $z = 10.5$cm station. At this location, a second pressure trace lifts off of the common operating point for the sensors at this location. Similarly, at the last axial station, three pressure traces are now not in agreement with the common operating point. There is is consistent behavior among the experiments where the initial backpressure was less than 15 kPa. By changing the backpressure for the same chemistry and mass flux, the axial location at which the combustor becomes insensitive to backpressure changes.

The axial pressure profile of the engine during steady operation (taken at 2.5 seconds for all axial profile plots) is displayed in Fig. 2.22 and the corresponding pressure ratios are plotted in Fig. 2.23. As the backpressure is lowered below a threshold value, the normalized axial pressure profiles converge to a single normalized axial static pressure profile for the given mass flux and chemistry. Inferred is that the engine becomes insensitive to backpressure after dropping below a certain backpressure threshold. Consistent trends at 50, 150, and 200 g/s have also been observed and documented. Resultant profiles from these mass flux conditions are highlighted in Figs. 2.26 and 2.27. Note, however, that for these experiments at different mass flux conditions, pressure at the front endwall was not recorded. Therefore these comparisons are made by normalizing the next available station: $P_{z=2.7cm}$. While the absolute pressures through the combustor at the varying mass flux conditions do vary, the normalized profiles agree well, indicating that the experiments in which the combustor pressures are insensitive to backpressure have self-similar axial static pressure profiles regardless of mass flux.

Table 2.3: Summary of backpressure sensitivity experiments.

Run No.	ER	$\dot{m}$ (g/s)	BP (kPa)	Combustor Sensitive	Front Endwall Sensitive
739	1.13	132	20.8	Yes	No
740	1.08	137	1.60	Nonreactive	Nonreactive
741	1.08	137	9.55	No	No
742	1.10	137	14.6	No	No
743	1.11	136	17.3	No	No
744	1.11	135	26.6	Yes	No
745	1.16	129	33.6	Yes	Yes
746	1.11	135	33.9	Yes	Yes
747	1.09	134	48.5	Yes	Yes
748	1.15	128	68.7	Yes	Yes
749	1.08	133	69.2	Yes	Yes
750	1.11	138	7.42	Nonreactive	Nonreactive
751	1.13	136	9.10	No	No
752	1.12	134	12.4	No	No

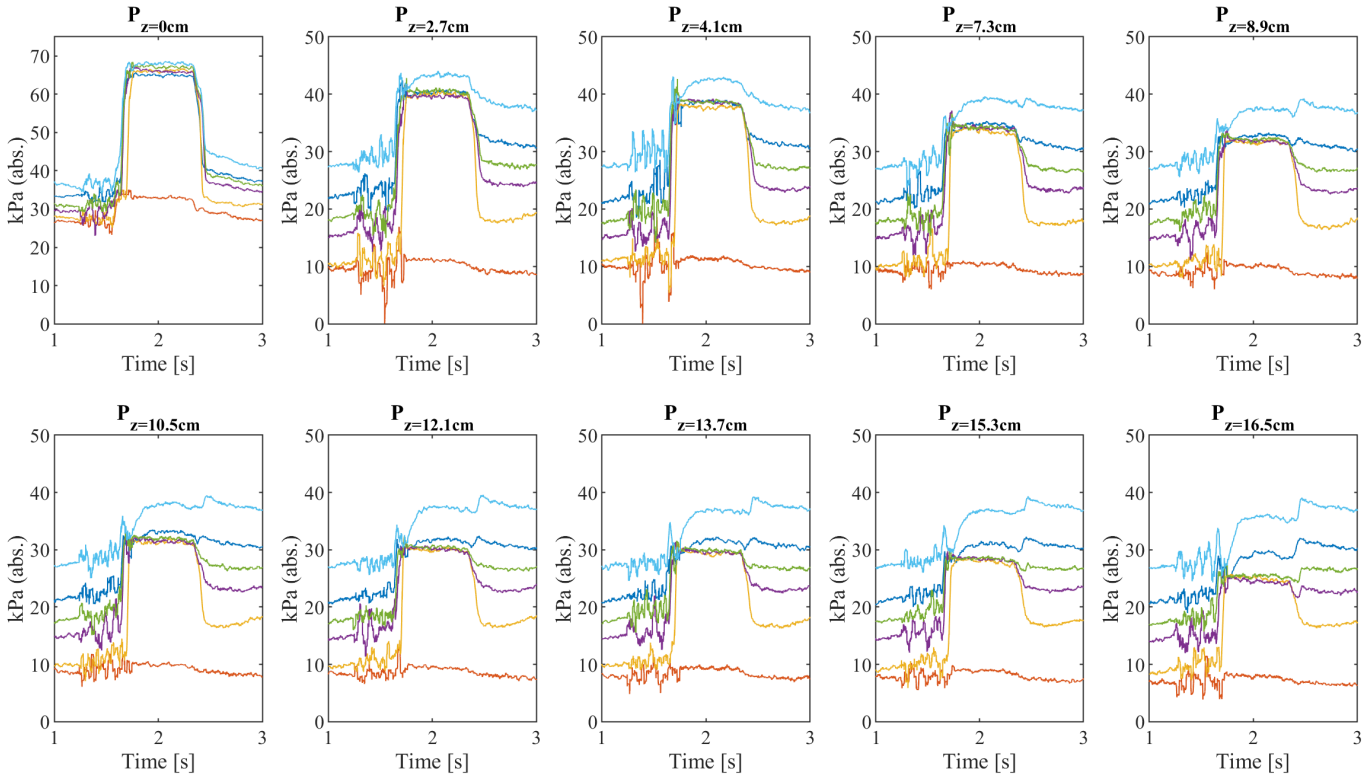

Figure 2.21: Pressure-time history for all instrumented axial stations in the 154-mm RDE. The station locations are measured by axial distance behind the front endwall. The nominal ER is 1.1 and the nominal mass flux condition is 26 kg/m^2/s.

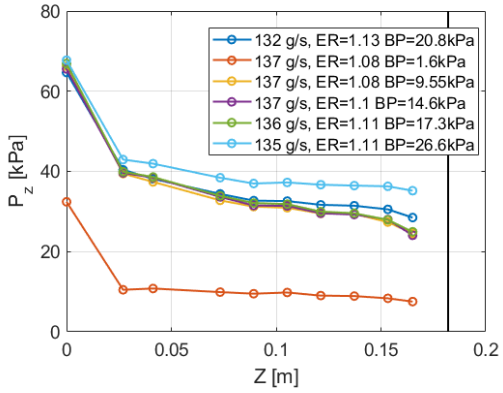

Figure 2.22: Absolute pressure along combustor length. For this data set, the mass flux is 26 kg/m^2/s. The vertical black line shows the location of the end of the constant-area annular duct. The trace with the lowest pressures corresponds to a non-reactive, cold-flow run.

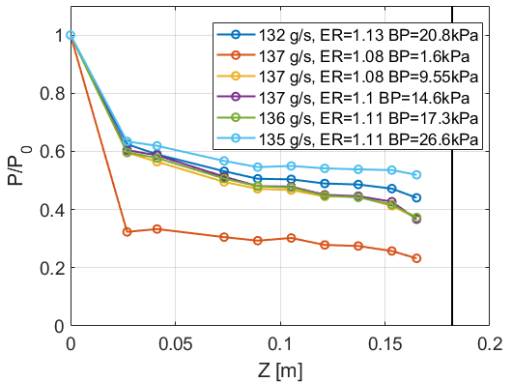

Figure 2.23: Axial pressure profile, normalized by $P_{z=0cm}$, for 26 kg/m^2/s data set. The vertical black line shows the location of the end of the constant-area annular duct. The trace with the lowest pressures corresponds to a non-reactive, cold-flow run.

We now compare spectrograms generated from data when the RDE was operating under backpressure-insensitive conditions versus operating in a backpressure-sensitive (including the pressure at the front endwall of the engine) regime. Figures 2.29 and 2.31 show spectrograms from runs with backpressures of 4 kPa and 35 kPa, respectively. The higher backpressure run exhibits persisting sideband frequencies, whereas that of the lower backpressure run does not. Furthermore, the dominant detonation frequency discretely changes between these operating backpressures. The PSD plots of these two experiments, Fig. 2.28 and Fig. 2.30, show that the dominant frequency shifts from approximately 7 kHz (with no appreciable sidebands) to 9 kHz (with sidebands at 6.5 and 11.5 kHz). In at least one scenario, the transition from three co-rotating detonation waves to two detonation waves was observed by changing backpressure exclusively. These results expand the known dependence of RDE wavenumber to backpressure, along with equivalence ratio and mass flux.

2.2.4 Backpressure Insensitivity

With the mass flow rate and fueling conditions for a specific experiment known, an estimate of the axial Mach number upstream of the heat release zone, denoted M_1,

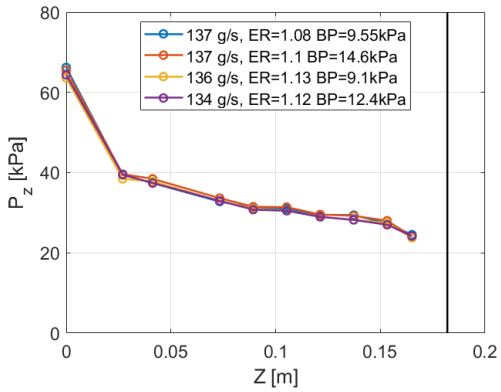

Figure 2.24: The static pressure trace for backpressure insensitivity for a set mass flux of 26 kg/m^2/s and equivalence ratio of 1.1.

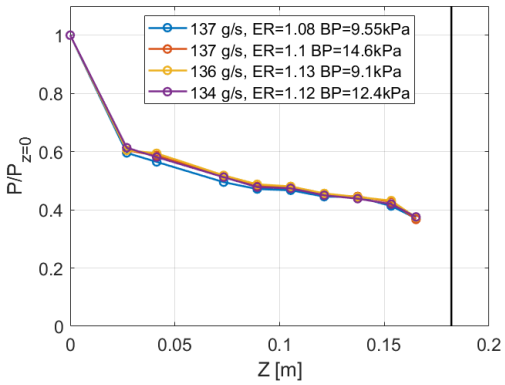

Figure 2.25: The normalized static pressure trace for backpressure insensitivity for a set mass flux of 26 kg/m^2/s and equivalence ratio of 1.1.

can be found. In [67], a type-K thermocouple was inserted through the front endwall of the 154-mm RDE to determine an estimate for temperature upstream of the heat release zone. Using a conservative estimate (1300 Kelvin) from examination of trends presented in [67], plotting experimentally obtained M_1 against the ratio P_b/P_1 (Fig. 2.32) yields a correlated description of the inlet conditions for these firings. The criteria for backpressure sensitivity/insensitivity is the presence or absence of a 'top hat' signal having a relatively constant combustor pressure for the duration of the hot-fire portion of the experiment (such as in Fig 2.15). For each experiment plotted, traveling waves do exist within the combustor, though their coherence is widely varied. For the experiments that are insensitive to backpressure, the time-averaged inlet Mach numbers (M_1) fall within a narrow range of Mach numbers centered around $M_1 \approx 0.26$ for all runs, regardless of the mass flux. This Mach number is shown as a vertical dashed line. The shaded region bounded by dashed lines indicate the region in which the transition from sensitive to insensitive occurs (determined by the resolution of the backpressure set-points for the set of experiments).

Note that while generally experiments can be classified as sensitive or insensitive to an imposed backpressure, there exists subclassifications within the realm of sensitivity. As seen in Fig. 2.21, for some experiments, the engine could operate in a regime where the exit of the combustor is sensitive to backpressure, but the pressure on the front

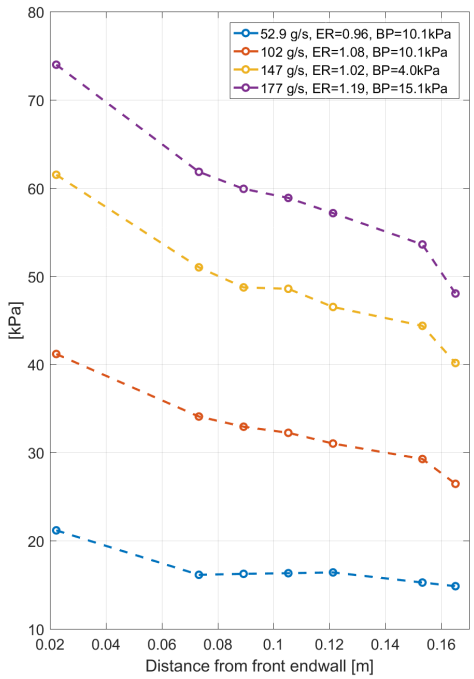

Figure 2.26: Absolute pressure along combustor length for all mass flux conditions tested. Front endwall data was not available for these experiments.

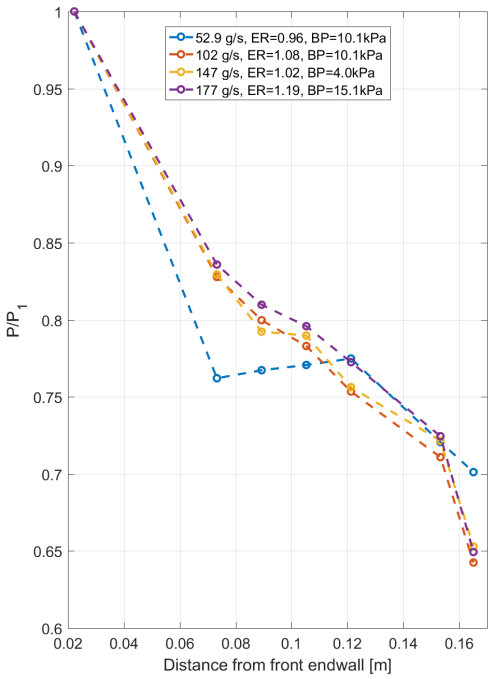

Figure 2.27: Axial pressure profile, normalized by $P_{z=2.7cm}$, for all mass flux conditions tested. Note that this normalization is different others presented in this chapter in that the normalizing pressure is the next available after the front endwall.

endwall of the engine may remain unchanged. Therefore, three classifications exist: (i) backpressure insensitive, (ii) backpressure sensitive *within* the combustor, and (iii) backpressure sensitive *throughout* the combustor.

2.2.5 Discussion

The experimental backpressure sweeps explicitly defined an envelope of backpressure insensitivity. For the firings that were insensitive to backpressure, the normalized time-averaged axial static pressure distribution is independent of the mass flux and detonation wave number, as evidenced in Fig. 2.27. The experimentally found critical pressure ratio P_b/P_1 for backpressure insensitivity is approximately 0.6 (Fig. 2.32), which corresponds to a fixed time-averaged inlet Mach of $M_1 \approx 0.26$. To contrast

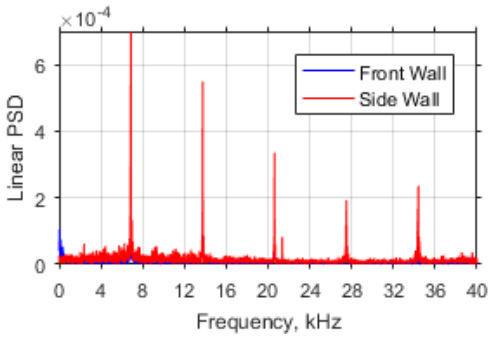

Figure 2.28: PSD of backpressure-insensitive run. The dominant frequency is 6.8 kHz, corresponding to two co-rotating detonation waves traveling at 64 % of D_{CJ}.

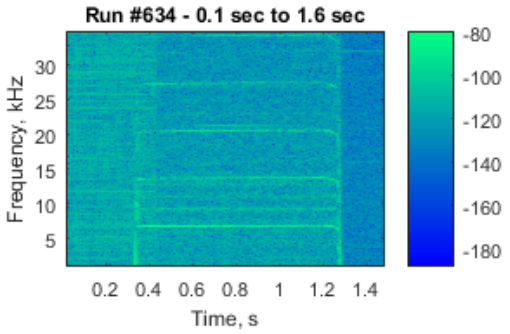

Figure 2.29: Spectrogram of backpressure-insensitive run.

this, for runs that are sensitive to backpressure, the inlet Mach varies dramatically. The proposed mechanism for the backpressure insensitivity is axial choking of the RDE flow at or near the end of the straight annulus. The presented results point to the axial choking process occurring in the steady state, despite the flow having transient small-scale multi-dimensional structure.

Once the engine is axially choked, no further decrease in backpressure can affect the upstream flow conditions. Because a further decrease in backpressure is communicated via a rarefaction wave (which propagates upstream at speed $u - a$), the wave cannot travel past the sonic point where $u = a$. However, if the backpressure is raised beyond the threshold for insensitivity, the disturbance can travel upstream as a compression wave or shock at a speed faster than the sonic velocity. The upstream propagating compression wave then alters the upstream pressure distribution and lowers the axial Mach number. As the backpressure increases, so does the upstream pressure, causing progressive upstream movement of the axial position at which the combustor pressure departs from the 'top hat' profiles. This behavior is exhibited in the data for backpressure-sensitive versus insensitive runs.

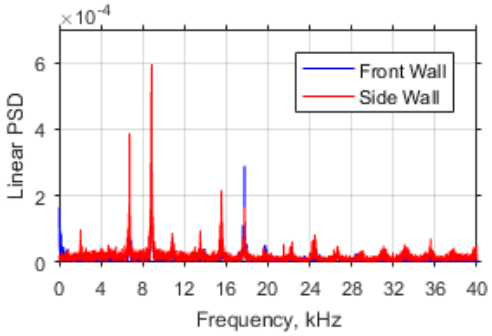

Figure 2.30: PSD of backpressure-sensitive run. The dominant frequency is 8.9 kHz. With three co-rotating waves, this frequency corresponds to 57% of D_{CJ}. Note the presence of sidebands.

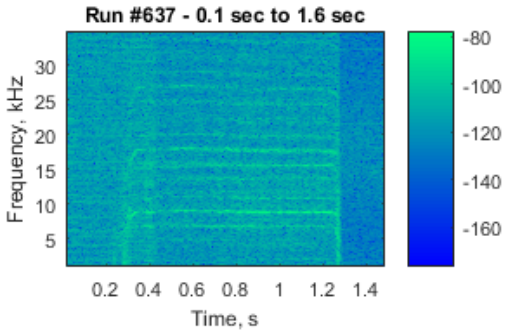

Figure 2.31: Spectrogram of backpressure-sensitive run.

1-D Gasdynamic Approximation

As the detonation waves pass by slow-response pressure probe, the probe is pressurized and then relaxes to form a time history like that of Fig. 2.18. In the time average, the passage of the detonation wave raises the pressure level at that axial station, although the magnitude of the peak pressure as the detonation wave passes is lost. In the steady condition, the pressurization from the detonation waves provide the axial pressure gradient that drives the initially subsonic flow to the sonic condition. Looking upstream of the detonation zone, the time-averaged pressure, P_1, is increased from the detonation. The ratio of the sufficiently low back pressure to the upstream pressure, P_b/P_1 is maintained at a value below that of the critical ratio required for choking of the axial flow. This ratio can be calculated from an axial momentum balance:

$$\frac{P_{critical}}{P_1} = \frac{1 + \gamma_{reactants} \cdot M_1^2}{1 + \gamma_{avg} \cdot 1^2} \tag{2.1}$$

With the values compiled from the data ($M_1 = 0.26$, $\gamma_{avg} = 1.3$, and $\gamma_{reactants}$ calculated from the inlet mixture), an estimate for the critical pressure ratio from Eq. (2.1) is approximately 0.46. In Fig. 2.32, this value is displayed as a red horizontal dashed line together with the region where backpressure sensitive transitions to insensitive.

Supposing the flow of the RDE to behave as a quasi-steady, constant-area duct (with

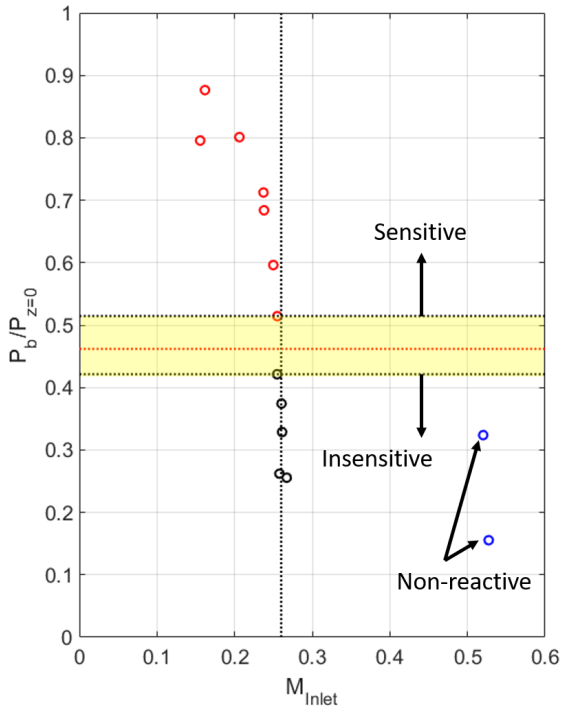

Figure 2.32: Static pressure ahead of detonation zone versus axial Mach. Red indicates backpressure sensitivity and black indicates insensitive runs. The vertical dashed line marks where $M_1 = 0.26$, the estimate for time-averaged inlet Mach. The shaded region bounded by dashed lines indicate the region in which the transition from sensitive to insensitive occurs. Using the axial momentum balance for the inlet Mach of 0.26, an estimate of the boundary is plotted as a horizontal dashed red line at a pressure ratio of 0.46.

control surfaces 1 and 2 specified near the entrance and exit), the cross-sectionally averaged energy is reduced to the standard 1-D steady energy equation:

$$\left(h_s + \frac{u_z^2}{2}\right)_2 - \left(h_s + \frac{u_z^2}{2}\right)_1 = h_{f,1} - h_{f,2} = Q_{1\to 2} \tag{2.2}$$

where $Q_{1\to 2}$ is the total chemical energy released between 1 and 2, h_s is sensible enthalpy, h_f is enthalpy of formation, and u_z is the velocity of the flow in the axial direction.

Following the standard procedure of expressing the Eq. 2.2 in terms of M_1 and M_2, and

setting $M_2 = 1$, this relationship becomes:

$$q^* \equiv \frac{Q_{1\to 2}}{c_p T_1} = \frac{\left(M^2-1\right)^2}{2\left(\gamma+1\right)M_1^2} \tag{2.3}$$

The subsonic solution of Eq. 2.3, or the lower CJ Mach number, is given by:

$$M_{CJ}^- = M_1 = \sqrt{1+\frac{\gamma+1}{2}q^*} - \sqrt{\frac{\gamma+1}{2}q^*} \tag{2.4}$$

Corresponding to the experimental values of $M_1 = M_{CJ}^- = 0.26$, $\gamma = 1.3$, the calculated value of q^* is approximately 2.8. If the available heat is below this, thermal choking is not attained at station 2. Besides heating, the pressure ratio of Eq. 2.1 must be compatibly lower than its critical value.

With the inlet Mach number fixed for a variety of mass flux conditions, a mechanism must exist to adjust the inflow boundary condition once the sonic condition is met in the annulus. Suppose a steady, axially choked flowfield has developed at the end of the RDE straight annulus. If the inflow heat release is perturbed in some manner to increase the heat release, the flowfield (which is no longer steady) accommodates by emitting a compression wave from the region of heat release that propagates upstream against the incoming flow. The effects are twofold. First, the compression wave alters the flow entering the region of heat release by lowering the incoming Mach number [68]. Second, as the compression wave reaches the front endwall, the nominally choked injectors can become unchoked and alter the mass flux into the engine, as seen in many recent experimental and numerical studies [59, 54, 53, 55, 51]. This interaction of compression waves with injectors provides a negative feedback mechanism that ultimately results in pseudo-steady operation of the axially choked RDE. In the context of the detonation waves within the annulus, these compression waves can be regarded as oblique shocks attached to the spinning detonation wave front. The oblique shocks extend both upstream and downstream of the detonation waves. The pressure rise across the oblique shocks as they pass the injector temporarily unchokes the injector, potentially even allowing for backflow should the shocks be strong enough or the injectors soft enough. Despite the proposed intermittency of the injectors, the time average of M_1 remains fixed.

Note that there are three choking points in the RDE: (1) axial choking points (for

backpressure insensitive experiments), (2) nominally choked injector exits, and (3) the CJ point behind the detonation waves relative to their spinning front.

2.3 Area Ratio Effects

Recent computational [59, 54, 55] and experimental [69] studies have identified RDE injector-to-annulus Area Ratio (AR) as a key parameter in establishing stable and high-performance RDE operation. Injectors fed by constant-pressure plenums can only continuously provide positive mass flux into the combustion chamber when the pressure inside the annulus is lower than that of the plenum. Because of the local pressure rise associated with detonative heat release, injector blockage or backflow is possible. In RDEs with low AR, blockage and backflow are less likely to occur as these injectors are more stiff and resistant to downstream fluctuations (compared to a high AR engine operating at the same mass flux condition). This robust injector operation comes at a cost of significant pressure loss across the orifices, which in turn limit the pressure rise associated with the detonation waves. However, engines with higher AR and lower plenum pressures (for the same mass flux condition) are more susceptible to coupling between the injectors and the detonation waves.

In this set of experiments, presented are data relating thrusting pressure, injector pressure ratio, and global equivalence ratio (ER). Within the context of these results, discussed are RDE system-level coupling and RDE performance and the impact that AR has on these metrics.

2.3.1 Experiments

The goal of the presented experiments is to establish the operability curves of the 76-mm RDE with respect to the different injector configurations (AR). The operability curves are defined in 3D space with ER, thrusting-pressure-based specific impulse, and injector pressure ratio as dimensions. All experiments are run in a regime that is backpressure insensitive (see Section 2.2 and [70]). For the presented experiments, this backpressure was set to 0.5 atmospheres. The RDE configuration used is listed in Table 2.4 (RDE features) and Table 2.5 (injector specifications). The core length used was the longest

Table 2.4: 76-mm RDE configurations

Mean diameter	71.2 mm
Flow OD	76.2 mm
Flow ID	66.2 mm
Annular gap	5.0 mm
Annular cross sectional area	1120 mm^2
Combustor lengths	12.7mm, 102 mm, 152 mm
Area Ratios	0.135, 0.188, 0.240

core available, i.e., 152 mm in length.

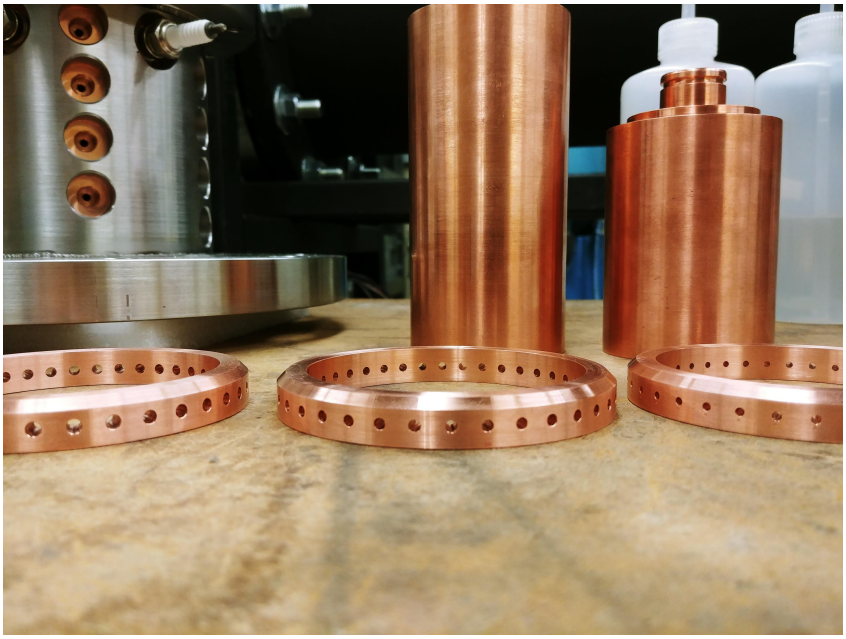

Figure 2.33: Three oxygen injection rings with different orifice sizers are shown. These are the actual pieces used in the presented experiments. The largest orifices (left) are 0.104" in diameter. Those of the middle ring are 0.092". Lastly the smallest orifices are 0.078" in diameter. Each ring has a fuel-side counterpart. Each ring contains 36 orifices.

The sequencing of the valves and high-speed data for all of the presented experiments in this section are shown in Figure 2.13.

2.3.2 Results

The complete time history of the combustor pressure through time is shown in Figure 2.35 corresponding to the experiment scheduling shown in Figure 2.34. Just as in the pressure-time traces of the 154mm-RDE, immediately observed is a sharp pressurization

Table 2.5: Orifice sizes used in area ratio experimental survey

	AR = 0.135	0.188	0.240
Oxidizer Ring (36x)	0.078”	0.092”	0.104”
Fuel Ring (36x)	0.047”	0.055”	0.063”

of the combustion chamber associated with ignition (at approximately 1.5 seconds) followed by the 0.5 second duration firing and ramp-down to ambient backpressure. As was the case for the 154-mm RDE, the pressure measured at $z = 0$ meters is taken to be the thrusting pressure, as this pressure is also measured at the front endwall (perpendicular to the flowpath).

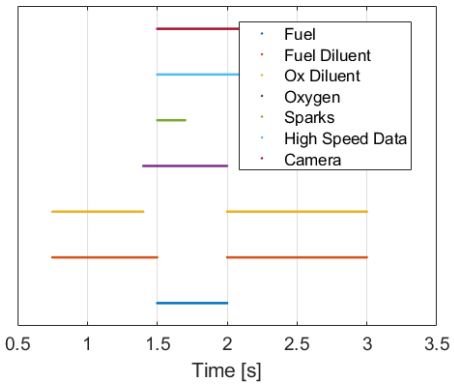

Figure 2.34: Valve states and trigger signals for a single hot firing.

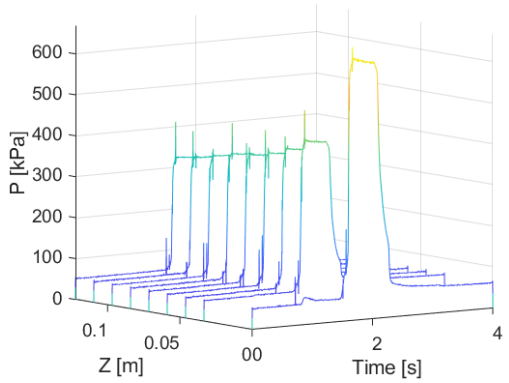

Figure 2.35: Complete space-time history for a typical experiment.

Operability Curves

For each experiment, the thrusting pressure is recorded alongside the static pressures inside the oxygen and fuel plenum chambers. The operability space is defined with the axes of ER, ratio of thrusting pressure to mass-flow-weight-averaged plenum pressure, and thrusting-pressure-based specific impulse. In reducing the data to these three coordinates, a dependence on mass flux is (conveniently) not observed.

Figure 2.36 summarizes the pressure ratio across the injectors for the three AR tested. The data points presented each represent a successful firing of the engine that lead to a traveling combustion wave mode. All mass flux conditions tested are presented in this figure. Note the wide range of ER operability - for the AR of 0.135, the engine successfully ran from ER of 0.13 to 3.5. For the two other AR configurations tested, the

full limits of stable operation were not tested, but rather a subset of the parameter space to determine local maxima in the operability curves. The pressure ratio is highest (0.82) for the largest AR (0.240) at a global ER of approximately 0.6. As AR is reduced, this pressure ratio drops. For the lowest AR tested (0.135), this peak in pressure ratio (0.5) occured at a global ER of approximately 1.0. The trends in thrusting-pressure-based specific impulse, visible in Figure 2.37, show consistent behavior across the injectors: each delivers approximately the same peak performance. Peak specific impulse was 235 seconds at a ER of 1.1 and an AR of 0.135. The 3-D operability space is presented in Figure 2.38. Note that the specific impulse reported is based on thrusting pressure only - no gains from nozzles or geometric throats are included.

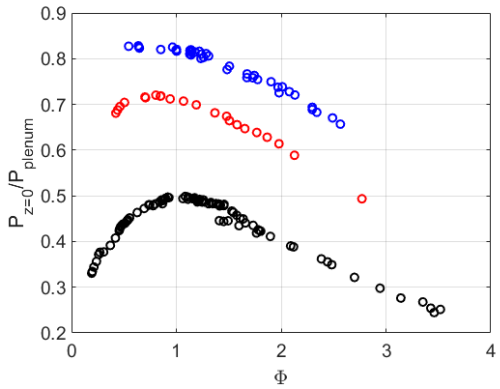

Figure 2.36: Ratio of thrusting pressure to mass flow rate weighted average of the plenum pressures for all mass flux conditions tested. (Black = AR of 0.135, Red = AR of 0.188, Blue = AR of 0.240)

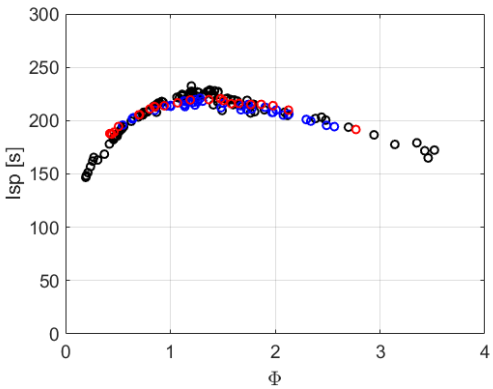

Figure 2.37: Thrusting-pressure-based specific impulse versus ER for all mass flux conditions tested (150 - 350 g/s). (Black = AR of 0.135, Red = AR of 0.188, Blue = AR of 0.240)

Plenum Feedback

The timing of the introduction of oxidizer and fuel into the engine is offset in all experiments by 200 ms. During this time, the oxidizer plenum pressures stabilize and reach quasi-steady flow rates (provided the upstream gas supply matches the desired flow rate). After the oxidizer flow stabilizes, the fuel is introduced and the ignition system is turned on. This experiment schedule has the added benefit that the degree of back-pressurization of the oxygen plenum chamber can be directly observed. In Figure 2.39, two pressure traces are shown of runs with identical fueling parameters. One run

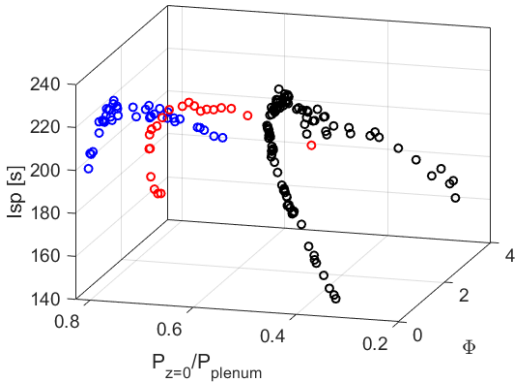

Figure 2.38: Operability curves in I_{sp} - pressure ratio - ER space.

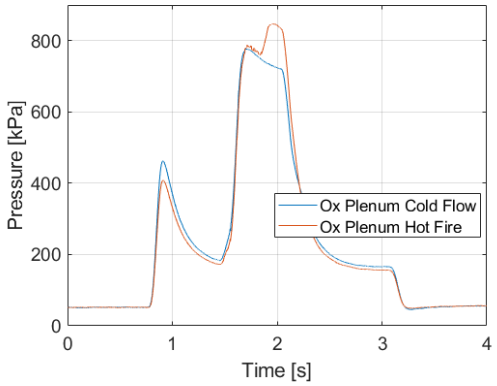

Figure 2.39: Back-pressurization of the oxygen plenum chamber.

did not ignite while the other successfully lit about halfway through the propellant flow period. Of note is the immediate and significant back-pressurization of the plenum by coupling with the local pressure rise associated with the traveling combustion wave. The pressure levels in the plenum chambers pre- and post-ignition can be quantified to show a degree of coupling or back-pressurization.

Table 2.6 lists example runs from all AR conditions tested where explicit back-pressurization was observed. For each listed run, a plenum pressure before (cold) and after (hot) ignition was recorded. The percent difference in these pressures is given in the last column. For the lowest AR, the back-pressurization of the oxygen plenum is on the order of 10% of the cold flow plenum pressure. At the highest AR, the oxygen plenum pressure approximately doubles once the engine is running. For all of these runs, the orifices are choked until the time of ignition. Note that similar numbers for the fuel plenum cannot be extracted from this data set - this is because the introduction of fuel and ignition are scheduled too close together in time to allow for the fuel plenum pressure to stabilize before ignition.

Traveling Wave Topology

The traveling wave topology varied significantly between the different AR and along the respective operability curves. The greatest variation of wavenumber, direction, and speed was observed for the AR of 0.135. However, counter-propagating waves were observed for nearly every experiment. In fact, co-rotating waves were an oddity for this

Table 2.6: Oxygen plenum back-pressurization

Run No.	AR	ER	$\dot{m}$ (g/s)	Cold (kPa)	Hot (kPa)	%-diff
122	0.135	1.49	235	742	852	15%
140	0.135	2.44	259	784	898	14%
162	0.135	1.21	256	947	1040	10%
166	0.135	1.27	298	1150	1240	8%
178	0.135	1.24	180	651	713	10%
221	0.188	1.48	318	621	915	47%
224	0.188	1.58	228	395	620	57%
233	0.188	0.94	193	397	538	35%
182	0.240	1.73	208	249	508	104%
189	0.240	1.18	171	223	406	82%
198	0.240	1.13	163	220	437	99%
196	0.240	1.78	212	250	505	102%
215	0.240	1.67	262	344	649	89%

injector. Although no general trend of number of waves and properties was found to exist as a function of the operability curves, presented here is a summary of the modes found and where they exist within operability space. Figures 2.40 and 2.41 map the runs whose wave behavior is to be detailed within the context of this variation of area ratio. For each detailed experiment, presented are several features. First, for each run a θ-time plot is shown. This corresponds to the kinematics of the waves in the laboratory reference frame. Next, the waves are shifted into the reference frame of one of the waves, such that the behavior of the tracked wave appears steady. The luminosity integrated *across the entire annulus* as a function of time is displayed in-sync with these space-time plots. The luminosity around the annulus corresponding to the vertical white lines in the space-time plots is shown on the bottom of each summary figure after shifting to a zero-mean magnitude. The spectral content of the luminosity through time is shown as a spectrogram. Likewise, the 2-D Fast Fourier Transform of the space-time history is displayed showing dominant frequency in time (corresponding to speed) and in space (corresponding to a count of waves in the domain).

Although the behavior of the waves through these experiments varied widely, several unique features of the structure of the waves for these experiments deserve mentioning. First is the regular pattern formed by the presence of counter-rotating waves, as in Figs. 2.42 and 2.44. In Run # 82, the regularity of the wave propagation forms a repeating

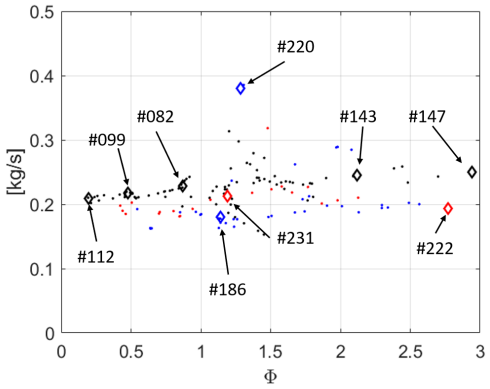

Figure 2.40: Location of detailed runs in the context of fueling and mass flow rate.

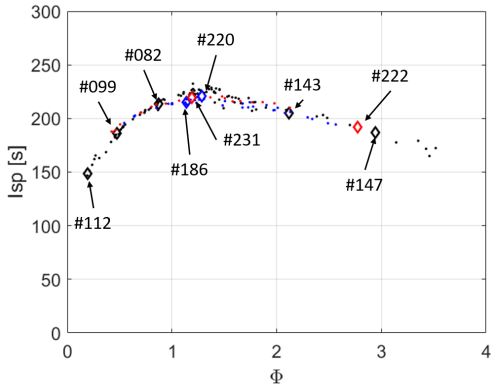

Figure 2.41: Location of detailed runs with respect to thrusting-pressure based specific impulse.

structure of thee co-rotating waves (clockwise or decreasing in θ) and a periodic switching between three and four waves traveling in the opposite direction. The 2-D frequency content of the experiment (Fig. 2.42) shows this explicitly: there exist two dominant frequencies corresponding to three and four waves in the upper half of the spectrum (not to mention a faint trace of a 5th wave). Not only is the wave propagation regular, but also the periodic transitions between three and four counter-propagating waves. For less-ordered detonation waves, such as those in Figure 2.44, the 2-D frequency content tells a similar story: although 6 co- and 6 counter-propagating waves are dominant for the experiment, significant 'sidebanding' exists where secondary frequencies symmetric about the dominant frequency give rise to complex transition and collection dynamics in the experiment.

In Fig. 2.43, seen is a collection of three waves persisting through time. Though the waves are stable in that the number of waves is not changing, the relative spacing between the waves is not consistent - it appears oscillatory. Similar behavior is seen in the three wave case of 2.46, though for this case, sidebands again exist symmetric about a carrier frequency and persist through time. This phenomenon appears to extend across numbers of waves and different injectors: see Fig. 2.47.

Aperiodic traveling wave behavior is also seen in these experiments. In Fig. 2.48, mode transitions plague the 'steady state' of the engine. In the span of the 2 milliseconds shown, the experiment transitions from two co-rotating waves to two of the opposite direction,

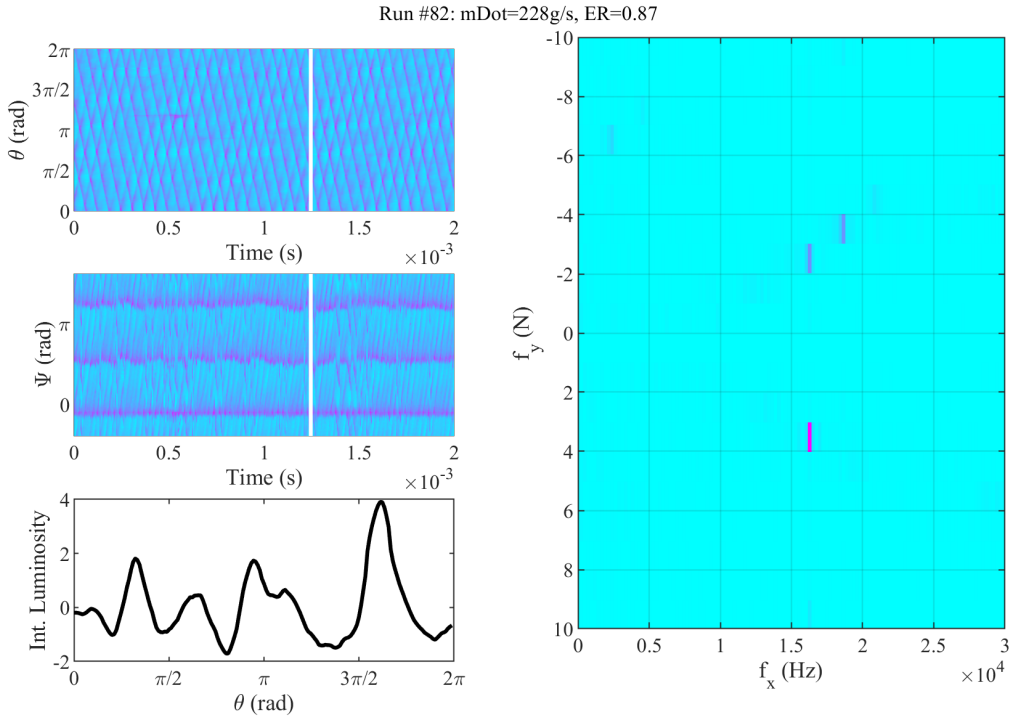

Figure 2.42: Run 082. AR = 0.135. CJ speed of the propellant is 2,319 m/s. The speed of the traveling waves are approximately 1330 m/s (57% D_{CJ}).

followed by a single wave with faint counter-propagation. However, of note is that the 2-D frequency content appears regular: the clockwise and counter-clockwise propagating behavior appear to be mirror-images of each other, despite the apparent aperiodic nature of the space-time history. In run # 186 of Fig. 2.49, traveling waves and longitudinal pulsations co-exist with similar operating frequencies. This mode corresponds to periodic plane waves similar to those of pulse jets or pulse detonation engines: a spatially uniform explosion halts the flow of propellant into the combustion chamber and simultaneously ejects exhaust rearward. Only when the injectors can recover will the combustion process begin again.

Lastly, of note is the background luminosity accompanying the traveling waves in the majority of the exhibited experiments, particularly in Fig. 2.50. In this case, although there is a single traveling wave, the wave amplitude is very shallow and its associated speed is relatively slow. Because what is captured by the high-speed camera is natural chemiluminescence from the combustion process, one can see that the shallow wave front

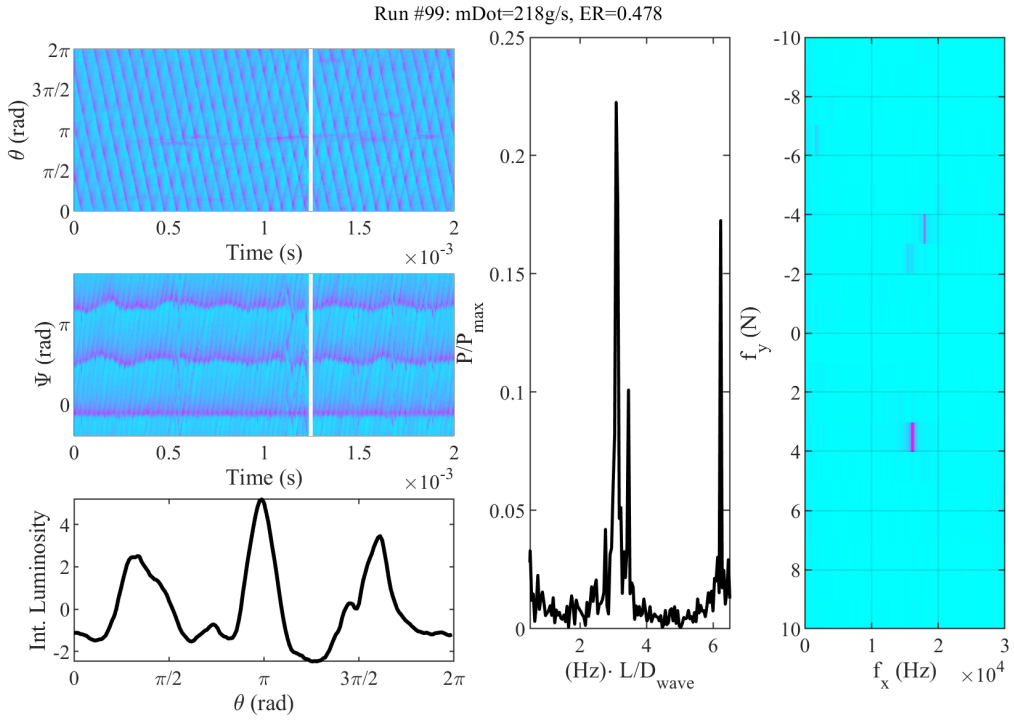

Figure 2.43: Run 099. AR = 0.135. CJ speed of the propellant is 2,038 m/s. The speed of the traveling waves are approximately 1258 m/s (62% D_{CJ}).

is accompanied by significant luminosity in the *entirety* of the annulus. The implication is that the traveling wave is likely not the sole-supplier of heat release in the engine: significant amount of propellant is being burned through deflagration.

Shortened Engine Cores

In an effort to better characterize the axial flow in the combustor for these experiments, a comparison experiment was performed with two shortened (102mm and 12.7mm) cores. In these configurations, two or more instrumentation ports are outside of the duct. Compared are three runs of similar mass fluxes and ER in Figures 2.51 and 2.52 - the blue trace is of a run with the full length (0.15 meter) flowpath. The red trace has the shortened core (0.1 meter flowpath) installed. The yellow trace is with the 12.7mm length core. Figure 2.51 shows clearly the continued expansion of the flow outside of the shortened ducts to below the ambient pressure. The magnitude of the static pressures along the axis for both experiments is similar until the duct exit. In Figure 2.52, the

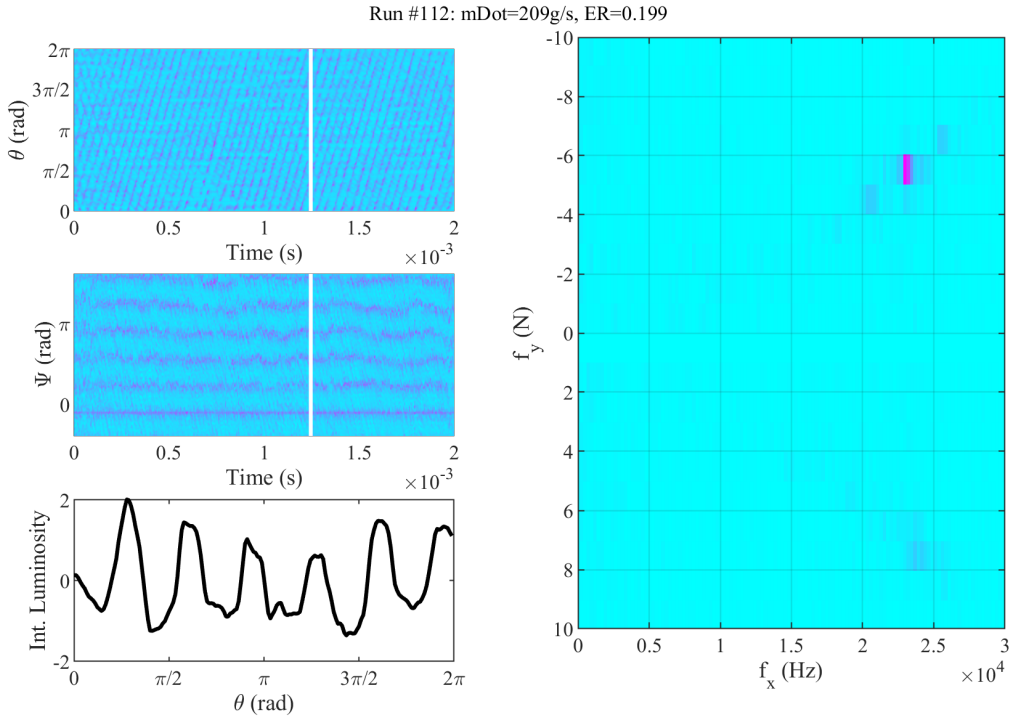

Figure 2.44: Run 112. AR = 0.135. CJ speed of the propellant is 1,683 m/s. The speed of the traveling waves are approximately 804 m/s (47% D_{CJ}).

normalized pressure traces are presented. The behavior of the two traces is qualitatively different. The slope of the trace for the longer flowpath is shallower than that of the shorter flowpath. Likewise, the pressure ratio at the last axial station is higher than that of the last station in the duct of the shorter core case (at approximately 0.1 meters). Again, note the lack of instrumentation at or near the end of the duct for the 0.15 meter flowpath cases.

2.3.3 Discussion

Thermal Choking

We can elaborate on this supposition of thermal choking from Section 2.2 further with the comparison of the three duct lengths, as shown in Figures 2.51 and 2.52. From these two figures, one can see the dramatic pressure drop outside the exit of the shortened cores to below the ambient pressure. At the end of the straight annular duct of the 102-mm core, the pressure ratio is comparable to the pressure ratio required to choke 1-D flow

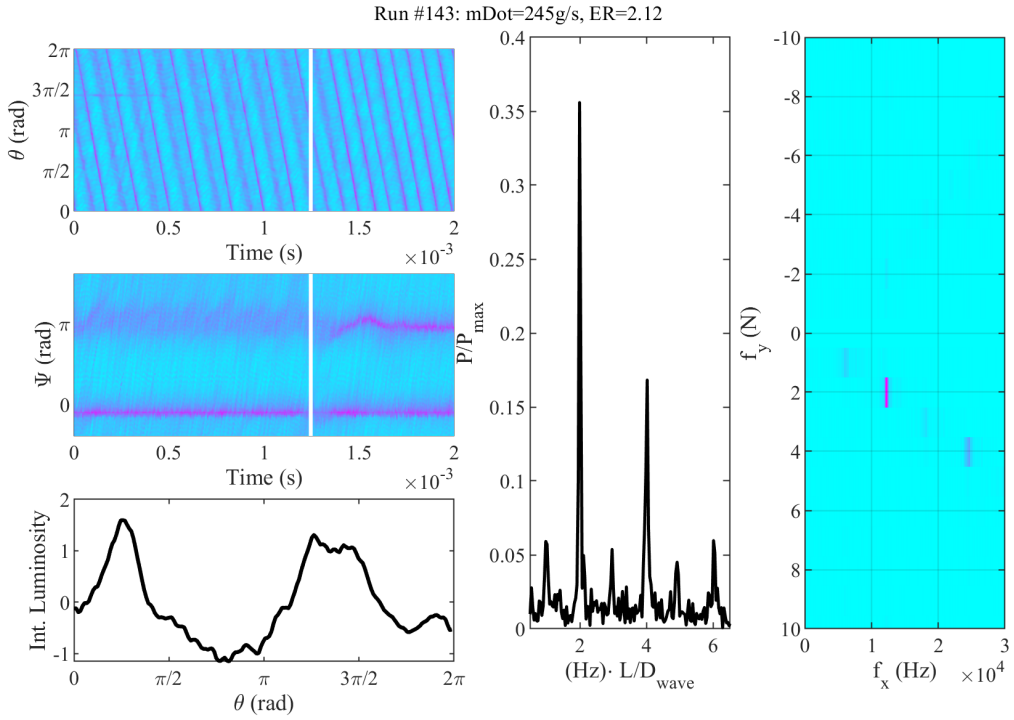

Figure 2.45: Run 143. AR = 0.135. CJ speed of the propellant is 2,629 m/s. The speed of the traveling waves are approximately 1,468 m/s (56% D_{CJ}).

from rest ($M = 0$ to $M = 1$ with $\gamma = 1.3$). At the last instrumented station for this case, the pressure is 0.06 times that of the thrusting pressure. For this flow to be subsonic would require an area constriction, not an abrupt area expansion. Therefore, concluded is that the flow in this condition is thermally choked and expanded supersonically at the abrupt area expansion at the exit of the duct.

Injector Pressure Ratio and Plenum-Wave Coupling

In this study, the injector pressure ratio is defined as the ratio of thrusting pressure to the mass-flow-averaged plenum pressures. This experimentally determined value is used as a relevant metric because this pressure ratio defines both an injection loss (pressure drop across the orifices) and a degree of coupling, as evidenced by the back-pressurization of the plenum chambers. As AR is increased, the coupling between the traveling combustion waves and the plenum chambers becomes very significant. In the case of AR = 0.240, the oxidizer plenum chamber pressure doubled at the onset of ignition.

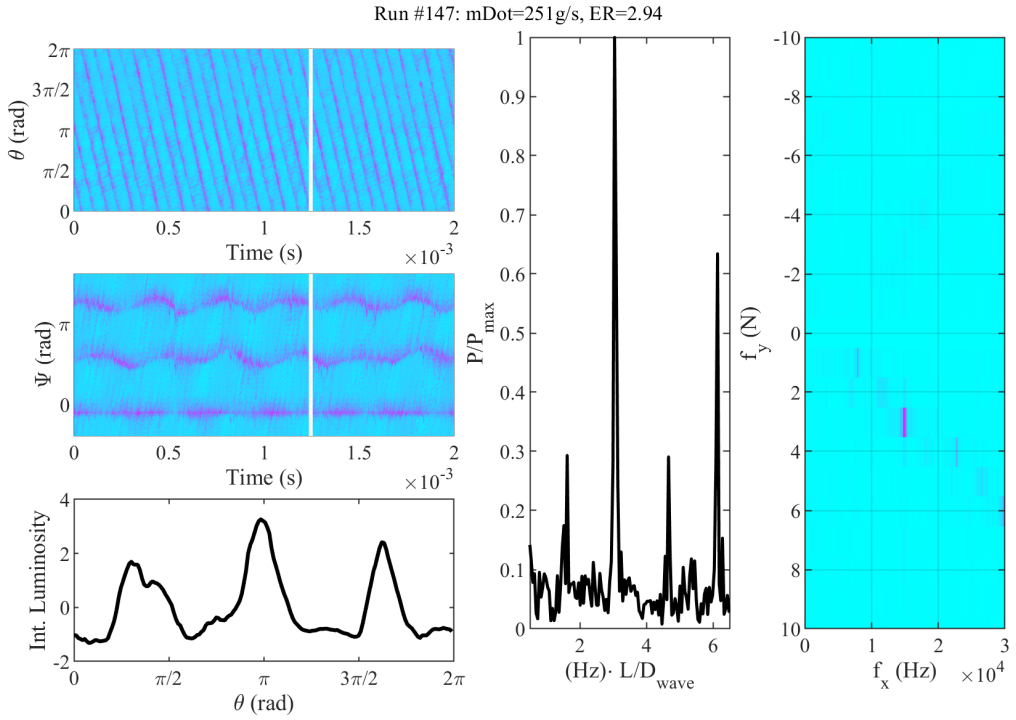

Figure 2.46: Run 147. AR = 0.135. CJ speed of the propellant is 2,401 m/s. The speed of the traveling waves are approximately 1,188 m/s (49% D_{CJ}).

This back-pressurization is present at all mass flow rates tested to date (see: Table 2.6) - indicating that this is a phenomenon that occurs regardless of the feed pressure and is instead a direct manifestation of the AR of the engine.

The increase of P_{thrust}/P_{plenum} with increase of AR (plotted in Figure 2.36) is intuitive. The mechanical restriction is reduced as AR increases, so there is greater degree of communication between the plenum and combustion chambers. The specific impulse data reported in Figures 2.37 are based on thrusting pressure and mass flow rate exclusively (no expansion factor or nozzle correction is used). The consistency in the magnitude of specific impulse can be explained by the imposition of a pseudo-boundary condition on the exit of the combustor, namely that on the time- and circumferential-average, the axial flow is thermally choked. For experiments of the *same mass flux and chemistry*, the energy input to the flow is equivalent across the different AR. Supposing such experiments across different AR to be thermally choked, the conditions at the exit of the engine are identical. Choking the duct acts as a boundary condition: it sets the upstream

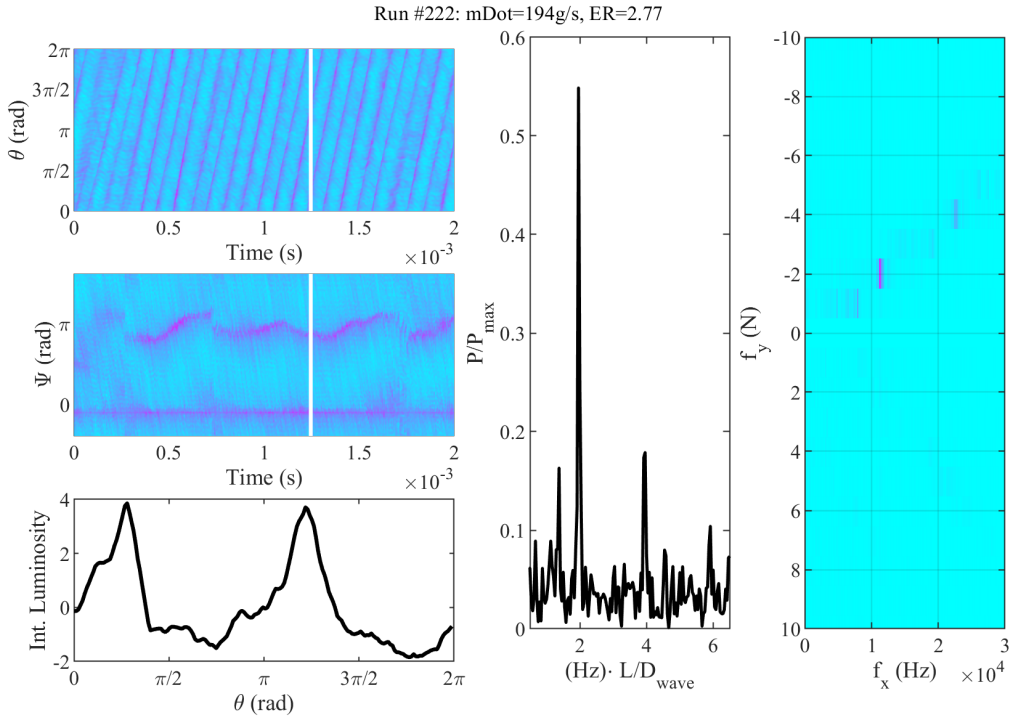

Figure 2.47: Run 222. AR = 0.188. CJ speed of the propellant is 2,472 m/s. The speed of the traveling waves are approximately 1363 m/s (55% D_{CJ}).

pressure required to steadily deliver the particular mass flow rate of the experiment. What differs between the experiments of different AR, however, is the pressure required in the plenum to deliver this consistent mass flux through the engine. For larger AR, indeed the obtained measurements of plenum pressure indicate that a higher feed pressure is required to offset the significant degree of backflow into the plenums. With soft injectors (significantly coupled plenums and combustion chamber), the backpressurization of the combustion chamber caused by thermal choking is felt all the way up to the plenums. In this manner, the front endwall pressures of the combustion chamber across different AR are similar in magnitude: the same energy release and mass flow rate fully specify the thrusting pressure required to choke the flow. The plenum pressures necessarily adjust their operating levels to accommodate the backflow and attainment of a sonic condition at the exit of the engine.

Furthermore, the orifices for the fuel and oxidizer rings are subject to the same periodic forcing (the passage of a high pressure detonation wave). However, the orifice diameters

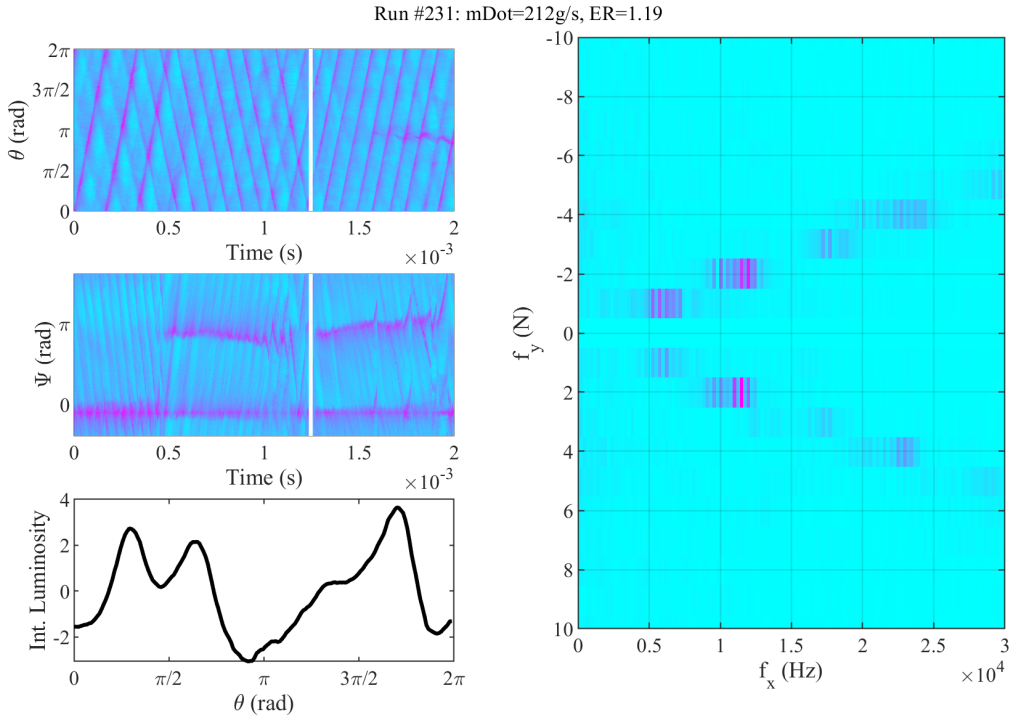

Figure 2.48: Run 231. AR = 0.188. CJ speed of the propellant is 2,478 m/s. The speed of the traveling waves are approximately 1468 m/s (59% D_{CJ}).

(and therefore aspect ratios such as length/diameter) of the fuel and oxidizer rings are not the same. Therefore, their dynamic response to the same forcing will not be the same. Similarly, as equivalence ratio is varied across experiments, the plenum pressures are adjusting to match the global mixture chemistry. The shapes of the curves in Fig. 2.36 are likely due to the mismatch of injector responses for different orifice sizes and plenum pressures.

2.4 Impinging Injector

An impinging-type injector was designed and constructed in an effort to produce consistent detonation wave behavior. The injector (shown in Fig. 2.7) features 72 pairs of orifices inclined 30 degrees to the central axis of the engine. The oxidizer orifice diameter is 0.049" and that of the fuel is 0.031" which yields an area ratio of 0.11 when mounted on the 76-mm RDE. The injector was machined out of single-piece brass and installed as a drop-in modification to the existing engine hardware. Machine drawings for the

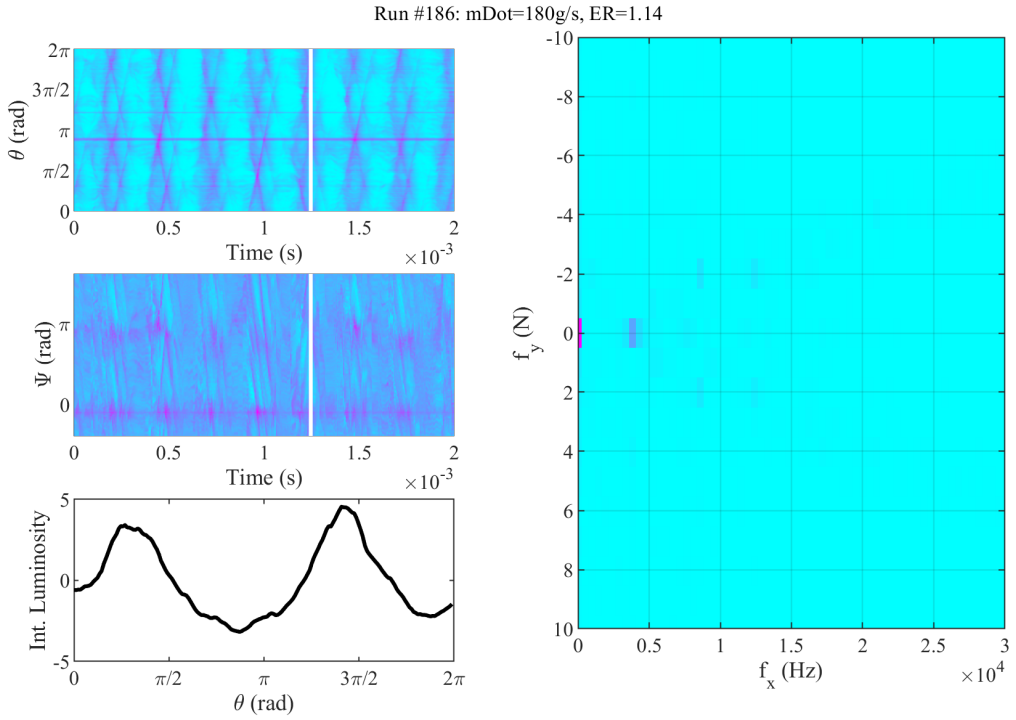

Figure 2.49: Run 186. AR = 0.240. CJ speed of the propellant is 2,455 m/s. The frequency of pulsation is 4025 Hz.

injector can be found in Appendix A. The testing presented here was purely exploratory and is incomplete. Nevertheless, the wave dynamics are of relevance to this dissertation, and as such, the results from these tests are included. The tests were conducted with a 76-mm long flowpath for a combustor aspect ratio (flowpath outside diamter-to-length) of 1.

Four experiments are shown that showcase the behavior of the detonation waves for this hardware configuration. Their operating points are shown in Figs. 2.53. The figures shown contain the same information as was included in Section 2.3, including the space-time history of the waves in the laboratory and wave reference frames and the spectral content of annulus. One can immediately see that the structure of the traveling waves are much more defined than those of Section 2.3. The luminosity wave forms are steep-fronted and decay to a low luminosity, indicating a lesser degree of parasitic deflagration when compared to the results from the radial injectors. Additionally, counter-propagation is notably absent from these experiments. The spectral

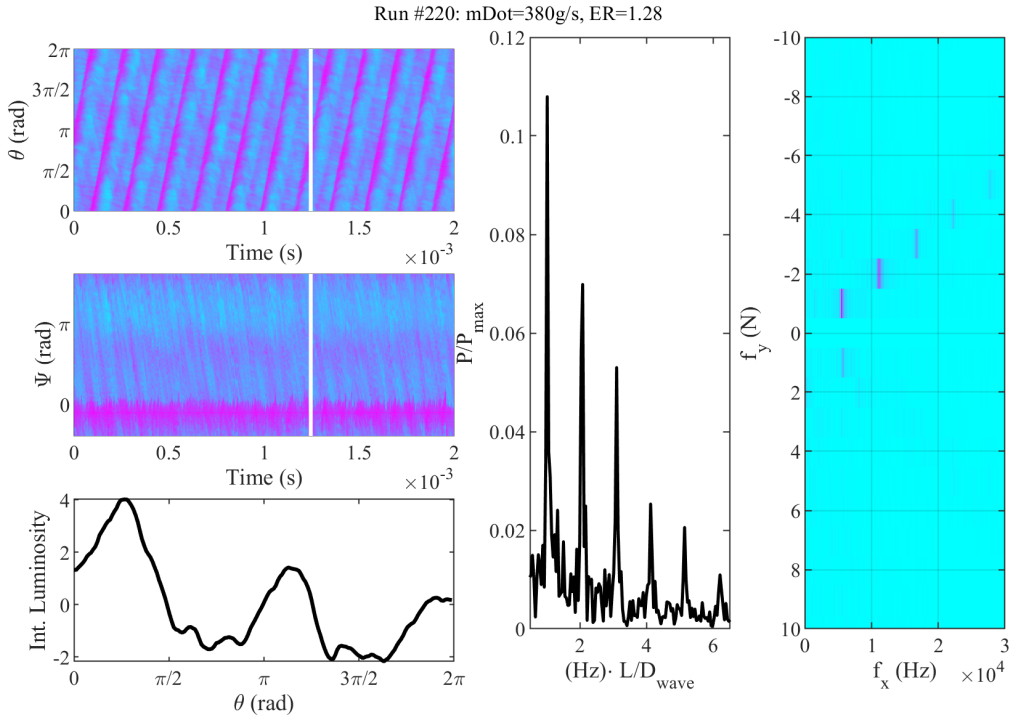

Figure 2.50: Run 220. AR = 0.240. CJ speed of the propellant is 2,514 m/s. The speed of the traveling waves are approximately 1363 m/s (54% D_{CJ}).

characteristics seen in experiments with radial injectors persist with this injector. Non-steady wave motion (such as in Figs. 2.55, 2.57, and 2.58) is accompanied by spectral sidebands that are symmetric about a dominant frequency corresponding to the average velocity of the waves. These sidebands and wave behavior are characteristic of the canonical modulational instability whereby steadily propagating waves bifurcate to time-periodic oscillation of the wave motion. These oscillations can become quite severe, as seen in Fig. 2.57. Note that Figs. 2.56 and 2.57 are from the same run: a transition from a single wave to two waves occurred during the experiment.

2.5 Transients

The experiments presented thus far all occur in a regime that is quasi-steady; that is, without drastic changes in operating condition of the combustor. However, noteworthy dynamical behavior is exhibited during transient periods. These may include ignition, the ramp-up or ramp-down of propellant into the combustion chamber, the alteration of the

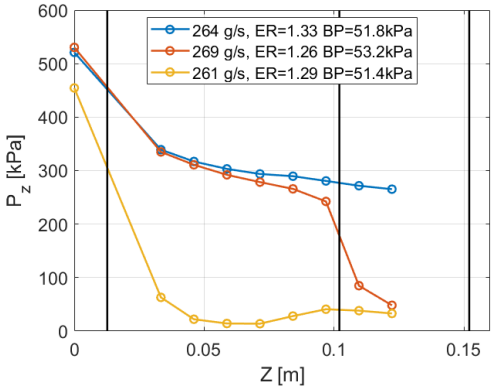

Figure 2.51: Comparison of axial static pressures for 0.15 meter (blue dots), 0.1 meter (red dots), and 0.0127 meter (yellow dots) flowpaths. The black vertical lines correspond to the exits of the cores. Note the expansion of the flow to below ambient backpressure for the shortened cores.

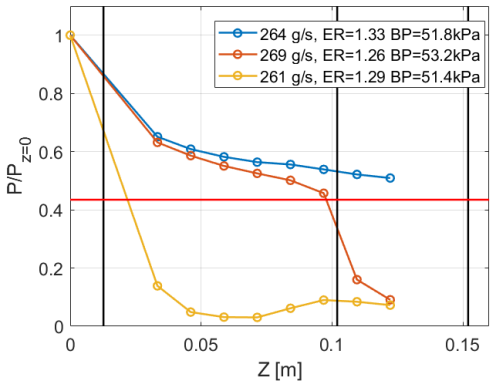

Figure 2.52: Normalized static pressure traces for 0.15 meter (blue dots), 0.1 meter (red dots), and 0.0127 meter (yellow dots) flowpath experiments. The black vertical lines correspond to the exits of the cores. The horizontal red line corresponds to the pressure ratio required to drive the flow from rest ($M = 0$) to the sonic condition ($M = 1$) for $\gamma = 1.3$.

backpressure of the combustor, or the loss of an axial choke point. During these periods of change, the the behavior of the detonation waves may change dramatically. However, as the time scales associated with the detonation waves are much shorter (several orders of magnitude) than those associated with the propellant supply, the external impetus for driving the transients are fundamentally unknown. In this section, presented are the "normal forms" for transients observed in the experiments presented in this dissertation: (i) ignition, (ii) wave nucleation, and (iii) wave destruction. These "normal forms" are presented without attached operating points or specific fueling conditions as they are canonical - the qualitative behavior of these transients is consistent across *all* observed operating conditions.

In Fig. 2.59, an observed transition from one wave to two waves during the startup transient is shown. In this mode transition, after a point of criticality, a second detonation wave forms and begins to travel around the annulus. However, the spacing between the two waves in the annulus is asymmetric, causing an imbalance in the amount of propellant consumed by each of the waves and the rate of propellant consumption. If one of the

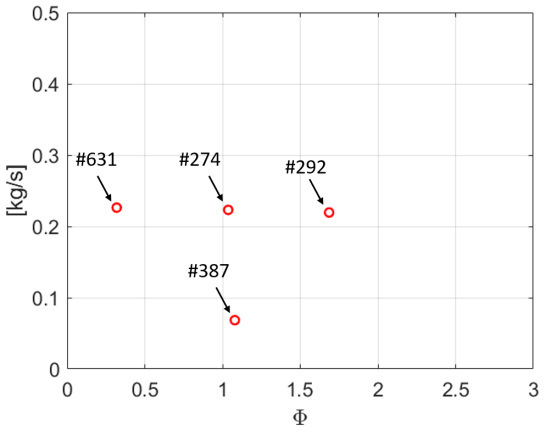

Figure 2.53: Mass flow rate and equivalence ratio for the featured impinging-type injector experiments.

waves becomes too close to the preceding wave (a phase difference between the waves of $\psi < \pi$), the trailing wave has less propellant to consume than the preceding wave. Since propellant heat release directly affects the speed of a detonation, the trailing wave begins to decelerate. The preceding wave, however, can process the remaining portion of available propellant and accelerates through this excess. In this manner, these two waves behave dispersively, where they seek a stable state with maximum and symmetric phase differences. As the transition to two waves occurs and the dynamics settle to a steady state, the wave speed reduces to about 90% of the single wave speed.

The opposite scenario occurs upon ramp-down of propellant feed at the end of each experiment. Figure 2.60 exemplifies a ramp-down transition of 2 to 1 wave over the span of about 10 ms. The two waves compete for the increasingly scarce propellant, as opposed to the case of excessive propellant exhibited in Fig. 2.59. Because of an initial perturbation in phase difference, the waves begin to exchange strength (speed and amplitude) in a regular fashion producing the exponential instability growth. As the phase difference oscillations grow, a catastrophic interaction between the waves occurs, resulting in the overrunning of the weaker wave by the stronger wave during one of the large-amplitude oscillations. After the bifurcation, the velocity of the remaining wave is about 10% higher than that of the wave prior to the instability.

Lastly, Fig. 2.61 shows a typical ignition phenomenon in the engine. After the initial spreading of an ignition kernel through the annulus, the deflagration transitions to a

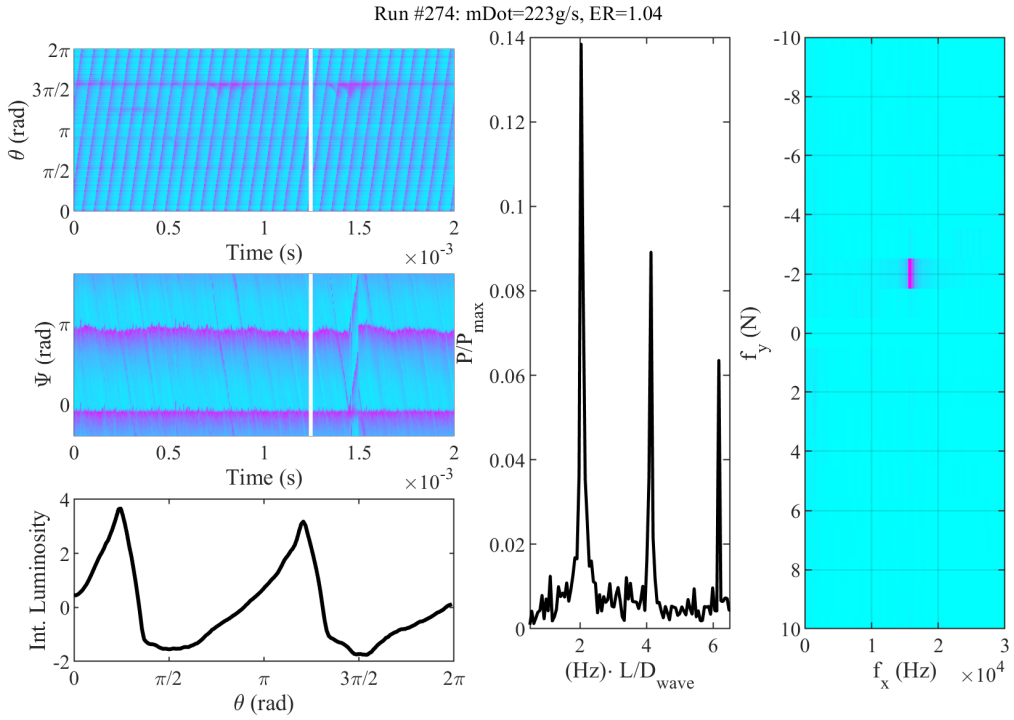

Figure 2.54: Run 274. AR = 0.11 with impinging injector. CJ speed of the propellant is 2,408 m/s. The speed of the traveling waves are approximately 1,800 m/s (75% D_{CJ}).

detonation that quickly wraps around the annulus and collides with itself. This initial detonation is very near the Chapman-Jouguet speed of the mixture. As soon as the detonation reaches its own tail, the speeds of the traveling waves drop significantly. Several pulses of lower amplitude form. These quickly organize into three co-rotating waves that in short time transition to a final wave number of two.

2.6 Discussion

The presented experimental efforts have established the baseline operation in the 154-mm and 76-mm RDEs for gaseous methane and oxygen propellant. Consistent across all experiments is the axial choking of the combustors. There exists a regime in which the heat added to the flow is sufficient to thermally choke the constant-area annular ducts of the RDEs tested. For the 154-mm RDE, the point at which the combustor became decoupled from the downstream components was experimentally found by varying the imposed backpressure of the engine. With sufficiently low backpressures, the behavior

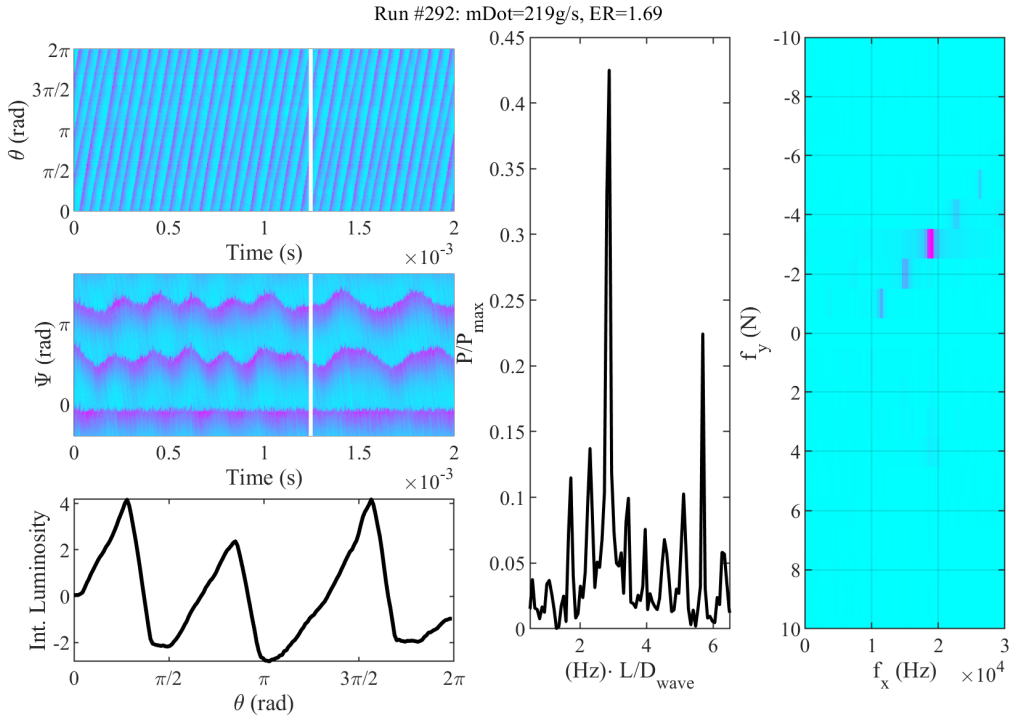

Figure 2.55: Run 292. AR = 0.11 with impinging injector. CJ speed of the propellant is 2,617 m/s. The speed of the traveling waves are approximately 1,415 m/s (54% D_{CJ}).

of the combustor is unaffected: the change of backpressure is not communicated to the engine. Conversely, as backpressure is raised, the point at which this imposition is felt is seen to move forward axially until the backpressure is felt throughout the combustor, including the front endwall. By identifying experiments that are backpressure sensitive or insensitive, the inlet Mach number is seen to become locked to a specific value of about $M_{inlet} = 0.26$ for low backpressures (with exit static pressures indicating sonic or near-sonic flow). Experiments that are backpressure insensitive are estimated to have low subsonic inlet Mach numbers (≈ 0.1 to 0.2) and decidedly subsonic exit conditions (≈ 0.6). Note that in for the 76-mm RDE, the range of mass fluxes tested precluded the ability to find a backpressure-sensitivity threshold: the engine appeared axially choked for the vast majority of experiments. The attainment of an axial choke point at the end of the combustor was also observed to drive the *system-wide* operating characteristics in the suite of testing with different injector-to-annulus area ratios. For the same mass flow rate and mixture equivalence ratio, should the combustor attain an axial choke point at the end of the combustor, the operating pressure of the combustor is necessarily constrained

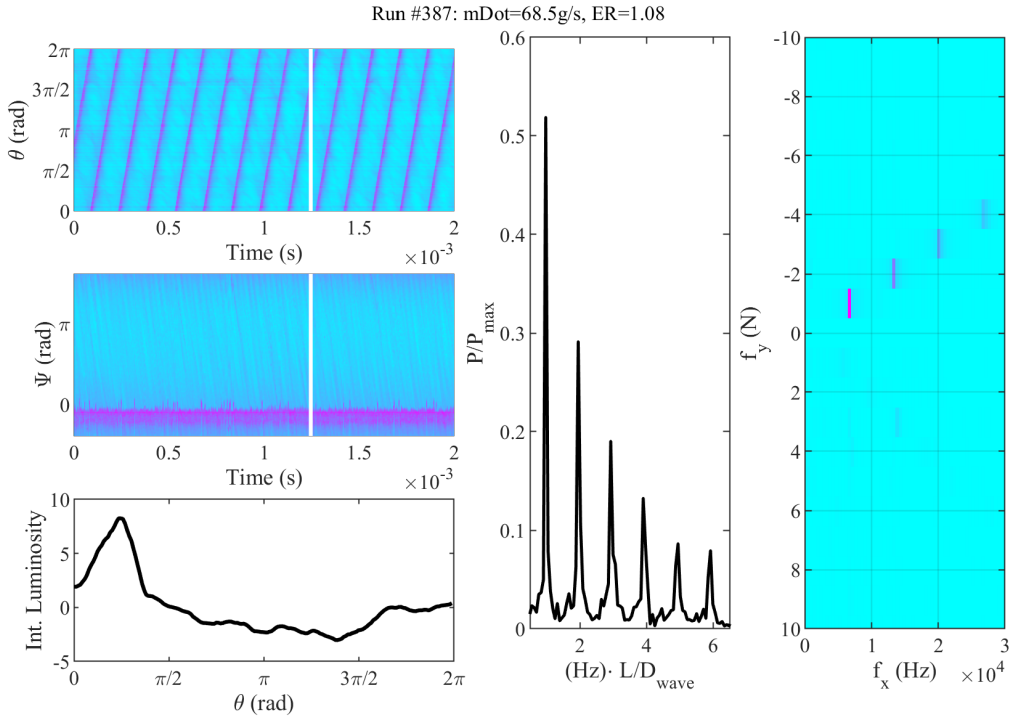

Figure 2.56: Run 385. AR = 0.11 with impinging injector. CJ speed of the propellant is 2,428 m/s. The speed of the traveling waves are approximately 1,541 m/s (64% D_{CJ}).

to a single pressure profile. This profile is independent of the injector-to-annulus area ratio. However, the degree of backpressurization of the plenums across the different area ratios varied significantly, from approximately a 15% backpressurization for $AR = 0.135$ to doubling the plenum pressures for $AR = 0.240$ to deliver the same mass flux. Furthermore, the differences in AR exhibited different traveling wave topologies, from regular propagation of co- and counter-rotating waves for $AR = 0.135$ to sporadic propagation of $AR = 0.188$, to single-wave propagation with visible parasitic deflagration for $AR = 0.240$. Although the radial injectors predominantly produced counter-rotating waves, there did exist some experiments with co-rotating waves, including a curious case of a single steep-fronted wave with an entrained shallow "deflagration bump." These cases occurred in the extremes of equivalence ratio. The impinging-type injector provided stronger detonations that rarely exhibited counter-rotation. Because the detonation waves of these experiments were 'cleaner' than the counter-propagating counterparts of the radial injectors, seen were some remarkable properties of the waves. These included strong mode-locking of the waves and persisting wave modulation of varying

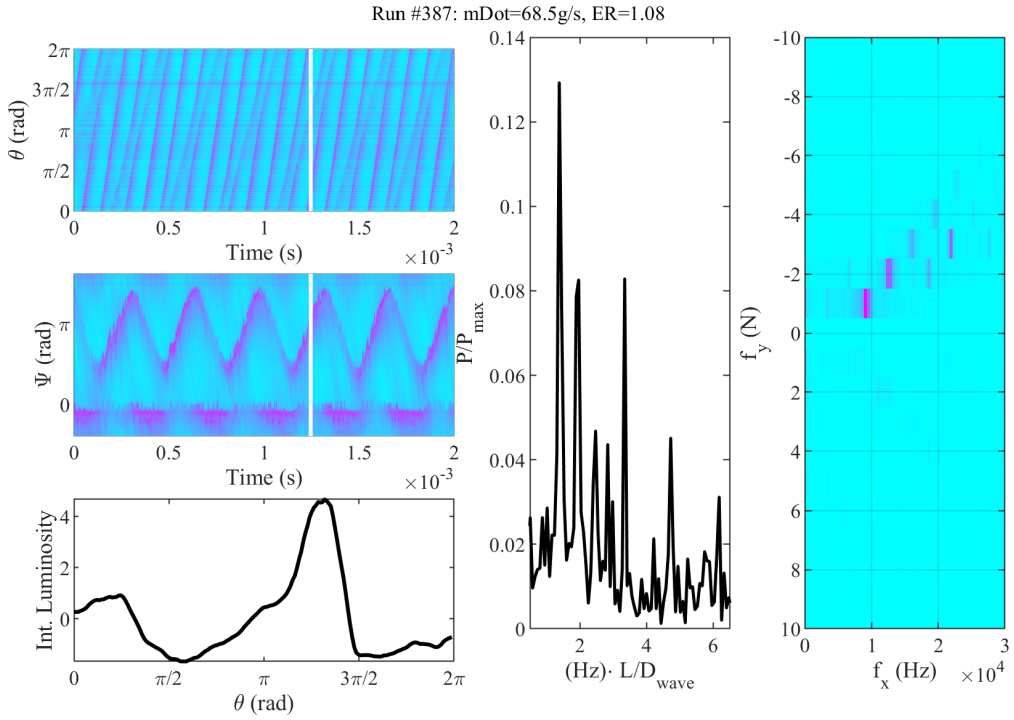

Figure 2.57: Run 385. AR = 0.11 with impinging injector. CJ speed of the propellant is 2,428 m/s. The speed of the traveling waves are approximately 1,440 m/s (59% D_{CJ}).

amplitude and frequency. Lastly, presented were representative periods of experiments that showcased transient periods of experiments, including ignition and transients leading to a change in the number of waves.

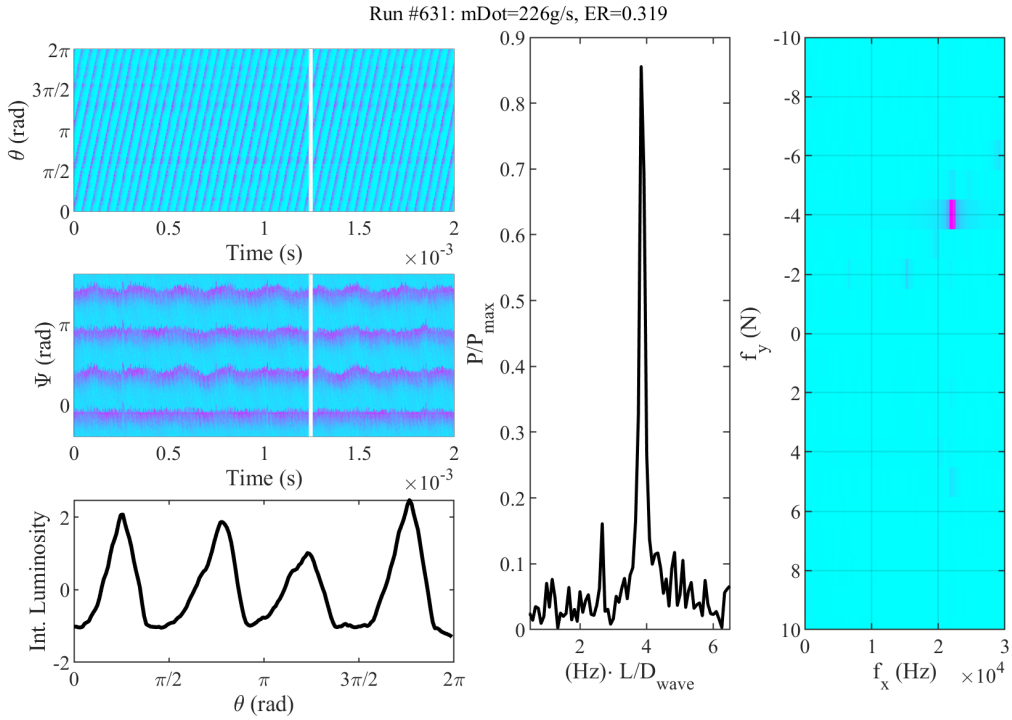

Figure 2.58: Run 631. AR = 0.11 with impinging injector. CJ speed of the propellant is 1,872 m/s. The speed of the traveling waves are approximately 1,250 m/s (67% D_{CJ}).

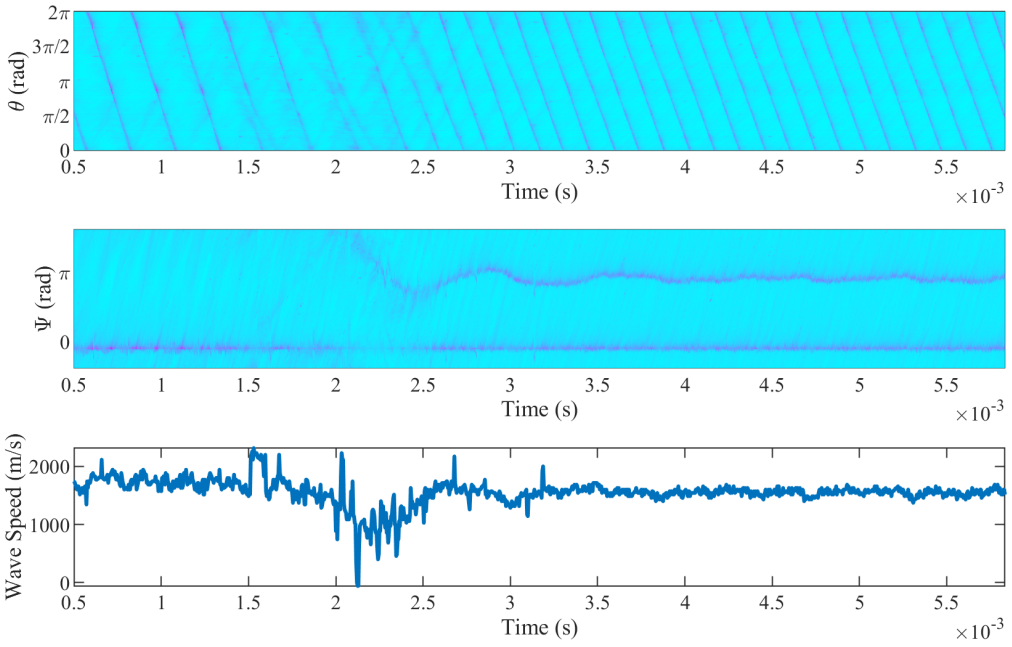

Figure 2.59: Wave nucleation process.

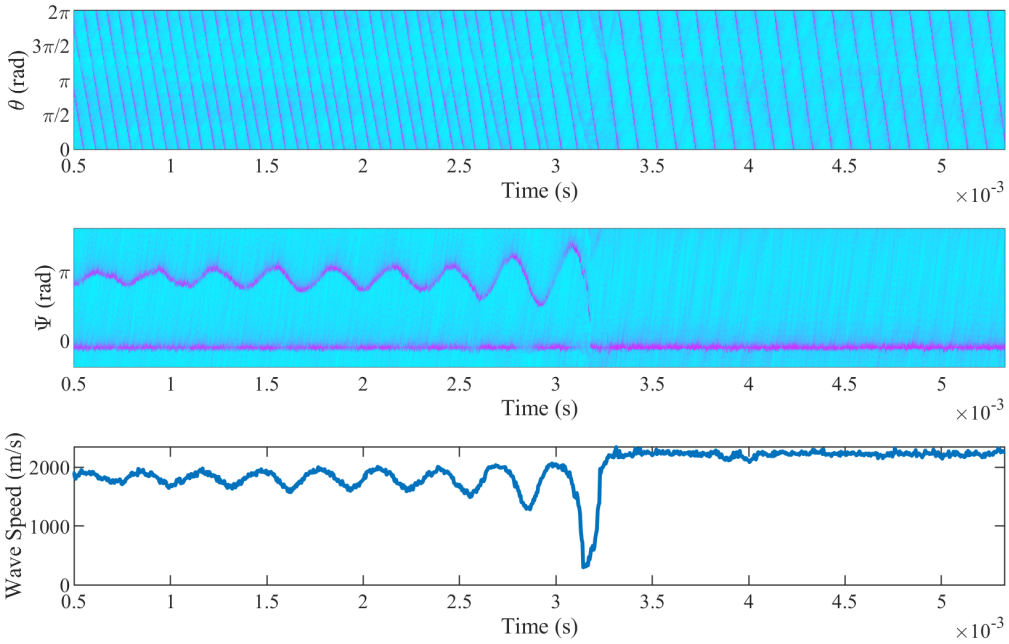

Figure 2.60: Wave nucleation process.

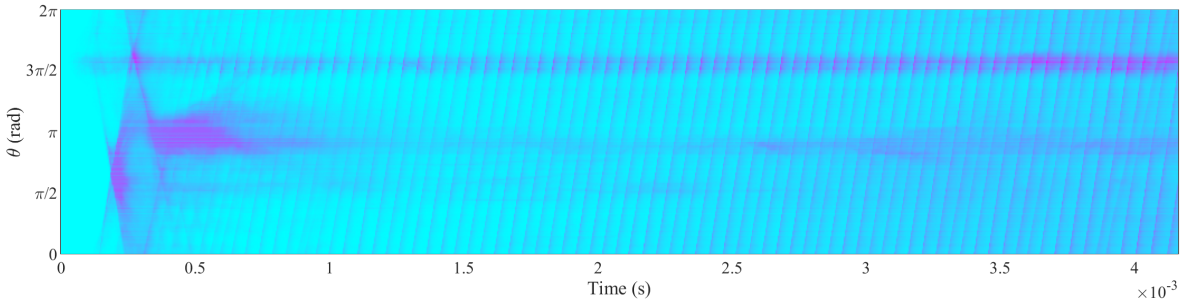

Figure 2.61: Ignition and wave formation process.

Chapter 3

Modeling

The behavior of rotating detonation waves seen in experiments shows striking structure and order, despite the nuances and peculiarities of the specific engines tested and flowfields developed. The formation of patterns and coherent structures is a fascinating branch of mathematical physics. In this chapter, a brief survey of relevant subsets of nonlinear waves and dynamical systems theories are presented within the context of the rotating detonation engine and pattern formation. Particularly, emphasis is placed on solitonic structures, systems for which there exists an energy input and output, and systems with excitable media. Topical examples are presented from these fields. Following this discussion, a similarly brief survey of nonlinear waves in combustion systems is presented, including the concept of detonation analogs.

Drawing upon these fields of nonlinear waves and dynamical systems, a mathematical analog to the rotating detonation engine is formulated from the starting point of the Majda's model for dynamic combustion [71]. Numerical experiments of the RDE analog are presented and compared to experimentally obtained kinematic traces of rotating detonation waves.

3.1 Nonlinear Waves and Dynamical Systems

The goals of this dissertation are to qualitatively reproduce (i) the detonation phenomenon in a periodic domain, (ii) the nonlinear dynamics of the collection of

rotating detonation waves seen in experiments, and to (iii) relate these phenomenon to the engineering tasks of maturing the RDE technology. In this chapter, the discussion begins with brief reviews of two branches of mathematical physics: nonlinear waves and dynamical systems. The latter topic is presented entirely within the context of nonlinear waves.

To motivate this discussion, consider the apparent *contradictions* of rotating detonation waves. First, in steady operation, the collection of waves travel about the annular combustion chamber at a constant speed with a constant wave shape. In some sense, this can be explicitly modeled with a linear wave equation advecting a particular wave shape (or, in the the case of multiple waves, a wave train) at a specified speed. Indeed, for the steady case, this *linear* representation is sufficient. However, known is that the unit physical processes governing wave behavior are decidedly nonlinear (combustion, mixing, injection, and exhaust, for example). Likewise, experimental observations tell a different story through *transients* - a set of phenomena that linear wave equations cannot capture. Thus, one may suppose that the steady operation of the RDE is the manifestation of the *saturation* of nonlinear phenomena such that the dynamics appear linear in some limit. For rotating detonation waves, this corresponds to an upper-bound on the growth of the waves: the detonations are supported by a finite amount of propellant, with which a certain heat release is associated, and therefore a maximum speed for which a detonation can be steadily supported. In other words, the growth of the detonation front is limited by the local exhaustion of propellant. Therefore, a model necessarily needs to incorporate both dynamics of a fluid medium and dynamics of the propellant and its regeneration.

Consider again the steady-state behavior of the collection of rotating detonation waves. The waves travel at identical speeds with phase differences between the waves that are symmetric and maximal, i.e., with phase differences of $2\pi/N$ where N is the number of waves in the chamber. Furthermore, the experiments of Chapter 2 show that perturbations exponentially decay to this stable state. Implied is that there is a significant degree of coupling between the waves. However, this contradicts classical detonation theory: the detonation front is *supersonic*, meaning the detonation structure is unaware of the upstream state. Likewise, the detonation is formed by the spawning of a sonic point behind the front of the wave, acoustically isolating the detonation from the

rest of the flowfield. Similarly, one can characterize the detonation waves as dispersive, since in long-time the waves are seen to separate to these maximum phase differences. This is a controversial statement in that the governing physics - reactive Navier-Stokes - is hyperbolic in nature, possessing no general dispersion relationship. This apparent contradiction needs to be resolved. Intuitively, because the detonations exist on a periodic domain, the flow ingested by a detonation is the output of the preceding wave modified by the physical processes occuring in-between the passage of the waves, such as injection, mixing, and exhaust. A model of the dynamics of the waves therefore additionally requires the inclusion of these effects.

3.1.1 Solitons

The study of nonlinear waves and coherent structures in fluids has a long history. Perhaps the best example is the observation of solitarily propagating waves by John Scott Russell and his follow-on experiments in a water tank in 1834 [72]. Russell, on horseback on the banks of the Union Canal in Scotland, followed a smooth, single-humped pulse of water emanating from a horse-drawn boat that had come to a stop in the water. He termed the pulse of water - which he followed for over a mile - as a "wave of translation," meaning that the form and velocity did not change over space or time.

After confirmation of the phenomenon in experiments and publication of his results, mathematical equations describing the behavior of the water waves were proposed by Boussinesq, Korteweg, and de Vries in the years following. The canonical equation is commonly termed the Korteweg-de Vries (KdV) equation and reads:

$$\frac{\partial u}{\partial t} + \frac{\partial^3 u}{\partial x^3} - 6u\frac{\partial u}{\partial x} = 0 \tag{3.1}$$

where u describes the height of the water surface over space (x) and time (t). A full derivation of the KdV equation and historical context of the problem is given in [72].

The KdV admits traveling wave solutions with remarkable properties. By transforming into the traveling wave coordinate $\xi = x - ct$, where c is the wave velocity, the KdV equation becomes an ordinary differential equation for which homoclinic (an orbit where the beginning and end states are identical) trajectories exist, subject to an effective

energy potential. This implies a family of solitarily propagating waves that can be recast as dynamics of a Hamiltonian system. Furthermore, the equation can be solved exactly.

The solitarily-propagating waves of the KdV equation, or solitons, are local structures where the nonlinearity exactly balances the dispersive properties of the equation. Thus, the steady behavior of solitons of the KdV equation can be fully characterized by specifying an initial soliton shape (effectively specifying the energy content to be governed by the Hamiltonian of the system). The speed of the solitons are directly related to their amplitude. However, the interactions of these waves are decidedly nonlinear. Hallmarks of solitonic interactions include (i) particle-like behavior pre- and post- interaction, (ii) nonlinear superposition at the collision point, and (iii) phase shifts of the wave trajectories after interacting. In Fig. 3.1, two interacting KdV solitons are shown. The higher-amplitude wave travels faster than its lower-amplitude counterpart. Because the solitons are fundamentally localized structures, as they approach one another, the balance physics of the interaction is dissimilar from that of steady propagation. The waves pass through each other, but with a phase shift imposed on the waves during this nonlinear interaction. After the interaction, the solitons return to their initial waveforms and speeds. The fundamental properties of the KdV soliton interactions generalize to those of other nonlinear wave equations, including the Boussinesq Equation, the Nonlinear Shrödinger Equation, and the sine-Gordon Equation.

Note that the behavior of rotating detonation waves are similar to KdV solitons: higher amplitude waves travel faster, and in the limit of steady behavior, the wave propagation appears linear. However an important distinction between the two should be made: the KdV equation is dispersive (or, possesses a non-trivial dispersion relationship), where rotating detonation waves are fundamentally of a hyperbolic system.

3.1.2 Driven-dissipative Systems

Although the solitons of storied equations such as KdV and NLS give significant physical insight into the propagation of rotating detonation waves, the comparison is weak in that these canonical systems are conservative. In fact, the KdV equation can be shown to satisfy an infinite number of conservation laws [73]. Self-organization is not restricted to these special systems. Systems possessing an input/output energy balance are prevalent

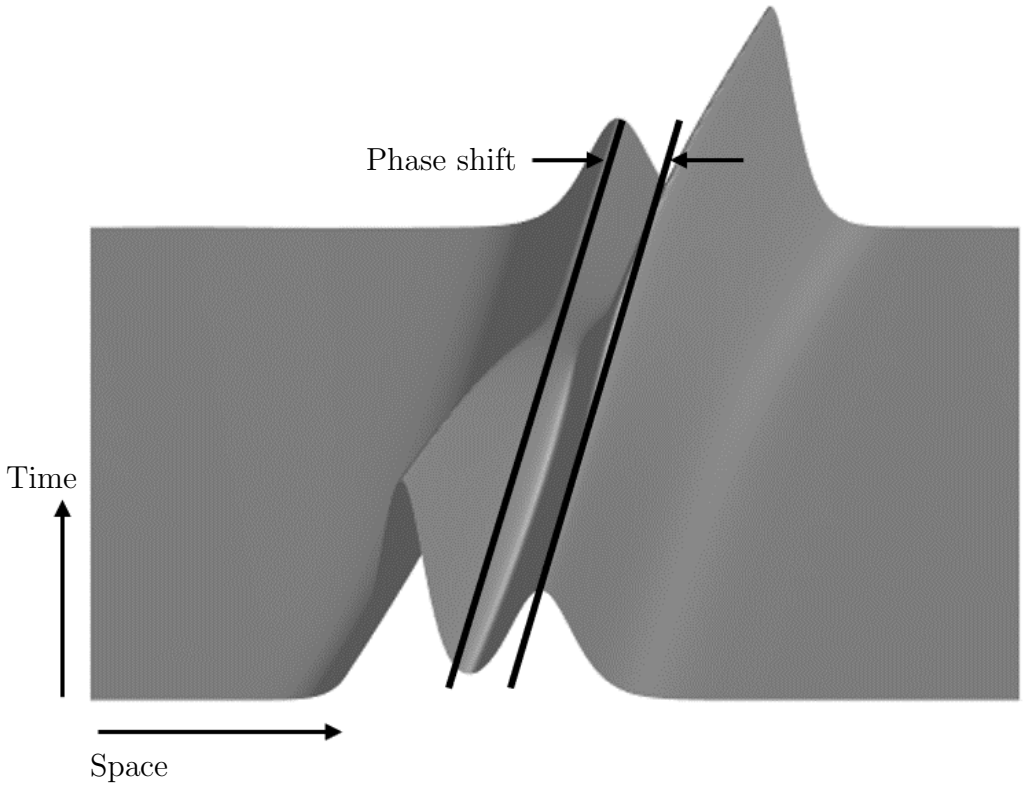

Figure 3.1: Two KdV solitons nonlinearly interacting. The local balance physics at the point of interaction gives a fundamentally different structure than for the freely-propagating soliton. This different physics is manifest as a phase shift in the soliton trajectory. Their interaction is not the linear superposition of the waves, despite having linear trajectories pre- and post- interaction.

in a diverse set of subjects, including biology, optics, chemistry, and fluids [74].

In driven-dissipative systems, the balance of gain and loss, together with the constraints of nonlinearity and dispersion of the underlying system, is responsible for the formation of local structures and their behavior. At the highest level, rotating detonation waves can be classified into this category: under the conditions of the nonlinearity of the fluid medium, the energy input (propellant injection) and output (exhaust and energy rejection processes) are what gives rise to the formation of stably propagating detonation waves. This is the context in which a model will be built in Section 3.2.

Here, presented are examples of driven-dissipative systems with behavior similar to

that of the RDE. First is the FitzHugh-Nagumo model for nerve excitation in a continuous medium. Highlighted in this system are the ideas of *triggering*, *excitation*, and *refractoriness*. Second is the passively mode-locked laser, whose periodic domain and gain and loss dynamics give bifurcation structures similar to those of the RDE.

Integrate-and-Fire Models of Spiking Neurons

In a field of neurons that possess some neuron-to-neuron coupling, individual neurons act upon a stimulus provided by coupling by "spiking" and sending this stimulus to neighboring neurons. These dynamics are driven by neuron cell membrane voltage potentials [75]. A popular model of the neuron spike is the *integrate and fire* model, whereby a neuron accumulates some external input until a threshold is reached [76, 77]. Upon reaching the membrane potential threshold, the neuron undergoes a rapid change of state where the neuron develops a spike and resets to some base value of membrane potential.

The neuron is *driven* by an external input and *dissipates* the accumulation of energy through the generation of a spike. The FitzHugh-Nagumo (FHN) model is one such integrate and fire model, a simplified version of which is given as:

$$\frac{dv}{dt} = -kv + \alpha + cmv + mI \tag{3.2}$$

$$\frac{dm}{dt} = -m + \Theta\left(m - v\right) \tag{3.3}$$

where v is the subthreshold potential of the cell membrane, m is a variable switching between a refractory state and a depolarization state, I is the external input, and k, α, and c are constants reflecting the rates of charging and discharging of m and v. Numerical simulation of this model is shown in Fig. 3.2 for a single neuron with model constants $k = 0.015$, $a = -0.035$, $c = 0.002$, and $I = 0.05$.

This charge-discharge model, while simplistic, captures many of the essential elements of the neuron. Neurons exhibit periods of "refractoriness" after spiking, inhibiting the formation of a second spike in rapid succession. Implied is that there is a minimum amount of time required between spikes. Similarly, there exists significantly different

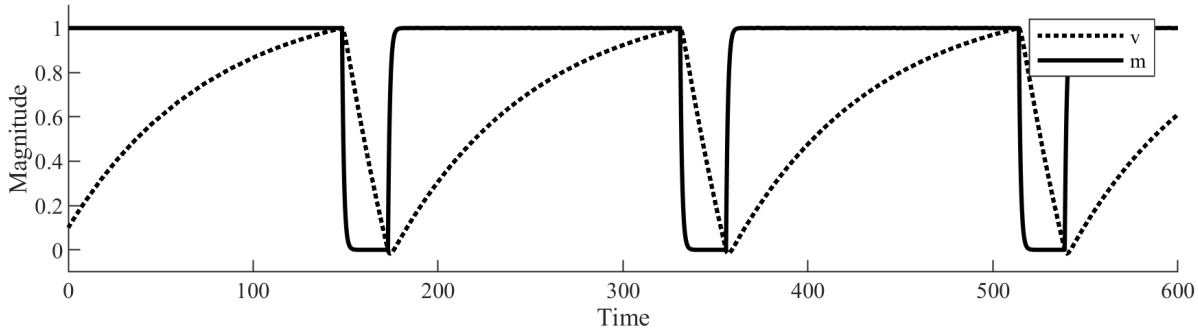

Figure 3.2: Simulation of an integrate-and-fire model for a single neuron. The cell menbrane subthreshold voltage is given by v and the state of the cell is given by m, where $m = 1$ is the depolarization period and $m = 0$ is the refractory period. Model constants: $k = 0.015$, $a = -0.035$, $c = 0.002$, and $I = 0.05$.

time scales between the two states of the cell: the "charging" takes place on the order of five to ten times longer than to discharge.

Extensions of the FHN exist to model a continuum of neurons. In this setting, the medium is termed *excitable* - or able to release energy upon *triggering* on a sufficient external stimulus. In the continuous domain, the FHN model takes on the form of a reaction-diffusion equation that has its own set of remarkable properties, including traveling pulse trains and pulse modulation [11]. An example of a two-wave pulse train is shown in Fig. 3.3. Of note in this figure are the inter-pulse spaces - they exhibit the same modulation of phase difference as seen in Chapter 2.

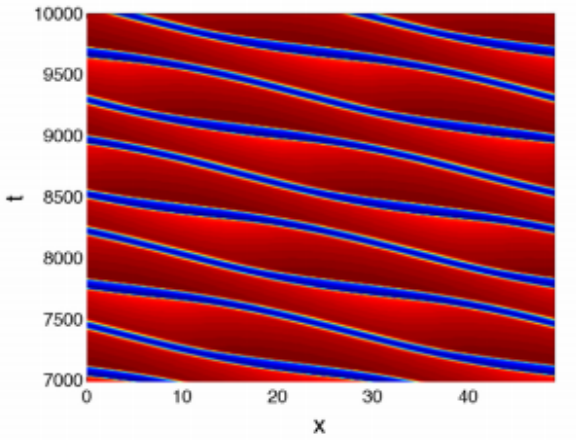

Figure 3.3: Traveling waves of a continuum-modified reaction diffusion equation the modeling of nerve pulses. For certain parameter regimes, the collection of waves can form a modulational instability. Reproduced from [11].

The features of integrate-and-fire models that are desirable in modeling rotating detonation waves are the ideas of *triggering*, *excitability*, and *refractoriness*. In the RDE and in integrate-and-fire models, the medium through which the waves travel possess some implicit energy content that *can* be released should the medium become triggered. In the case of integrate-and-fire models, triggering is analogous to crossing the subthreshold potential required to spike. In the RDE, combustion is shock-initiated. Both systems also possess some inherit time delay before another traveling wave or spike can be formed. In the RDE, this time lag is because of the lack of re-introduced propellant into the combustion chamber. In the integrate-and-fire model, this is because of the resetting of the potential to a low value, from which the accumulation of an external input is required before spiking again.

Mode-locking and Bifurcations in Laser Systems

The electromagnetic field in an optical fiber laser cavity is described by the nonlinear Schrödinger equation (NLS) - a slowly-varying envelope field approximation that relates the dominant balance physics of wave dispersion and nonlinearity [78]. The NLS equation admits soliton solutions, or waveforms where nonlinearity and dispersive phenomena exactly balance, allowing for stable and steady wave propagation. In ring fiber lasers (Fig. 3.4), these soliton pulses are subject to localized *gain* and *loss*, as imposed on the system by an external energy feed source (pump) and energy sink (an output coupler and saturable absorber, for example).

In such laser configurations, the time scales of gain absorption can be significantly different than that of the gain recovery. The implication is that an *intensity discrimination* exists: the pulses in the cavity experience pulse-shaping phase shifts biased towards higher-intensity gain due to a saturable absorption mechanism [78]. In this manner, should multiple pulses exist in the system, the pulses establish a communication link via the gain and loss mechanisms. The pulses become mode-locked in that they experience phase shifts (once per round trip through the ring fiber) that adjust the inter-pulse spacing such that through time, the pulses experience equivalent amounts of gain.

Should the gain in the system be increased, the local balance of nonlinearity and

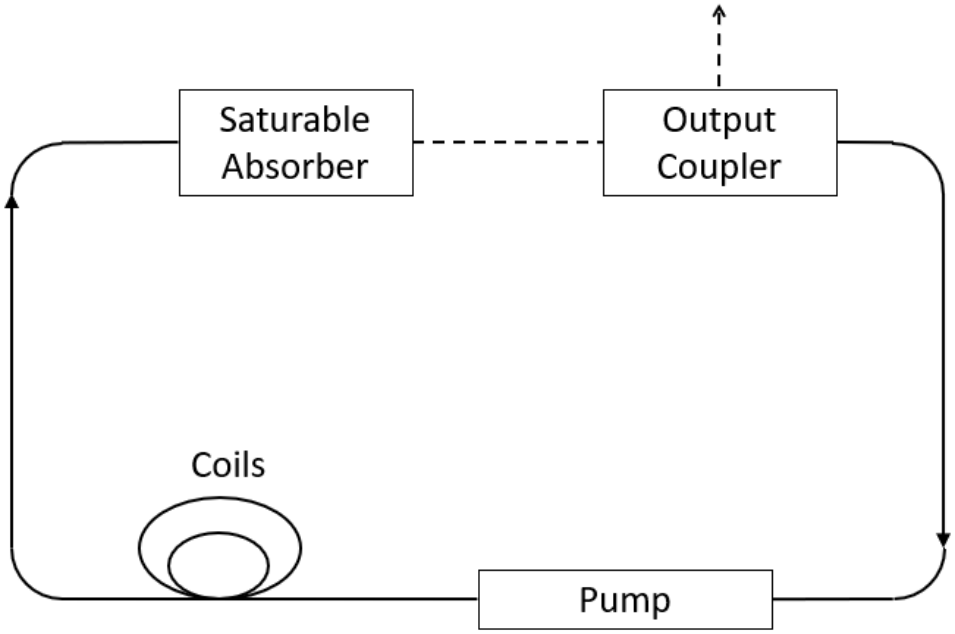

Figure 3.4: Ring fiber laser configuration with localized gain (pump) and loss (output coupler where a fraction of the energy is directed out of the system). The collection of soliton pulses within the cavity are formed by the intensity discrimination (nonlinear loss) provided by the saturable absorber. The solitons seek maximal and symmetric phase differences between one another in an analogous process to that of rotating detonation waves.

dispersion no longer holds and the soliton is destabilized. Specifically, as a soliton pulse is subject to increasing gain, its spectral width grows beyond the gain bandwidth and becomes unstable. After a point of criticality, the pulse will destabilize and split into two separate pulses of lower amplitude and smaller bandwidth. These pulses become mode-locked through the same phase-shifting processes.

The balance between gain, losses, dispersion, and nonlinearity in the fiber ring laser system dictate the quasi-steady behavior of the pulses and the inter-pulse dynamics, including bifurcations. With the inclusion of gain, loss, and saturation effects, the number of pulses in the laser cavity exhibit a "staircase" or "ratcheting" bifurcation structure (an example of which is shown in Fig. 3.5) [79, 12]. Furthermore, for differently engineered saturation and loss behavior, the dynamics of the solitons in the laser cavity have been shown to exhibit period-doubling bifurcations and chaos [12] - this is shown in Fig. 3.6. These bifurcation diagrams are similar to those of the RDE [80].

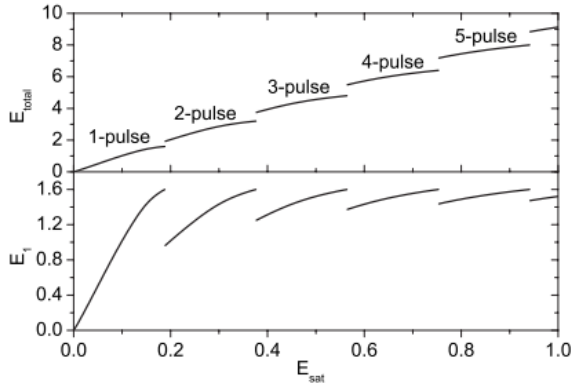

Figure 3.5: Subject to global gain/loss dynamics and saturation, the number of pulses in a ring-laser cavity follows a "ratcheting" bifurcation structure similar to that of the RDE. Reproduced from [12]

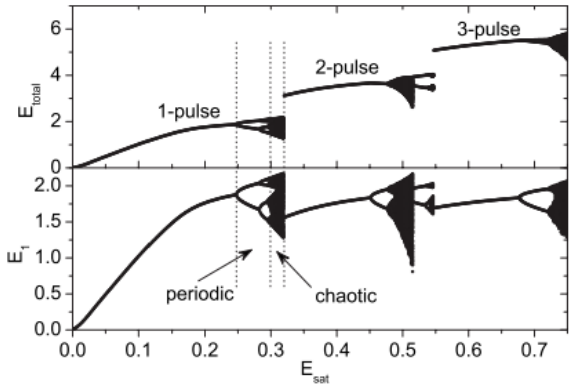

Figure 3.6: The inter-pulse regions of the bifurcation diagram of the laser cavity with nonlinear gain and loss shows period-doubling and eventual chaotic propagation. Reproduced from [12].

3.1.3 Reaction Waves

Waves in chemically activated systems can take on many forms, including reaction-diffusion fronts, combustion instabilities (as mentioned in Chapter 1), detonations, and autoignition phenomena. Here, combustion waves are discussed in the context of the *solitarily propagating wave* with gain (heat release through combustion) and loss (energy rejection to some ambient condition) - these are autowave processes.

The simplest example of a combustion autowave is a wildfire. If an ignition kernel (a match or a campfire, for example) surpasses a the energy required to trigger the excitable medium (the campfire becomes too large), the medium locally releases heat that drives

the flame front forward through the medium at the velocity of the diffusive interface. In this example, after the passage of the reaction front, the fuel is spent and the time scale of regeneration of vegatation (more fuel) is orders of magnitude larger (years) than the time scale of the reaction front (minutes to days). This concept of divergent time scales is a recurring theme in combustion autowaves.

The auto-ignition model of the Soviet engineer Frank-Kamenetskii [81] and of flow reactors by Zel'dovich [82] are two such models to display the interesting interplay between different temporal scales of reaction and of energy loss and regeneration. The system studied by Frank-Kamenetskii was the oxidation of a reactive gas flowing over a hot, catalytic surface. The system exhibits bi-stability: should the heat transfer away from the medium be greater in magnitude than the heat input due to reactions, the system is not excited and regresses to a 'cold flow' situation. Should the opposite occur (reactions dominate), the dynamics of the system are such that periodic ignition followed by extinction (as the time scale for combustion is much shorter than that of the reintroduction of reactant) develops. The mathematical system [13] reads:

$$\frac{da}{dt} = \beta(a_0 - a) - ake^{-\epsilon/T} \tag{3.4}$$

$$\frac{dT}{dt} = \frac{Q}{c}ake^{-\epsilon/T} - \alpha(T - T_0) \tag{3.5}$$

where a is the concentration of reactant, T is the surface temperature of the catalyst, Q is the heat release associated with the fluid, c is the specific heat, and α and β, are constants specifying rates of heat and mass transfer. The dynamics of the system are therefore the result of the competition between the rates of combustion, heat transfer, and regeneration of reactant. Note that this system is a coupled ordinary differential equation describing the dynamics at a single point in space. Supposing a similar structure exists for reaction-diffusion type equations, for example, in a flow reactor [82], traveling solitary combustion waves can be seen for certain parameter regimes [13]. Example profiles of such 'flamons' are shown in Fig. 3.7. The tails of each of the example profiles is determined by the rate at which the front moves as well as the rate of energy transfer away from the wave.

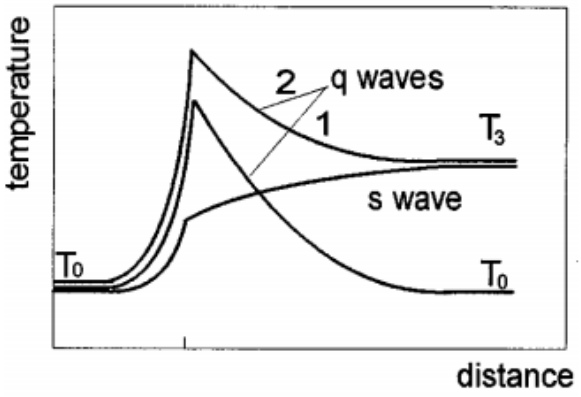

Figure 3.7: Example profiles of *flamons* in a flow reactor subject to energy input/output balances. Reproduced from [13].

In the limit of the extremes of the propagation of the flamons of Fig. 3.7, the transverse waves (perpendicular to the direction of travel) associated with hydrodynamic instabilities of the front may become excited. In this scenario, spinning and cellular fronts can occur, as in the Belousov-Zhabotinskii reaction (reaction-diffusion - see Fig. 3.8) and in spinning detonation.

Lastly, within the context of combustion instabilities, the spinning reaction waves corresponding to the first tangential mode of rocket combustors has been noted to exhibit solitonic propagation. In a study of high-frequency tangential instabilities in rocket combustors, Litchford [83] concludes that the reaction waves seen in experiments and his own computational modeling are indeed solitonic in nature. The observed structures were nonperiodic, self-sustaining, and collisionally stable, meaning that the reaction waves behaved like particles pre- and post-interaction, again with a phase shift similar to that of KdV interactions. In his study, however, these traveling waves are not detonations (not steep-fronted), though he notes that experiments claiming "detonation-like processes" in rocket combustion chambers may indeed exist in the limits of extreme behavior of the mechanisms similar to those included in his study. Of particular interest is the inclusion of a "transpirational" boundary condition that replenishes reactant after the passage of a wave.

Figure 3.8: The Belousov-Zhabotinskii reaction producing spiral waves [14, 15]. Reproduced from [15].

3.1.4 Detonation Analogs

Detonation analogs are *invented*, ad hoc mathematical models [84] proposed to mimic the physical phenomena observed in real detonations. Historically, two very similar models were proposed around 1980 with the goal of qualitatively describing detonation dynamics, including "galloping" detonation. These were the Fickett [85] and Majda [71] detonation analogs. The original intent of the model was to evaluate the traveling detonation wave-like solutions of the models and their stability, as these simplified models are more tractable and mathematically manageable than the reactive-Euler counterpart.

The two models are fundamentally the Burgers' Equation modified for a chemical source term. How the two models differ is in their treatment of the kinetics and their equation of state. In the Majda detonation analog, the source term is dependent solely on the time dynamics of a combustion progress variable, as in the reactive Euler equations. The Fickett analog, however, links combustion to the evolution of the fluid medium through the spatial derivative of the combustion progress variable. In doing so, the combustion source term can develop a very rich set of behavior, including the fluctuation of induction lengths and decoupling of the leading shock from the combustion zone (in which case,

the detonation fails to propagate). The Fickett analog is given by:

$$\frac{\partial u}{\partial t} + u\frac{\partial u}{\partial x} = -q\frac{\partial \lambda}{\partial x} \tag{3.6}$$

$$\frac{\partial \lambda}{\partial t} = \omega(u, \lambda) \tag{3.7}$$

$$p = \frac{1}{2}\left(u^2 + \lambda q\right) \tag{3.8}$$

where $u(x,t)$ is the state of the medium in space and time, q is the heat release associated with the unreacted medium, and λ is a combustion progress variable (exists within $[0,1]$). The dynamics of the combustion progress variable are governed by a model for chimical kinetics, $\omega(u,\lambda)$ - typically Arrhenius in type. Similarly, the Majda analog is given by:

$$\frac{\partial u}{\partial t} + u\frac{\partial u}{\partial x} = q\frac{\partial \lambda}{\partial t} \tag{3.9}$$

$$\frac{\partial \lambda}{\partial t} = \omega(u, \lambda) \tag{3.10}$$

$$p = \frac{1}{2}u^2 \tag{3.11}$$

In both models, the variable representing the state of the fluid medium, u, is related to the properties of a real fluid only by analogy: u assumes some properties of density, temperature, internal energy, and velocity, though explicit relationships do not exist.

Because of the difference in the implementation of the chemical source term, and therefore the associated equation of state of relating u to an effective pressure, these two analogs exhibit different properties. While both recover the ZND profile for detonations for Arrhenius-type kinetic models, only the Fickett model recovers frontal dynamics similar to those of real detonations [84, 16]. Example time-histories of these dynamics are shown in Fig. 3.9. Furthermore, the model recovers the period-doubling bifurcations to chaos (Fig. 3.10) characteristic of 1-dimensional galloping detonations.

Without modification to the specific form of Arrhenius kinetics to allow for variations in induction lengths, and therefore combustion-shock decoupling, the Majda detonation analog does not admit limit cycle solutions [86, 87, 88]. Nevertheless, Majda's model

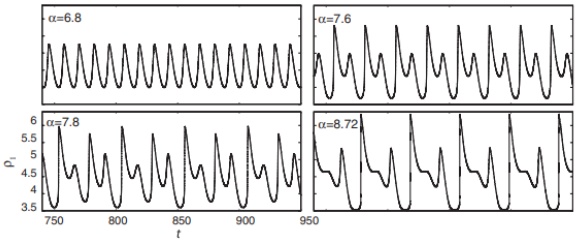

Figure 3.9: The time history of leading shock pressures for Fickett's detonation analog for different activation energies in the Arrhenius kinetic model. Reproduced from [16].

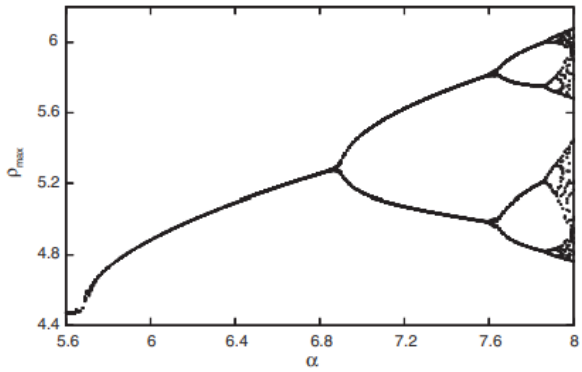

Figure 3.10: Period doubling bifurcations to chaos in the Fickett detonation analog. Reproduced from [16].

remains attractive for its ease of implementation and recovery of the ZND detonation front structure. Modern efforts of detonation analog modeling include derivations from first-principles through asymptotics and the investigation of shock-chemistry interaction (see Faria and Kasimov [33, 89]).

3.2 The RDE Analog System

The requirements for a successful model are thus:

- Recover linear trajectories of the waves outside of wave-to-wave interactions,
- Demonstrate a "refractory" period due to the depletion of propellant immediately behind the waves and the slow time scales of injection and mixing,
- Exhibit mode-locking of the collection of waves with sufficient time,
- Possess an excitable medium where heat release is governed by some version of

Arrhenius kinetics, and

- Assume a distinct "ratcheting" bifurcation structure when energy input into the domain is taken to be a bifurcation parameter.

To begin, a derivation approach is adopted from Mi and Higgins [90] with the key difference being the inclusion of a second dimension, as depicted in the control volume in Fig. 3.11. The aim is to capture the dynamics of an intensive property, here taken to be internal energy (denoted u), through time. The time rate of change of u in the control volume is equal to the difference in fluxes into and out of the volume. Additionally, a source term mimicking chemical heat release adding energy within the domain. Mathematically:

$$\begin{aligned} \dot{E}_{cv} = \Delta x \Delta y \left[q\dot{\lambda} \right] \\ +\Delta y \left[f\left(\eta_x\right) - f\left(\eta_{x+\Delta x}\right) \right] \\ +\Delta x \left[f\left(\eta_y\right) - f\left(\eta_{y+\Delta y}\right) \right], \end{aligned} \tag{3.12}$$

where x and y are coordinates in the circumferential (periodic) and axial directions, respectively, q is the propellant specific heat release, λ is a combustion progress variable, and $f(u)$ is the flux of u across a boundary. The property u is defined to be the specific internal energy $\frac{E}{\Delta x \Delta y}$.

Dividing by the dimensions of the control volume, one arrives at:

$$\dot{E}_{cv} = q\dot{\lambda} + \frac{f\left(u_x\right) - f\left(u_{x+\Delta x}\right)}{\Delta x} + \frac{f\left(u_y\right) - f\left(u_{y+\Delta y}\right)}{\Delta y}. \tag{3.13}$$

As in Majda's original paper [71] and in Mi and Higgins' derivation [90], chosen is the simplest flux that satisfies the convexity required for the Lax entropy condition; i.e., that $f(u) = \frac{1}{2}u^2$. Taking the limits as $\Delta x \to 0$ and $\Delta y \to 0$ and moving the spatial terms to the left hand side yields:

$$\frac{\partial u}{\partial t} + \frac{\partial \frac{1}{2}u^2}{\partial x} + \frac{\partial \frac{1}{2}u^2}{\partial y} = q\frac{\partial \lambda}{\partial t}. \tag{3.14}$$

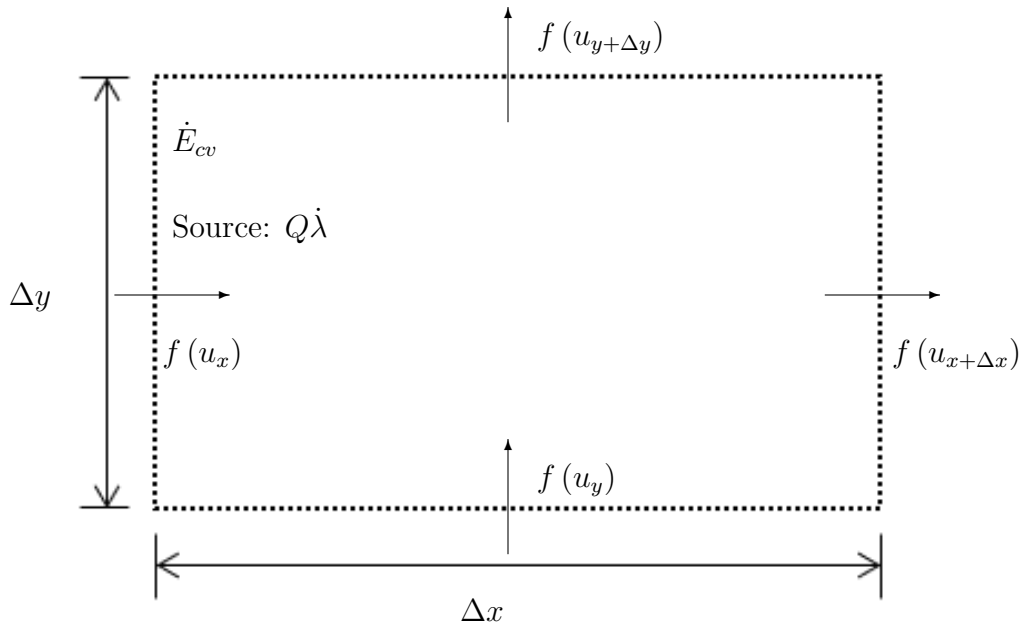

Figure 3.11: 2-D control volume for model derivation.

3.2.1 Quadratic Losses

Because of the restriction of the domain to the periodic 1-D line in the x co-ordinate, the axial (y) gradient will be modeled. The control volume is chosen to exist adjacent or attached to the front endwall of a RDE. At this front endwall, the flux of η entering the domain is assumed to have a negligible effect on the evolution of energy in the domain when compared to the circumferential flux terms and source term. As such, $f\left(\eta_y\right) = f\left(\eta_{y=0}\right) \approx 0$, so the approximation of the gradient becomes:

$$\frac{\partial \frac{1}{2}u^2}{\partial y} \approx \lim_{\Delta y \to 0} \frac{\frac{1}{2}u^2_{y+\Delta y} - 0}{\Delta y}. \tag{3.15}$$

To simplify further, assume that the detonation waves in real engines are approximately planar and the properties immediately before and after the passage of a wave are approximately uniform. Therefore, one can assume that from the axial location $y = 0$ (attached to the front end wall of the engine) to $y = y_c$ (where y_c is the height of the detonation wave) the properties are uniform. Exploiting this approximate uniformity, the limit of Eq. (3.15) is taken to $\Delta y \to y_c$ (instead of zero). Any further reduction in the value of Δy will, in effect, over-predict the magnitude of the gradient. This simplified

limit now takes on a polynomial form:

$$\lim_{\Delta y \to 0} \frac{\frac{1}{2}u_{y+\Delta y}^2}{\Delta y} \approx \lim_{\Delta y \to y_c} \frac{\frac{1}{2}u^2}{\Delta y} = \epsilon_0 \frac{1}{2} u^2 = \epsilon u^2, \tag{3.16}$$

where $\epsilon = \frac{1}{2}\epsilon_0$ are constants reflecting the severity of the axial gradient of flux through the engine. Note that the flux function $f(u) = \frac{1}{2}u^2$ acts as an equation of state relating the property η to another whose gradient drives flow - this derived property $\frac{1}{2}u^2$ is analogous to pressure in the momentum equation for fluid flows. In real engines whose axial flow is thermally choked (the Mach number at the exit of the engine is 1), the axial pressure gradient near the front wall of the RDE is proportional to pressure at that location; i.e. $\frac{\partial p}{\partial y}|_{y=0} = cp_{y=0}$, where c is some parameter intrinsic to the engine (see Chapter 2). The proposed functional form of the axial gradient in Eq. (3.16) enforces the same behavior.

The equation governing the evolution of energy in the circumferential domain is now given as:

$$\frac{\partial u}{\partial t} + u\frac{\partial u}{\partial x} = q\frac{\partial \lambda}{\partial t} - \epsilon u^2. \tag{3.17}$$

This is equivalent to the inviscid Burgers' Equation with a chemical reaction source term and loss of energy to an ambient condition. The physical mechanism for the loss is the lateral relief from lack of confinement on one side of the traveling waves. Regularization with a viscous term ($\nu\frac{\partial^2 u}{\partial x^2}$) completes the comparison to the classic Burgers' equation, though for this section of this study, viscous effects are excluded.

The formulation of Eq. 3.17 is insufficient - still needed are descriptions of the combustion and injection processes. In the absence of combustion, expected is that $\lambda = 0$, or similarly in the absence of any propellant regeneration, $\lambda = 1$. Thus, the dynamics of the combustion progress variable should be the competition of a combustion term and a regeneration term:

$$\frac{\partial \lambda}{\partial t} = \omega\left(u, \lambda\right) - \beta\left(u, \lambda\right). \tag{3.18}$$

Equation 3.17 is now modified to reflect the splitting of the source term by only including

the effects of heat release, not regeneration:

$$\frac{\partial u}{\partial t} + u\frac{\partial u}{\partial x} = q\omega\left(u, \lambda\right) - \epsilon u^2. \tag{3.19}$$

3.2.2 Gain Depletion

The rate of combustion to be constrained to be a function of the state of the domain. For this formulation, the heat release function $\omega(u, \lambda)$ is dictated by a simplified version of Arrhenius kinetics with a explicitly defined 'ignition energy' u_c, activation energy α, and pre-exponential factor k:

$$\omega\left(\eta\right) = ke^{\left(\frac{\eta - \eta_c}{\alpha}\right)}. \tag{3.20}$$

For a steadily traveling detonation wave, the expectation is that this gain term dominates the dynamics, providing a rapid release of energy into the domain saturable only by exhaustion of fuel or another nonlinear effect (such as a nonlinear loss term).

3.2.3 Gain Recovery

The gain recovery term $\beta\left(u, \lambda\right)$ works against gain depletion to 'refill' the domain towards a $\lambda = 0$ state. In injection of gaseous propellant, injectors are typically 'choked' orifices, meaning that perturbations in the combustor cannot influence the injection process as no characteristics can travel upstream past the choke point. However, in the presence of large-amplitude pressure oscillations (such as those present in detonation engines), the peak pressures may be comparable to those of the propellant plenums. This implies a loss of the sonic condition of the injectors. Should this occur, the state of the combustor becomes coupled to the injection scheme and can lead to unsteady behavior. To include these phenomena into the model, an activation function-based injection term is used that responds to the periodic forcing by the rotating detonation waves. The proposed activation function is given by:

$$\beta\left(u, \lambda\right) = \frac{su_p\lambda}{1 + e^{r(u - u_p)}}, \tag{3.21}$$

Table 3.1: Simulation survey parameters.

L	q_0	α	u_c	u_0	u_p	k	ϵ	r	D_{CJ}
2π	1.0	0.3	1.1	0	0.5	1	0.11	5	2

where su_p is the time constant for the regeneration of λ. In real engines, s is influenced by the injection scheme, mixing effectiveness, and total injection area. The quantity u_p corresponds to injection pressure. This form asymptotically assumes the value of the numerator if the value of u is small compared to u_p. In the limit as u becomes much larger than u_p, $\beta(u)$ approaches zero. Similarly, if either s or u_p is zero, there is no regeneration of λ. In this manner, the parameter u_p is used to control the injection sensitivity threshold. r is a parameter adjusting the 'steepness' of the activation function. Increasing injection area (s), plenum pressure (u_p), or both increases the energy flux into the domain. However, the dynamic response to these increases differs significantly. In real engines, in the case of a high plenum pressure (a 'stiff' injector), the influence of the detonation pressure becomes insignificant and the injector can deliver a consistent supply of propellant. In the case of a large injection area (holding the plenum pressure constant), the injectors are susceptible to large fluctuations of mass flux in response to this periodic forcing. Example activation function-based injector models are shown in Fig. 3.12. With this formulation, mixing is exponential with time - in the absence of combustion, λ asymptotically approaches 0.

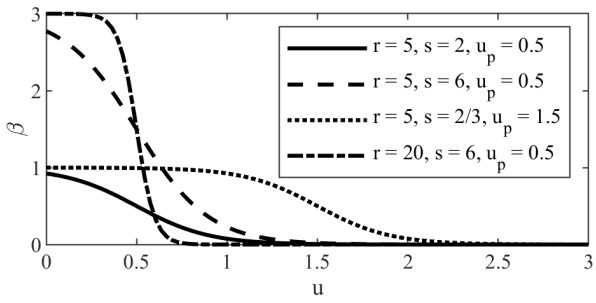

Figure 3.12: The influence of the state of the domain, u, on the gain recovery function β following the functional form of Eq. (3.21). The solid line is the activation function used for simulations in Section 3.3.

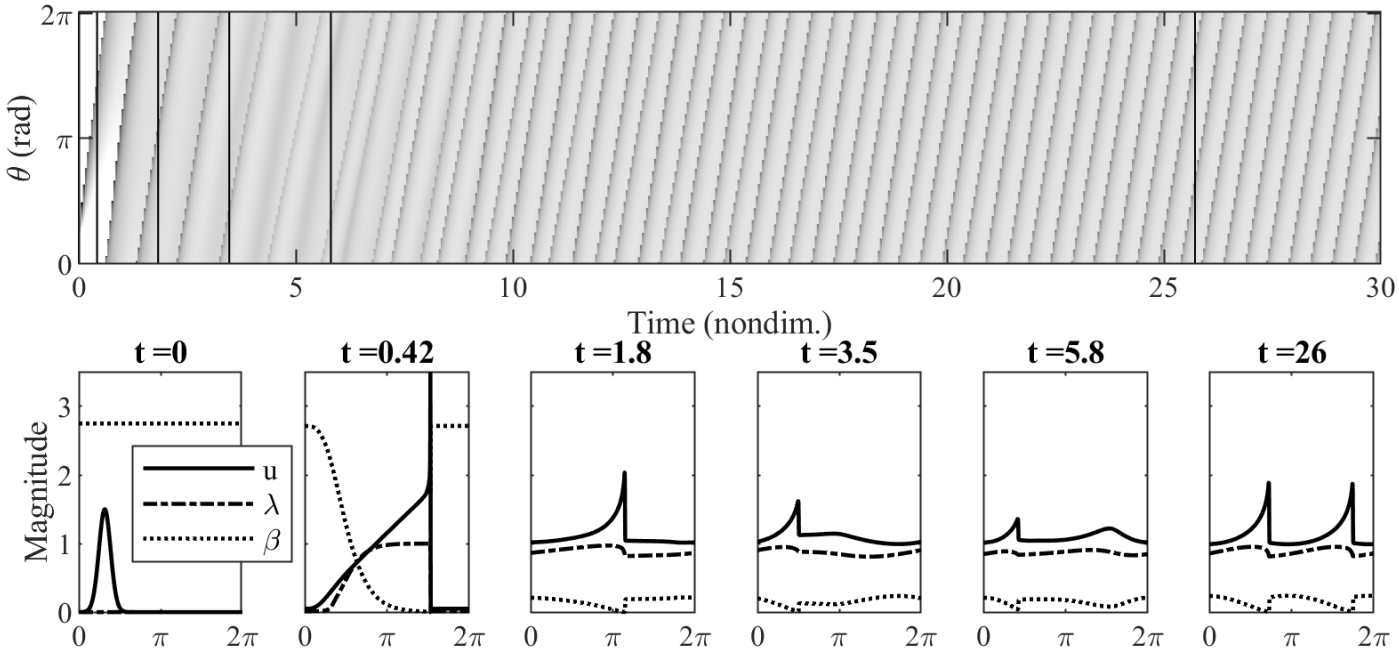

Figure 3.13: Nucleation and mode locking of detonations from a single pulse initial condition ($s = 7.0$). Vertical lines in the $\theta - t$ diagram correspond to simulation snapshots shown. The initial *sech*-pulse rapidly transitions to a CJ detonation. In regions where u is low, the injectors behave steadily. However, as the wave reaches its tail, u is everywhere elevated and the injection is severely curtailed. A second wave forms from the self-steepening of parasitic deflagration. After wave nucleation, the two waves behave dispersively and their phase differences approach π.

3.3 Numerical Experiments

In this section, a set of numerical experiments are presented that exhibit phenomena characteristic of the system of Eqs. 3.18-3.19. Numerical simulations are performed with the PyClaw open source finite volume software [91] on a converged grid. The parameters used for the numerical simulations in this article are given in Table 3.1. Exceptions are noted as appropriate.

3.3.1 Planar Fronts

We first examine the existence of planar solutions to the model system, including limit cycle behavior. The initial value problem was solved with initial condition $u(x,0) = 1$ and $\lambda(x,0) = 0.75$. A plane wave oscillates about the point in phase space where gain depletion and gain recovery match ($\beta\lambda = (1-\lambda)\omega(u)$) subject to the balance of energy input and energy rejection and dissipation ($\epsilon\xi = (1-\lambda)\omega(u)q_0$). Low-energy oscillations decay to a planar deflagration front without oscillations. Pulsating fronts, such as those seen in recent experiments, are characterized by periodic 'activation' and 'deactivation' of the injectors - first resonating with the heat release, and subsequently saturated by the loss mechanisms. An example of a plane wave pulsating front can be seen in Figure 3.17d for a single location in the annulus through time. The corresponding space-time history for the pulsating mode of operation is given in Figure 3.17c.

3.3.2 Traveling Waves

For traveling wave simulations, the initial value problem with initial condition $u(x,0) = (3/2)\text{sech}^2(x - x_o)$ and $\lambda(x,0) = 0$ was solved under varying refill (s, holding u_p constant) conditions and with linear and nonlinear loss terms.

As in [71], found is the analogous CJ velocity of the reduced system (the inviscid, steady wave in which all energy has been released to the wave in a infinitesimally thin reaction zone). This steady wave speed is defined as the minimum speed that fulfills the Rankine-Hugoniot conditions for the prescribed heat release. In the absence of losses, this minimum speed (CJ velocity, D_{CJ}) is $D_{CJ} = (u_1 + q_0) + \sqrt{q_0\,(q_0 + 2u_1)}$, where η_1 is the upstream state of a steady, shock-attached framework of the Majda Model. In the

case of $u_1 = 0$, the speed of the CJ wave becomes $D_{CJ} = 2q_0$. This speed is the metric upon which the traveling waves in the proposed model are benchmarked.

The evolution of a typical simulation is given in Fig. 3.13. Because the initial *sech*-pulse is well above u_c, the medium locally and rapidly releases heat. The wave steepens and forms a detonation. This initial pulse travels at the CJ speed until it reaches its tail, at which point the wave begins to rapidly dissipate and decelerate: the limited amount of gain recovery cannot continue to sustain the wave at $D_{CJ} = 2q_0$. Additionally, the rapid heat release (compared to the time scale of the dissipation of energy) of the initial CJ wave acts to raise the average u in the domain substantially above the ambient value u_0 and ignition value u_c. In this manner, the *effective* activation energy of the active medium is lowered and parasitic deflagration, or slow-scale heat release not associated with the traveling waves, is promoted in the entirety of the domain. Because the transit time of the initial traveling wave has been increased through dissipation, the parasitic deflagration has ample time to complete the deflagration-to-detonation (DDT) process and form multiple, lower amplitude detonation waves.

To induce a mode transition from an already mode-locked state, a step change in s is applied to the steady state, inducing a bifurcation. An example of such a transition is shown in Fig. 3.15b, where two initially mode-locked rotating detonation waves become unstable and destructively bifurcate. Low-amplitude phase difference oscillations grow exponentially, much like the experimental observations in Fig. 3.15a. During the period of oscillations, the two waves exchange strength (amplitude) and speed. For a given injection function β and loss ϵ, the instability growth rate and oscillation period is parameterized by the severity of the applied step in s and u_p.

3.4 Discussion

The presented model system qualitatively reproduces the nonlinear dynamics of collections of rotating detonation waves observed in experiments. The proposed system is an adaptation of the Majda detonation analog to a periodic domain with gain depletion, gain recovery, and generic restoring forces included in the system. These terms sufficiently mimic real-engine processes such as heat release, propellant injection, and rejection of

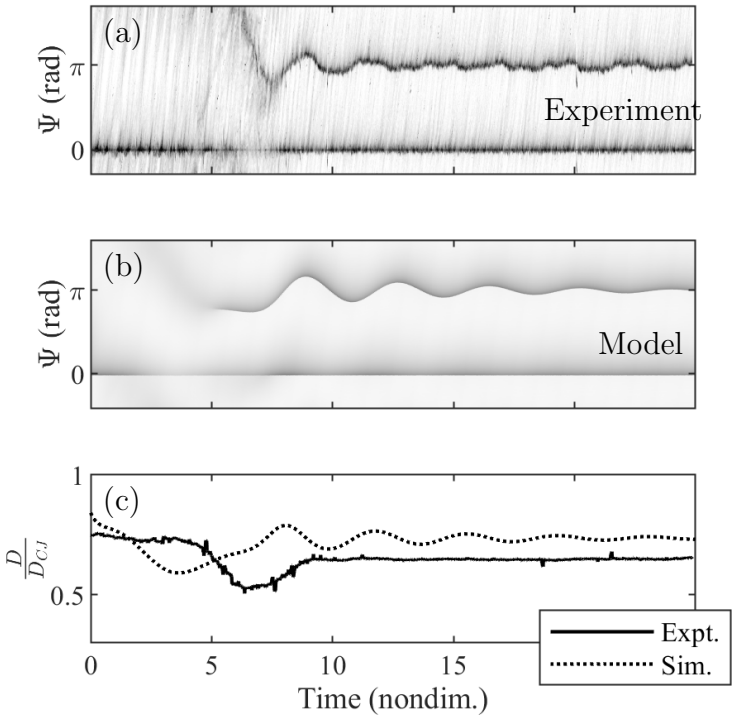

Figure 3.14: Representative wave nucleation process in a startup transient in an experiment (a) and in a simulation of the proposed model (b) displayed as pseudocolor plots of amplitude (arb. units). As seen in the wave reference frame of (a) and (b), the oscillatory phase difference between the two waves immediately after nucleation decays through time as the two waves become mode-locked. (b) corresponds to $s = 7.0$. The instantaneous speeds of the waves along $\Psi = 0$ in (a) and (b) are given in (c).

energy to an ambient condition. While not all physical processes in real engines have been explicitly captured, nor have the functional forms for the included terms been perfectly identified, the claim is that the dominant balance physics involved in the nonlinear dynamical behavior seen in real engines has been identified and correctly coupled. The *experimentally observed* and *model-reproduced* phenomena include wave nucleation (Fig. 3.14), mode locking of multiple waves (Fig. 3.13), wave destruction (Fig. 3.15), wave modulation (Fig. 3.16), and pulsating plane waves (Fig. 3.17).

3.4.1 Energy Flux

The model's steady (or quasi-steady) state exists when the energy flux into and out of the domain balance. This condition is met when the integrated losses are equal to the

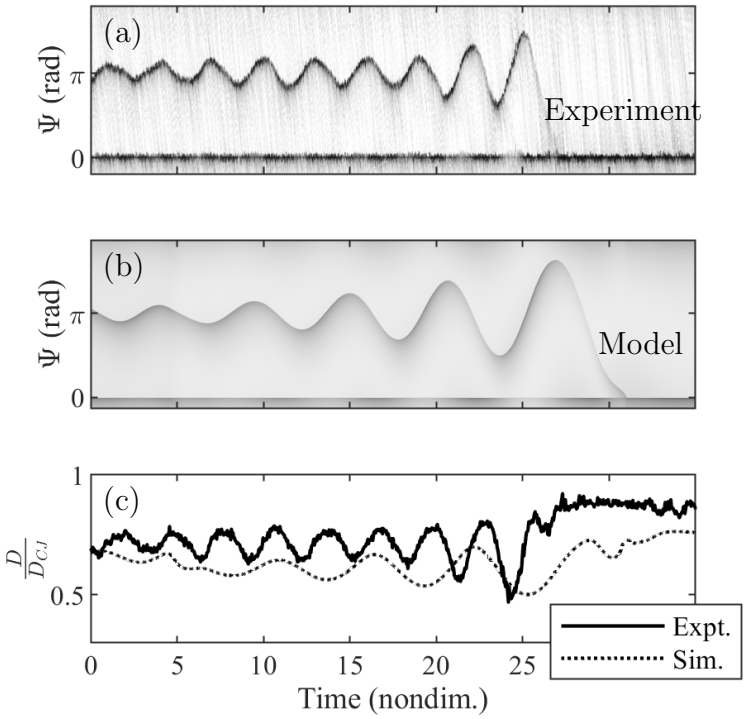

Figure 3.15: Representative destruction of a wave in an experiment (a) and in a simulation of the model (b) shown in the wave-attached reference frame as pseudocolor plots of amplitude (arb. units). Oscillations in Ψ grow exponentially until one wave overruns the other. For a given injection function β and loss ϵ, the oscillation period and phase difference growth rate are parameterized by the change in s and u_p. (b) corresponds to $s = 4$ with a -20% change in s applied to the mode-locked state. The instantaneous speeds of the waves along $\Psi = 0$ in (a) and (b) are given in (c).

integrated heat release over the domain:

$$\dot{E}_{domain} = \int_0^L q(1-\lambda)\omega(u)dx - \int_0^L \epsilon u^2 dx \tag{3.22}$$

For steady planar deflagration fronts and mode-locked traveling wave solutions, the integrals exactly balance and $\dot{E}_{domain} = 0$. For oscillatory plane waves, $\dot{E}_{domain} \neq 0$: there is periodic accumulation and ejection of energy in the domain that oscillates in-phase with injection and heat release, similar to the autoignition model of Frank-Kamenetskii [81, 82].

Transient phenomena, such as the initial start-up of a simulation or immediately after

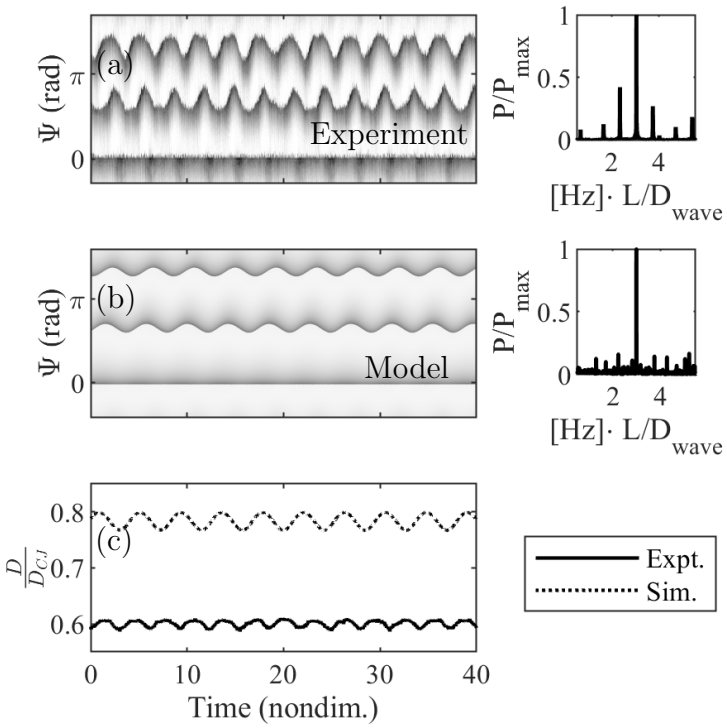

Figure 3.16: Space-time history of mode-locked modulation of wave speeds an experiment (a) and in a simulation (b) in the wave reference frame. The instantaneous speeds of the waves along $\Psi = 0$ in (a) and (b) are shown in (c). The accompanying spectra show clear sidebands symmetric about the carrier frequency. The frequency shown in the spectra is scaled by the average transit time of the mode-locked wave, L/D_{wave}. The abscissa magnitude corresponds to a count of the waves in the domain. As shown, the dominant frequency is three waves with sidebands near two and four waves.

ignition of an RDE, exhibit an imbalance of the integrals in Eqn. 3.22: $\dot{E}_{domain} > 0$. From the initial condition of zero combustion, the losses in the chamber are minimal. An accumulation of u will occur until the domain satisfies the relationship in Eqn. 3.22. A direct consequence of this behavior is the influence of the accumulation of u on the kinetic model. As u increases with the onset of combustion, the chemical reactions governed by the simplified Arrhenius kinetics are *accelerated*. This feedback mechanism promotes deflagration in the entirety of the domain, which can then transition to a number of detonations. This process is the physical mechanism for wave nucleation in RDEs.

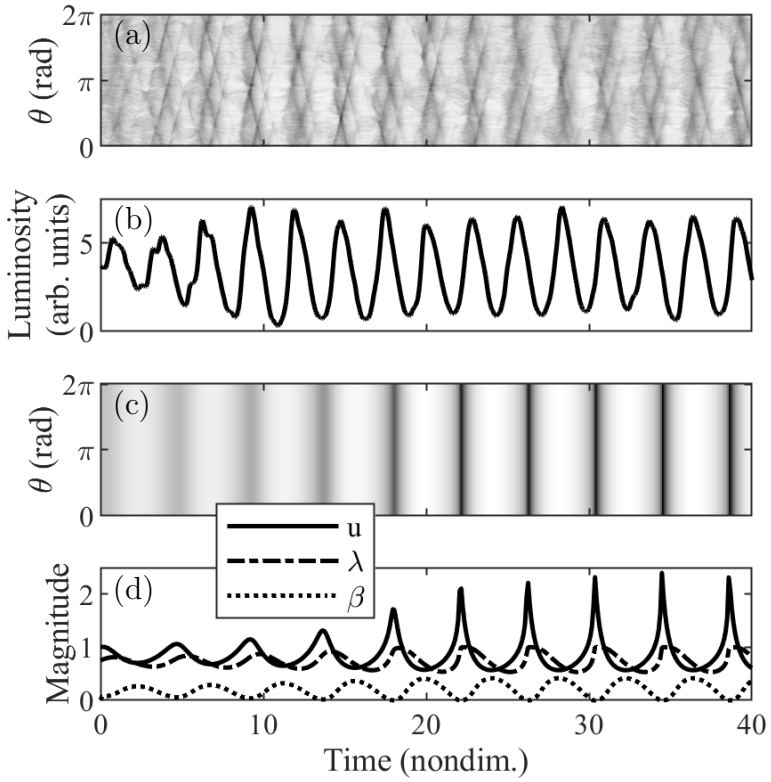

Figure 3.17: Space-time history of plane wave pulsation mode of operation in an experiment (a,b) and in a simulation (c,d). Simulation parameters are those listed in Table 3.1 with $q_0 = 6$ and $\epsilon = 1.0$. The deactivation and reactivation of the injectors gives rise to a resonance between the combustion and propellant injection.

3.4.2 Communication Pathways

In steady operation of an RDE and in the mode-locked state of the proposed model system, a number of traveling detonation waves co-exist in the periodic domain with maximum possible phase differences between the waves. Supposing these traveling waves to be detonations, there is an implied lack of communication between the waves: detonations travel supersonically and, if steady, in a condition where the combustion products are sonic relative to the wave front. For the waves to behave dispersively, as in Figs. 3.14 and 3.15 near the bifurcation points, implies a significant communication pathway or coupling mechanism in an apparent contradiction to standard detonation theory. Noted is that the propellant injection scheme is responsible for providing a consistent combustible medium through which the detonations can propagate. However,

known is that detonations induce blockages or backflow into propellant plenums. This phenomena is captured in the proposed functional form of β in Eq. (3.21), providing a necessary feedback mechanism between the detonations and the injection scheme. In this manner, the presence of all detonation waves is impressed upon the dynamic response of the injection scheme and long-range communication is established, allowing for dispersive behavior of the detonation waves. The coupling of the injectors and the detonation waves is the primary physical mechanism that drives the observed dynamics in both experiments and in the proposed model.

Chapter 4

Model Properties and Bifurcations

This proposed model marks a significant departure from the modeling 'state-of-the-art' in that it stresses global energy dynamics and long-time behavior over accuracy and device- and condition-specific computational studies. The approach adequately captures the non-locality (meaning the behavior at a single spatial location is coupled to all other locations) of the energy balance that leads to the diverse behavior seen in experiments. The physics are simplified in this approach: for the pulses to steadily propagate, gain and loss must exactly offset, subject to the nonlinearity (possessing a Burgers'-type flux) and periodicity of the medium. This perspective is adopted from the nonlinear waves community (see [92, 74, 93]). Localized structures that self-organize and propagate as a response to energy pumping from an external source are called dissipative solitons or *autosolitons*. Rotating detonation waves are classified as such.

To adopt the view of solitonic propagation of rotating detonation waves has high value. The physical processes responsible for pulse shape and behavior are known. This view therefore de-emphasizes the hardware or condition-specific considerations and does not require the resolution of the complete flow field. Potentially the greatest benefit of this perspective are the ability to determine relationships between stability, performance, and model parameters.

In this section, investigated are the the bifurcations and autosolitonic properties of the proposed model. First, experimental observations are reviewed for convenience, now in

the context of solitonic propagation. Next, a bifurcation study is performed through direct numerical simulations of the model system and through numerical continuation.

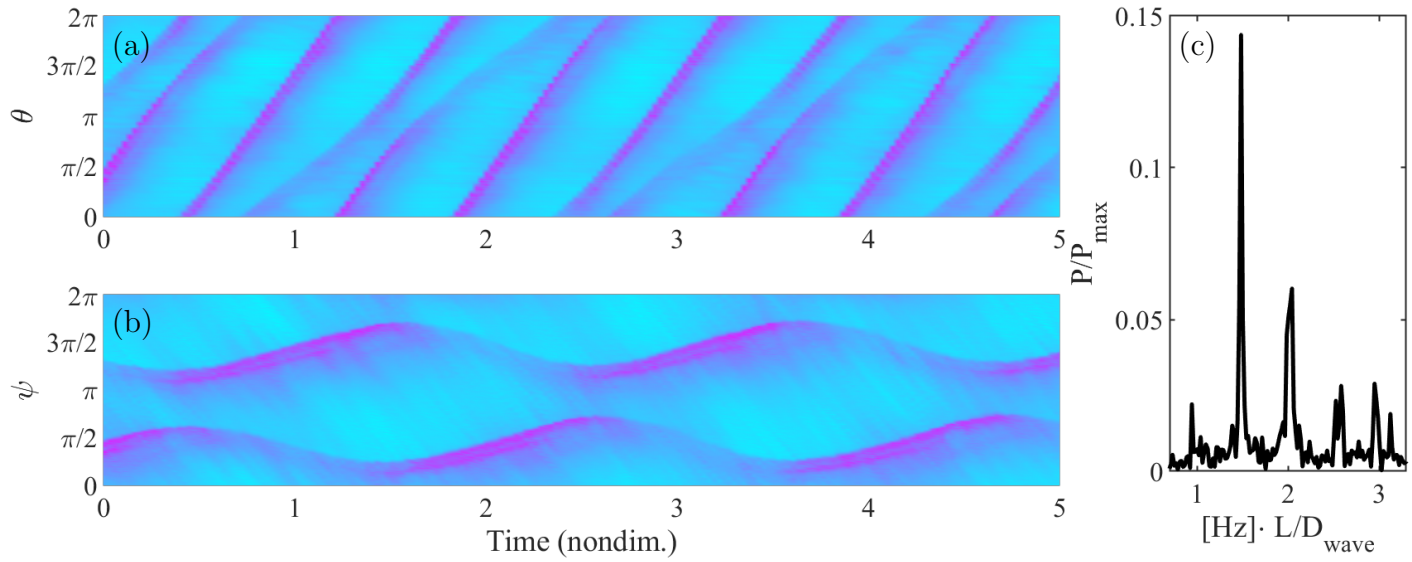

Figure 4.1: Raw integrated pixel intensity of RDE annulus through time is shown in (a) for an experiment with large-amplitude modulation. The two waves present in the domain exchange strength and amplitude in a regular fashion. At each wave collision, the waves nonlinearly interact, leaving an observable phase shift in the trajectories of the waves. The data shown in (a) is recast into the mean-velocity reference frame in (c). Here, the oscillations in phase difference between the waves is explicit. The accompanying spectrum in (c) shows the frequency content in terms of wave count (unit of abscissa). Sidebands exist symmetric about the wave count frequency of two, though dominating the frequency content is the lower sideband as this experiment is near a bifurcation point to one wave.

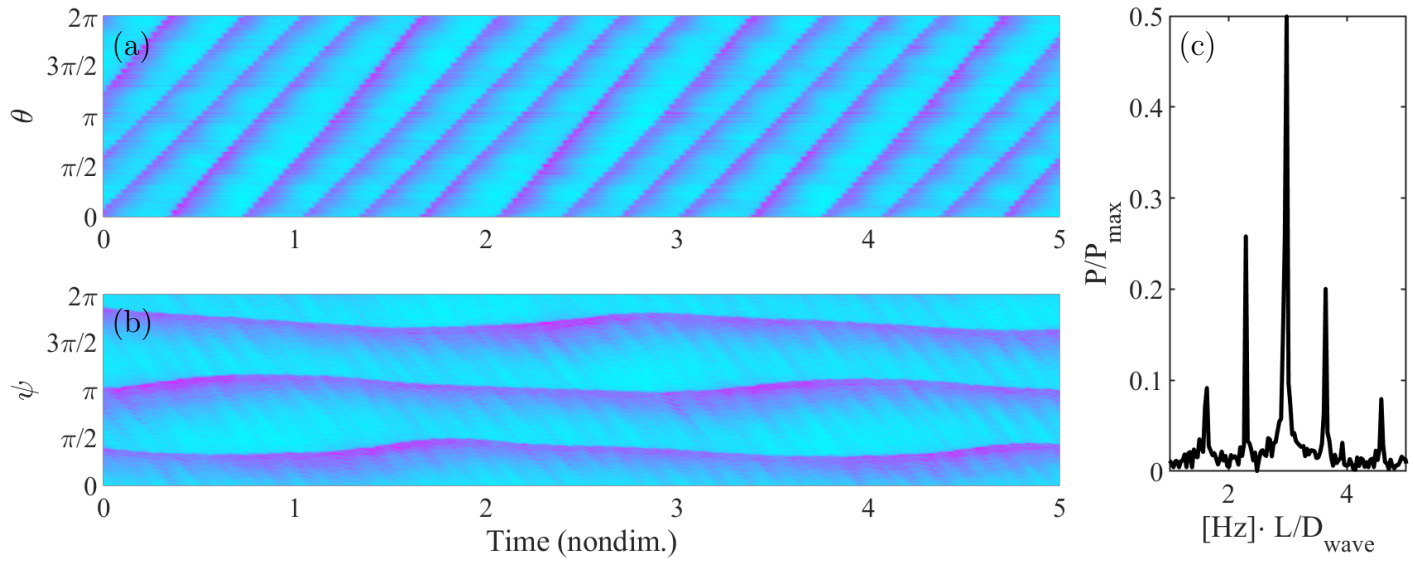

Figure 4.2: Shown in (a) is raw pixel luminosity for a three-wave modulation case in the laboratory reference frame. Recasting this to the mean-velocity reference frame (b), the oscillations in phase difference become explicit. Although this instability is the same type as displayed in the two wave case of Fig. 4.1, the amplitude of the modulation is less severe. The spectrum of the experiment is shown in (c), with sidebands near wave counts of two and four symmetric about the carrier frequency of three waves.

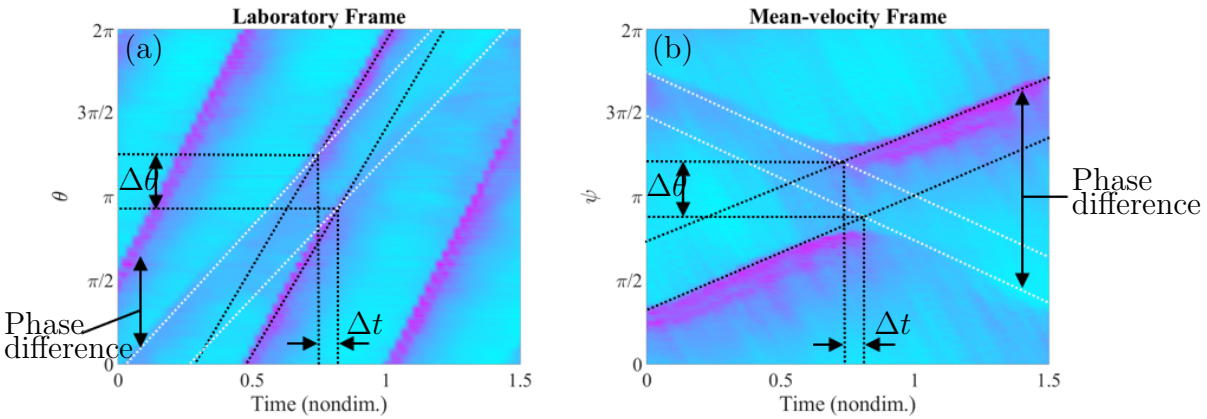

Figure 4.3: A single period of modulation for the data in Fig. 4.1 in the laboratory reference frame is shown in (a). The two waves present in the combustion chamber interact nonlinearly, producing observable time and phase shifts. Such kinematic traces are hallmarks of solitonic interactions. The data in (a) is shown in the mean-velocity reference frame in (b).

4.1 Experiments

Presented here a subset of experiments that exhibit a modulational instability with the goal of characterizing this phenomena with the proposed model system. Figures 4.1 and 4.2 show different numbers of waves in the annulus that travel with a modulated speed, amplitude, and phase difference. For these figures, plotted are these histories against time normalized by the average round-trip time of a wave. The time units correspond to number of round trips. Raw integrated pixel luminosity for a two-wave modulation case is given in Fig. 4.1a. In viewing this space-time history, it is apparent that in this experiment the waves have two modes of propagation. The first mode is characterized by a stronger (higher amplitude), faster moving pulse. The second mode is characterized by a significantly weaker, slowly moving pulse. The two co-existing waves in the RDE annulus regularly alternate between these propagation modes. The point at which the waves 'switch' modes is at the local maxima of the modulation; i.e., when the two waves are closest together. At this close range, a fundamentally different balance physics exists that changes the behavior of the waves. The strengths and speeds of the waves are directly tied to the amount and distribution of available reactant in the annulus. Immediately after a wave-pair interaction, the (now) faster of the two waves has an excess of reactant through which it can propagate stably (with a constant velocity

and amplitude). This imbalance of propellant distribution exists because: (i) the weaker wave has not blocked propellant injection to the degree that the stronger wave has, and (ii) a temporal imbalance exists corresponding to the large amplitude phase differences of the waves. Because the stronger wave travels faster than its counterpart, it approaches the tail of the slower wave, where the amount of renewed reactant is significantly less than required to sustain the speed and amplitude of the strong wave. This strong wave therefore decelerates, as the dissipative processes (exhaust) now dominate the physics. At this point of interaction, the phase difference between the strong and weak waves is small - on the order of 45 degrees or $\pi/4$ radians. The accompanying phase difference - the one preceding the weak wave - is therefore $2\pi - \pi/4$. With these large phase differences (and accompanying time lags), reactant regeneration asymptotically approaches a state of complete 'refill', where no combustion products are present in the flow and the reactant is fully mixed. The weaker wave now rapidly gains strength: the input energy to the wave overwhelms the dissipative processe. Finally, the transition to the stronger mode of propagation is complete when the energy input to the wave exactly balances the dissipative processes. This saturation of the growth of the waves is explicitly seen in the spatio-temporal history of the experiment: the paths of the waves are straight lines (paths of constant velocity) connected by brief periods of nonlinear wave-to-wave interaction. Displayed in Fig. 4.2a is similar time-periodic modulation, though with three waves.

All experiments possessing this modulational instability share a similar spectrum. A carrier frequency corresponding to the average velocity (or, if normalized as in Figs. 4.1c and 4.2c, a count of the waves in the domain) is accompanied by sidebands symmetric about the carrier frequency. By recasting the wave trajectories into the reference frame of the velocity corresponding to the carrier frequency, one can visualize the same dynamics as deviations from the average velocity. The sidebands in the spectra correspond to frequencies near that which would appear for an increment or decrement in number of waves. For example, for the three wave case of Fig. 4.2, the spectrum shows a dominant (carrier) frequency of three waves with sidebands at approximately two and four waves. Figure 4.1b is the representation of the data contained in Fig . 4.1a recast into the reference frame of the mean velocity of the waves. In this reference frame, the oscillations of phase difference about $\psi = \pi$ phase differences is explicit, as is the modulation of wave amplitude. The lower-amplitude modulations of Fig. 4.2 do exhibit

the same characteristics of the two wave case, through the range of interaction for these cases is observably larger than that of the two wave case.

In the brief wave-to-wave interactions, the waves exhibit clear solitonic behavior. The strong wave assumes the shape and velocity of that of the weaker and is displaced by a small phase shift. Likewise, the weak wave assumes the shape and velocity of that of the stronger wave - again displaced by a small phase shift. This interaction is most easily observed with close-scale interactions. In Fig. 4.3, displayed is a single period of oscillation extracted from the two wave modulation case of Fig. 4.1. The time shifts Δt yielding phase shifts $\Delta\theta$ give the interaction the appearance of a solitonic collision.

4.2 Autosolitonic Propagation and Bifurcations

The goal of this section is to use the proposed reduced-order mathematical formulation to (i) reproduce, qualitatively, the modulational instability and solitonic interactions of collections of rotating detonation waves, and (ii) characterize the conditions under which these instabilities develop. Using this model, a sweep of numerical simulations to survey wave behavior and produce a simulation-based bifurcation diagram. Lastly, numerical continuation is used to extract the traveling wave branches (and deviating branches) as a function of a bifurcation parameter.

4.2.1 Bifurcation Structure: DNS

PyClaw [91] is used to perform the direct numerical simulation portion of the bifurcation study. The Matlab-based software pde2path [94, 95] to perform the numerical continuation. However, the model system as written in Eqns. 3.19 and 3.18 admits solutions with discontinuities. Although PyClaw is well-suited to handle shocks, pde2path was originally intended for systems of elliptic partial differential equations. To facilitate the bifurcation analysis, the model system is necessarily regularized with diffusion such that the solutions become continuous, albeit still possessing sharp gradients characteristic of the reaction fronts. The bifurcation study is therefore performed on the modified system:

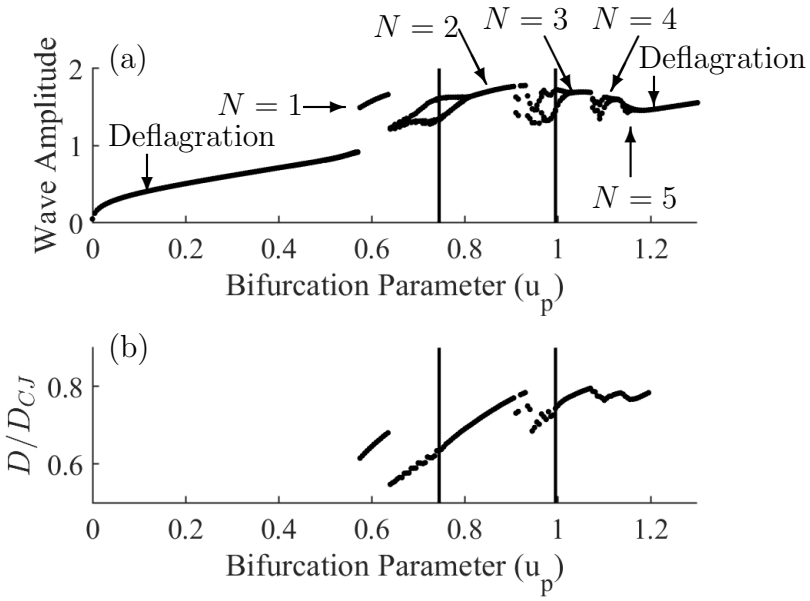

Figure 4.4: A bifurcation diagram of the RDE model analog showing peak amplitude of the simulated domain is shown in (a). Model parameters are listed in Table 3.1. In increasing the bifurcation parameter u_p from zero, the system initially exhibits planar deflagration fronts, then traveling waves (from 1 to 5 waves), then back to a deflagration front. The associated speeds of the traveling waves are given in (b).

.

Table 4.1: Bifurcation study parameters

L	q_0	α	u_c	u_0	s	k	ϵ	r	ν_1	ν_2	D_{CJ}
2π	1.0	0.3	1.1	0	3.5	1	0.15	5	0.0075	0.0075	2

$$\frac{\partial u}{\partial t} = \nu_1 \frac{\partial^2 u}{\partial x^2} - u\frac{\partial u}{\partial x} + kq\,(1-\lambda)\,e^{\frac{u-u_c}{\alpha}} - \epsilon u^2 \tag{4.1}$$

$$\frac{\partial \lambda}{\partial t} = \nu_2 \frac{\partial^2 \lambda}{\partial x^2} + k\,(1-\lambda)\,e^{\frac{u-u_c}{\alpha}} - \frac{s u_p \lambda}{1+e^{r(u-u_p)}}, \tag{4.2}$$

where the constants ν_1 and ν_2 are diffusivities associated with the combustion (diffusing u) and injection (diffusing λ) processes, respectively. The model parameters used in this study are listed in Table 4.1.

A bifurcation diagram showing the peak amplitude of the domain as a function of the parameter u_p (injection sensitivity threshold) is shown in Fig. 4.4, as computed by numerical simulation on a converged grid with PyClaw. Each simulation was initialized

with a singe localized pulse $u(x,0) = (3/2)sech^{20}(x-1)$ with a "half combustion" condition of $\lambda(x,0) = 0.5$.

At $u_p = 0$, the injection term β is zero and the entire domain dissipates to a zero value. As u_p increases, a planar deflagration front forms: the dissipation term $(-\epsilon u^2)$ first dominates the dynamics of the domain, prohibiting the formation of stable pulses, then relaxing to exactly balance the input energy given by a non-zero β. At a critical value of $u_p \approx 0.56$, the initial pulse can form a single stably-propagating wave of a significant amplitude. At this condition, the input-output energy balance is still satisfied, but the time scale corresponding to the round-trip time of the wave (the speed of which is determined by the energy release associated with the Arrhenius kinetics) has become comparable to the time scales of gain regeneration (su_p) and dissipation. Continuing to increase u_p increases the peak amplitude of the single wave until $u_p \approx 0.65$, where a transition to two waves occurs. This transition marks the point at which the mean value of u in the domain has accelerated the kinetics to the point where the effects of parasitic deflagration (combustion that is not associated with the traveling waves) and detonative combustion on the domain are of the same order. The single wave's amplitude decreases as the parasitic deflagration is consuming a increasing amount of the available energy. Once the parasitic deflagration can self-steepen to form a shock during the round-trip time of a detonation wave, a deflagration-to-detonation transition occurs and the number of waves increases by one. This transition is seen in Fig. 4.4 when increasing u_p above 0.65 (a transition from one to two waves) and again around 0.9, 1.07, and 1.1. As u_p becomes large (beyond $u_p \approx 1.1$), the domain regresses back to a planar deflagration front. The time scale of the kinetics is now much faster than all others in the model, including that of the traveling waves. All input energy input is quickly consumed and dissipated.

The inter-pulse regions of the bifurcation diagram show a diverse set of behavior, including wave modulation. In Fig. 4.4, the vertical lines correspond to the simulation histories of Fig. 4.5 for two and three wave cases. For this region of operability space in u_p, the waves travel unsteadily with modulation similar to that which is observed in experiment (Figs. 4.1 and 4.2). In the bifurcation diagram of Fig. 4.4, the wave modulation for the two wave branch is bounded by stable two wave propagation on both

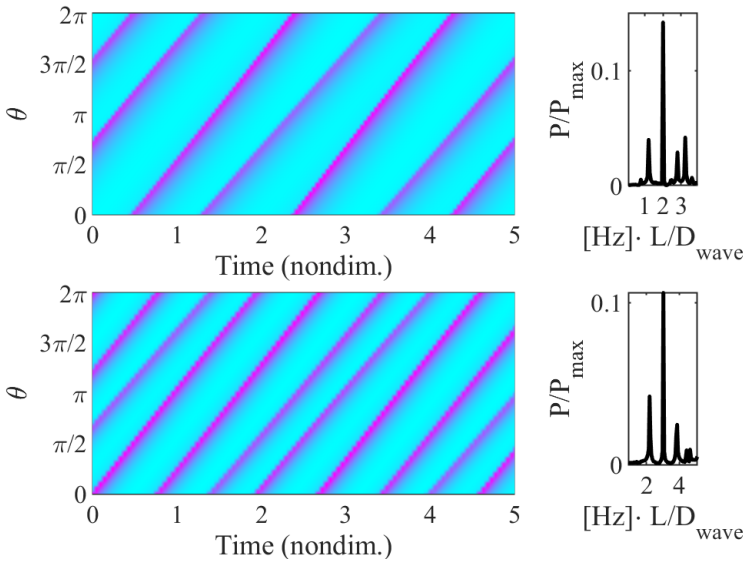

Figure 4.5: Modulated wave trajectories in the laboratory reference frame from numerical simulations corresponding to the vertical lines in Fig. 4.4.

sides of the instability. The modulation region for the three wave branch is bounded by a jump to the two wave branch and by stable three wave propagation.

The bifurcation diagram of Fig. 4.4 shows structure. A planar delfagration branch exists and is predominantly linear with u_p. Branches exist for each number of traveling waves that interact in some manner, giving intervals of u_p where the wave dynamics are not steady. Transitioning from steady propagation (a number of waves moving at constant velocity) to unsteady propagation constitutes a bifurcation to an instability.

4.2.2 Bifurcation Structure: Numerical Continuation

The continuation software pde2path uses the finite element method to analyze partial differential equations of the form

$$\frac{\partial u}{\partial t} = -G\left(u, \mu\right) \tag{4.3}$$

$$G\left(u, \mu\right) = -\nabla \cdot \left(c \otimes \nabla u\right) + au - b \otimes \nabla u - f \tag{4.4}$$

where u is a function of space and time, μ is a vector of parameters, and the variables a,b,c correspond to the linear, advection, and diffusion tensors, and f is the nonlinearity.

In the finite element formulation on a discretized domain, this reads as:

$$M\dot{u} = -G(u,\mu) \tag{4.5}$$

$$G(u,\mu) = Ku - Mf(u,\mu) \tag{4.6}$$

where M is the mass matrix, K is the stiffness matrix (diffusion term), and Mf is the nonlinearity. The model exists on a periodic domain, meaning that a continuous symmetry exists that must be eliminated before attempting continuation. This is achieved by augmenting the system with an additional bifurcation parameter, v, corresponding to velocity, such that the *imposed* speed exactly offsets the motion of the waves. Therefore, the model system 4.1-4.2 is recast as:

$$\begin{aligned} G = &\begin{pmatrix} \nu_1 K - vK_x & 0 \\ 0 & \nu_2 K - vK_x \end{pmatrix} \begin{pmatrix} u \\ \lambda \end{pmatrix} - \begin{pmatrix} -\frac{1}{2}K_x u^2 \\ 0 \end{pmatrix} \\ &- \begin{pmatrix} M & 0 \\ 0 & M \end{pmatrix} \begin{pmatrix} kq(1-\lambda)\exp\left(\frac{u-u_c}{\alpha}\right) - \epsilon u^2 \\ k(1-\lambda)\exp\left(\frac{u-u_c}{\alpha}\right) - \frac{su_p\lambda}{1+\exp(r(u-u_p))} \end{pmatrix} \end{aligned} \tag{4.7}$$

The continuous symmetry associated with the periodic boundaries has been removed by the addition of this phase constraint. We use wave profiles from the direct numerical simulations from Fig. 4.4 to initialize the traveling wave branches for continuation.

To compute time-periodic orbits along branches emanating from a detected Hopf bifurcation, an additional constraint must be imposed to fix the translational invariance in time [95]. Here, the imposed velocity of Eq. 4.7 is redefined to be the average velocity over the period of oscillation of the Hopf orbit. By defining a reference profile (the steady traveling wave profile, for example), the profile at each time slice can be compared to this reference, producing a deviation of traveling wave speed. Over one period of modulation, the average of these deviations from the reference profile are forced to be zero. Thus, time-periodicity is enforced and the translational invariance (in time) is fixed with respect to a reference profile.

Using the numerical simulations from Fig. 4.4 as initialization seeds, an estimate of the

complete bifurcation diagram is constructed using pde2path for the parameters listed in Table 3.1.

Figure 4.6 contains several distinct branches of solutions for the model system: one 'trivial' branch and five traveling wave branches. Along these branches, solid lines indicate regions of stability whereas dotted lines indicate unstable regions. The 'trivial' branch is the locus of points satisfying the input-output energy balance with no contributions from traveling waves. This is the *deflagration* branch: the locus of solutions where a planar front spanning the domain consumes and quickly dissipates all input energy. Because of the viscous regularization of the model system, there exists a small region of stability around this branch where diffusion inhibits wave growth. Note that in the system without viscous regularization, this is not necessarily the case. Any change in concavity with Burgers' type flux (without diffusion) leads to wave growth and shock formation, and therefore a perturbation off the deflagration branch may indeed lead to wave formation if the local energy gain exceeds the local energy dissipation.

The single traveling wave branch is a closed solution branch - an isola - that exhibits stability for the top half of the branch. The region of stability is bounded by fold bifurcations at the extremes of the isola. The solution branches of higher number of waves are qualitatively similar to the single-wave branch: each possesses a region of stability (with the exception of the five wave branch, which is everywhere unstable for these model parameters) bounded by bifurcations to instability.

The wave speeds along the branches vary dramatically - by a factor of two for some branches - though they saturate at about the same value across branches. Relative to the CJ speed of detonations for the Majda detonation analog ($D_{CJ} = 2q = 2$), their speed is about 80 - 90% of the theoretical maximum. As u_p and the number of waves increases, there is marked drop in wave speed and amplitude, consistent with direct numerical simulations and experiments with large wave counts [26].

Self-Similarity and Domain Length

In Fig. 4.7, the single- and double-wave branches of Fig. 4.6 plotted alongside branches of the same system but different domain lengths: $L = 2\pi$ (the original system), $L = 3\pi/2$, and $L = \pi$. The traveling wave branch for $N = 1$ on a $L = \pi$ domain is identical

to that of the $N = 2$ wave branch on a $L = 2\pi$ domain. The system is self-similar, scaled by domain length. Furthermore, the wave speeds are along these branches are also equivalent. Increasing the domain size from $L = \pi$, the $N = 1$ branch detaches from the deflagration branch and forms an isola. With further increase in domain size, the isola decreases in size. A point of criticality exists where the domain is too large to support a single wave: the transit time of the wave becomes too long compared to the time required for parasitic deflagration to self-steepen and form an additional wave. At this point of criticality, the $N = 1$ isola ceases to exist, though the $N = 2$ branch detaches from the deflagration branch and forms a new isola. This process of isola formation and destruction repeats indefinitely with each doubling of the domain length. Note, however, that the regions of stability of the self-similar branches ($N = 1$ on $L = \pi$ and $N = 2$ on $L = 2\pi$) are not consistent: for this set of parameters, instability only exists for wave count greater than one.

The Hopf Bifurcation to Wave Modulation

The traveling wave branches of Fig. 4.6 each possess a region of stability: the detonations propagate stably with a constant velocity through time. However, there exist Hopf bifurcations that spawn branches of periodic orbits away from the stably-propagating pulse train. By adding an appropriate Hopf constraint as described in Section 4.2.2, the continuous branch of orbits - the Hopf branches - can be extracted. For the two and three wave cases, these branches are shown in Fig. 4.8 with example solution plots. Note that for these branches, stability has not been evaluated - only the branch location in parameter space has been traced.

The branches intersect the traveling wave branches at two points. At each intersection is a Hopf bifurcation. Along these Hopf branches, the period of oscillation and the amplitudes of phase differences, wave amplitudes, and wave speeds are all modulated: the branches constitute the possible states of modulation for the given parameters. These variations in propagation behavior are exhibited in Fig. 4.8. At each intersection with the traveling wave branches (the end points of the curves in Fig. 4.8a), the modulation is low in phase difference amplitude, though the modulation onset frequency is about a factor of two faster for the higher energy (larger u_p) cases.

At each local extreme of phase difference oscillations, the waves interact solitonically as in the experiments of 4.1 and 4.2. From the collection of waves, the pair that interact exchange strength and undergo a phase shift. This is clearest in Figs. 4.8d and 4.8g-4.8h. At the onset of modulation (approached from a high u_p), the phase differences between the interacting wave pairs is large, as are the apparent phase shifts. As the oscillations in phase differences grow, the phase shifts between interacting pairs decreases. In the extreme limit of the three wave Hopf branch, the phase shifts become such that the weaker of the interacting waves is overrun and the phase shifts are zero, resulting in the reduction of the number of traveling waves. Similar phenomena occur for Hopf branches of higher wave count, as shown in Fig. 4.6 along the 4-wave Hopf branch.

Figure 4.9 compares a single-period of oscillation for two rotating detonation waves in an experiment and in simulation of the analog system. Both are displayed in the average-speed reference frame. The behavior of the waves in the experiment and model share the same qualitative behavior, including exchange of wave strength, and similar phase shifts through the interaction. However, the period of oscillation (shown in number of wave round-trips around the domain, based on average wave speed) of the model does not match that of the experiment, though the model likely is not quantitatively matching all timescales of interest (chemical, injection, mixing, and wave transit time). Note that no parameter selection techniques have been performed, nor has there been any fitting of the model to data. Provided the aforementioned time scales are such that the model can support traveling detonation waves, the bifurcation structure and wave interactions are qualitatively similar.

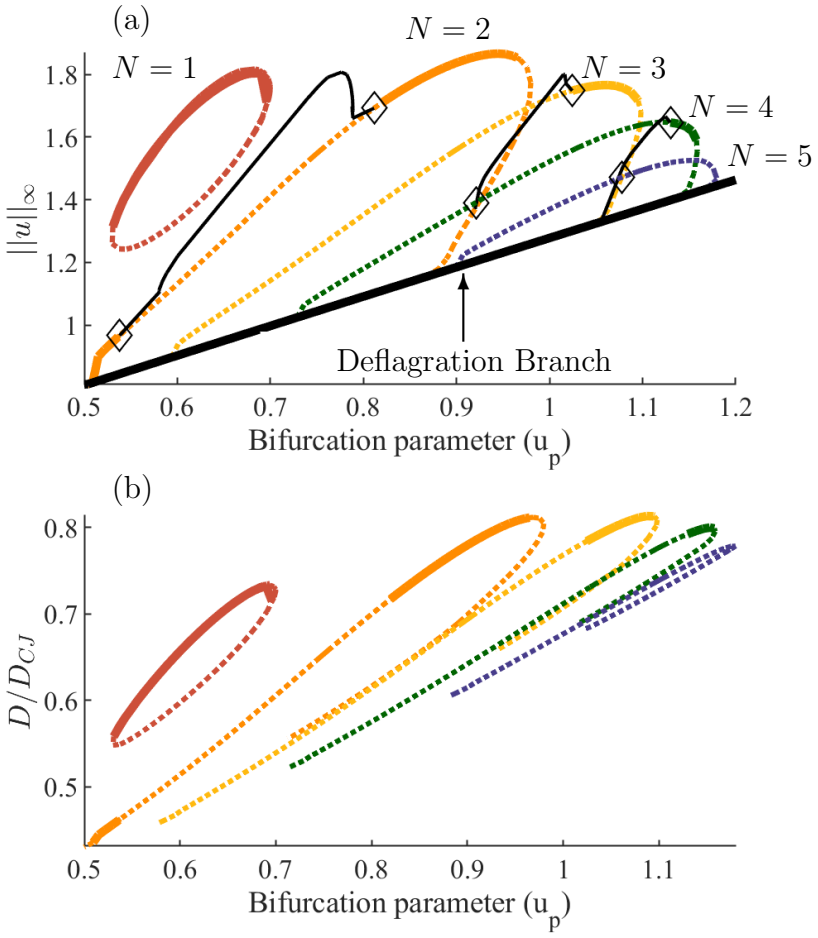

Figure 4.6: Bifurcation diagram replicating that of Fig. 4.4 computed from numerical continuation. Emanating from the trivial deflagration branch are 5 traveling wave branches. For each traveling wave branch, solid lines correspond to stable propagation and bashed lines correspond to unstable solutions. The single-wave traveling branch is a closed ring of solutions - an isola. Corresponding wave speeds along the traveling wave branches are shown in (b). Hopf bifurcations exist at the transition from stability to instability for the traveling wave branches, marked by diamonds. Along the Hopf branches are time-periodic modulations of wave speed, amplitude, and phase difference.

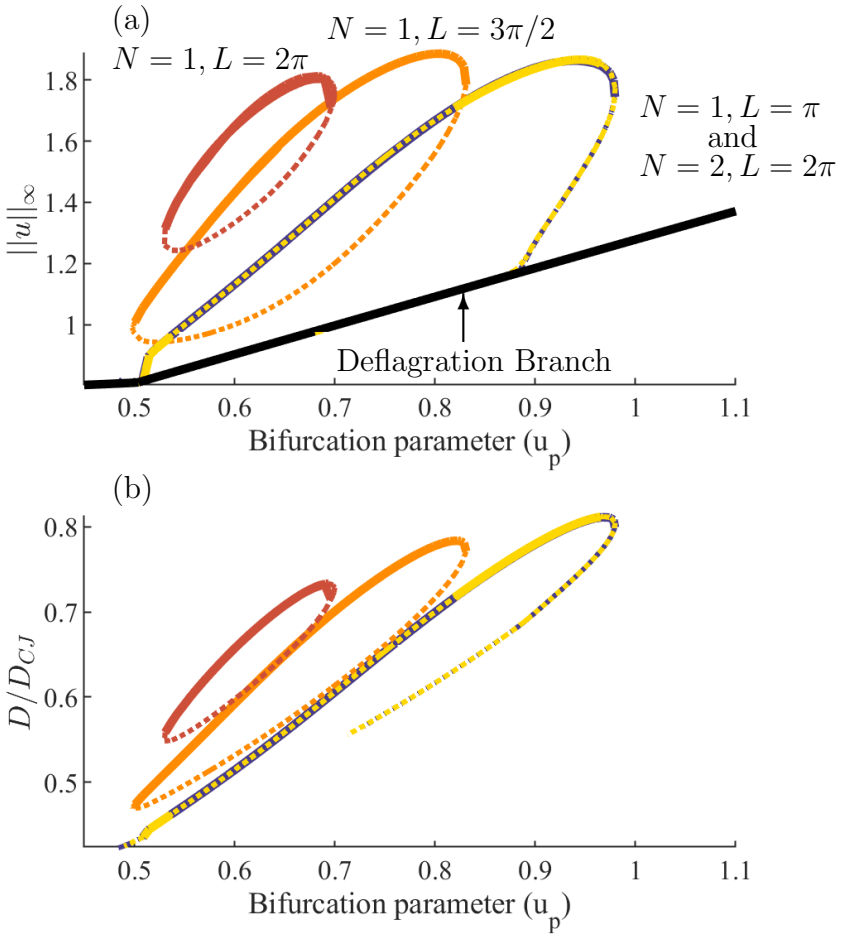

Figure 4.7: (a) A bifurcation diagram showing $N = 1$ and $N = 2$ branches of the original model system (domain length of $L = 2\pi$) alongside two additional cases: $N = 1$ on $L = 3\pi/2$, and $N = 1$ on $L = \pi$. Note that the traveling wave branches are self-similar - the curves of $N = 1$ on $L = \pi$ and $N = 2$ on $L = 2\pi$ overlay identically, including the wave speeds, shown in (b). The maximum wave speed and amplitudes for the model system with parameters listed in Table 3.1 shows strong dependence on the domain length, in effect changing the time scale for the round-trip time of the detonation wave.

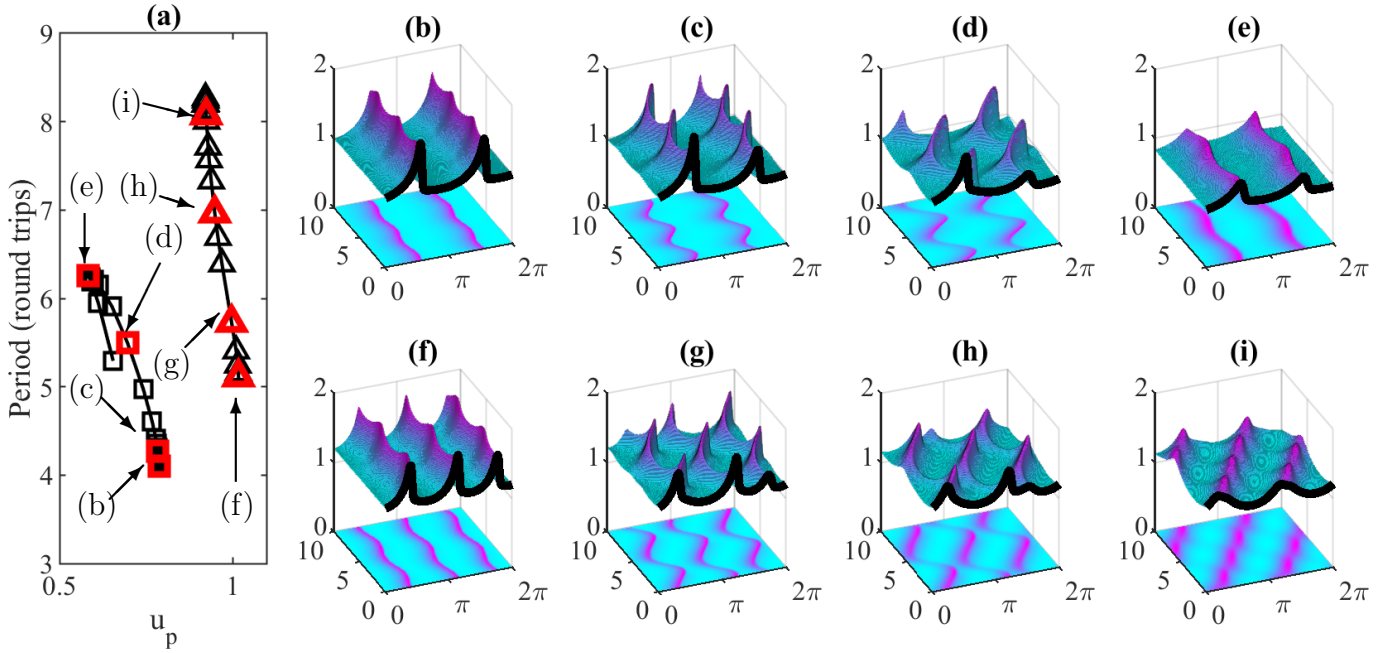

Figure 4.8: The two- and three-wave branches of the bifurcation diagram of Fig. 4.6 each possess regions of stability and instability. A Hopf bifurcation from the steadily traveling wave exists at these transitions. By continuing the Hopf branches, one can extract a diverse set of potential modulational behavior. In (a), the period of the Hopf orbits are displayed by number of wave round trips (based on wave speed averaged over one period) as a function of the bifurcation parameter. Example Hopf orbits for the two wave branch are shown in (b)-(e) and in (f)-(i) for the three wave branch. Along the Hopf branches, the amplitude of the phase differences and the waves vary dramatically. For the three wave branch, in the extreme limit of each wave-pair interaction, the stronger of the two interacting waves overruns the weaker wave, resulting in a reduction of number of waves by one. This phenomenon is shown in (i).

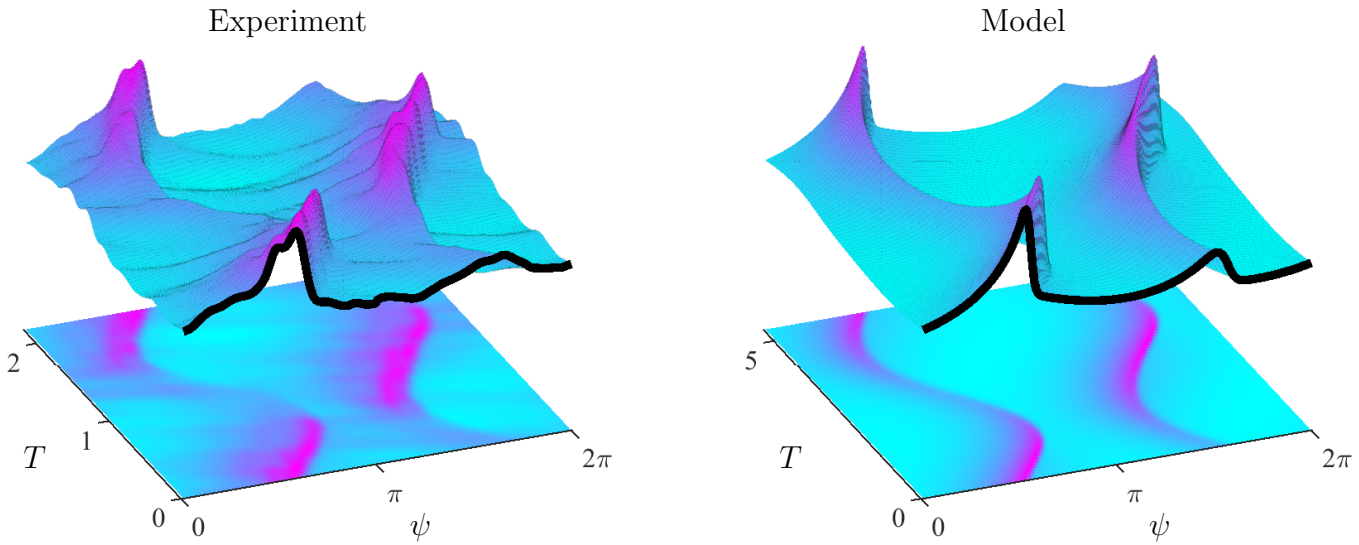

Figure 4.9: Extracted Hopf orbits after the onset of a modulational instability in an experiment and in the numerical continuation of the RDE analog system. The two detonation waves interact through global gain dynamics, producing a distinct and repeatable kinematic trace. The model is in good qualitative agreement with the experimentally obtained orbit.

4.3 Discussion

Rotating detonation waves have been experimentally observed to exhibit solitonic propagation, especially in wave pair interactions, where wave strengths are swapped and phase shifts are imposed (Fig. 4.9). In performing numerical simulations and a numerical bifurcation analysis of the rotating detonation analog system, the behavior of the waves seen in experiments has been qualitatively reproduced. Thus, the rotating detonation wave analog sufficiently mimics real-engine behavior, including the bifurcation structure, wave selection transients, and modulation of detonation waves.

In this section, the main findings of this section are emphasized and how they relate to the development of the rotating detonation engine. First, global gain dynamics are established as the mechanisms responsible for the observed physics. Next, the scales of interaction in the system and the solitonic behaviors they produce are discussed. Within this context, the modulational instability of rotating detonation waves is established as the *fundamental instability* of the system. Lastly, the engineering implications of this study are discussed, including stability, control, and scaling.

4.3.1 Global Gain Dynamics

The process of mode-locking of rotating detonation waves implies a significant communication pathway between the waves. This is a direct contradiction to classical detonation theory. Steady detonations are supersonically moving fronts, meaning they are 'unaware' of the fluid ahead of the wave. Similarly, the combustion products behind the detonation wave travel away from the shock front at a velocity sonic relative to the wave front. This implies that there are no characteristics that can propagate from the burnt side of the detonation upstream to the location of heat release. The rotating detonation engine possesses two physical constraints on the problem that lifts the restriction of wave (communicative) isolation. First, the domain is periodic, not infinite or pseudo-infinite in many classical studies, and second, the reactant ahead of the detonation waves is a function of the cumulative history of the detonation waves.

Periodicity means that the waves see the tail of the preceding wave (or, in the case of one wave, its own tail). The behavior of the detonation waves is necessarily dependent

not only on the local combustion at the shock front (where classical detonation theory stops), but also the time scales for energy dissipation and propellant recovery. These three physical processes have four different time scales corresponding to: (i) combustion, (ii) round-trip time of the detonation wave, (iii) dissipation (exhaust processes), and (iv) gain recovery (injection and mixing). These time scales vary by several orders of magnitude in real engines, with combustion being the fastest (sub-microseconds) and dissipation being the slowest (millisecond).

These time scales are related. The time scale of combustion is related to the amount of reactant ahead of the comubstion zone and the quality of the mixing processes. The transit time of the wave is governed by the heat release associated with the detonation wave (Chapman-Jouguet theory), but also by the properties of the ingested gas, as they are not necessarily at standard or injected conditions. Likewise, the properties of the fluid in the inter-pulse space is governed by the slower-scale dynamics of the exhaust processes. The rotating detonation analog succeeds in capturing the dynamics seen in experiments because the physical processes and their time scales are included and properly coupled.

We therefore claim that the *global gain dynamics* are responsible for the observed dynamics. It is insufficient to consider exclusively the physics of the front - classical detonation theory in this case - to describe the dynamics of the collection of waves. This approach also contrasts the convention of the field of autosolitons. Typical solitary structures in driven-dissipative systems are held together because of the *local* balance of gain, loss, nonlinearity, and dispersion. In the RDE, the local balance physics cannot be decoupled from the global gain dynamics.

4.3.2 The Fundamental Instability

The modulation seen in RDE experiments and simulations has been characterized as 'galloping' rotating detonation [96, 97, 27]. This term is adopted from the phenomenon whereby one dimensional detonations undergo a Hopf bifurcation to front modulation followed by period-doubling to chaotic propagation [32, 98]. In these studies, activation energy is typically taken to be the bifurcation parameter. Qualitatively, the behavior of 'galloping' detonation is very similar to the modulation seen in RDEs: the frontal motion of the waves and peak pressures oscillate through time, just as in Figs. 4.1 and 4.2,

though naturally the studies of 'galloping' detonation are performed on pseudo-infinite, 1-dimensional domains.

The viscous Majda detonation analog [71] does not exhibit the aforementioned nonlinear dynamics of real detonations. The *nonlinear stability* of detonations of the viscous Majda detonation analog has been evaluated with rigor with Evans function-based techniques [86, 87, 88] - indeed, no Hopf bifurcation exists "in a normal parameter range or in the limit of high activation energy" [88]. As the RDE analog system is fundamentally a modification of Majda's model to include global gain dynamics, claimed is that the inclusion of these terms and the restriction to a periodic domain is responsible for the formation of the Hopf bifurcation to modulation. Furthermore, the physical mechanisms responsible for the modulation in these cases are fundamentally different: for rotating detonation waves, this is the interplay of the processes contributing to the global gain dynamics. In 'galloping' detonations, the mechanism is encapsulated solely within the local frontal dynamics, including those of induction, reaction, and expansion of gases. By extension, this type of modulational instability found in RDEs is *unique* and *fundamental* to the RDE. As seen from the bifurcation diagrams of Figs. 4.6 and 4.7, for a given number of waves, to arrive at any behavior other than steady propagation, the operating point *must* first pass through this Hopf bifurcation.

4.4 Engineering Implications

Although the RDE analog system is still qualitative in nature, we can nevertheless examine metrics related to performance. In experiments, a readily observed metric is wave speed. In classical detonation theory, detonation wave speed is directly related to the heat release associated with the wave [30]. However, in the RDE, this is a misleading metric for performance. Because the detonation physics cannot be decoupled from the global gain dynamics, the measured wave speed is a property of the *system*, not only of the detonation wave front. To exemplify this, we refer to experimental studies [70] where decidedly shallow-fronted pulses exist in RDE chambers traveling at speeds comparable to the acoustic velocity of combustion products. However, if related to the Chapman-Jouguet speed of detonation for standard conditions, these speeds are of the same order. The physical difference in these scenarios is the mean combustor state. In the

RDE, the properties of the fluid ingested by the wave are significantly higher temperature and pressure than a 1-dimensional detonation propagating through standard conditions. If the upstream state of a detonation wave increases in temperature and pressure (or in the RDE analog system, an increase in u), *less* heat release is required to attain the Chapman-Jouguet condition for detonation formation [29]. Wave speed as a performance metric is therefore misleading without quantitative measurements of the fluid prior to detonation wave arrival.

An example of the interplay between wave speed and base state of the fluid in the domain is shown in Fig. 4.7. Among the different domain lengths, the peak wave speed and wave amplitudes do not coincide. In general, the fastest waves have lower base-to-peak amplitudes than that of the local maximum. Because the RDE analog system also captures parasitic deflagration, we propose an alternative metric by which one can compare the state of the system to the 'trivial' deflagration branches of Figs. 4.4, 4.6, and 4.7. This is simply the average of the square of the domain: $\overline{u^2}$. The analogous physical property is combustion chamber pressure [25].

We postulate that to form strongest detonation waves, the time scales of injection, exhaust, and the transit time of the waves should match. Significant attention has been devoted to injection and mixing within these engines, effectively shortening their associated time scales. However, decreasing this time scale *exclusively* will only lead to an increased affinity for parasitic deflagration. As an example, we refer to the premixed rotating detonation engine experiments from the United States Air Force Research Laboratory [99]. In this experimental study, during operation of the engine, stationary flames were attached to the injection sites in an extreme version of parasitic deflagration. The traveling waves propagated at a speed comparable to the acoustic speed of the combustion products of the propellant. In this scenario, it is probable that the time scales associated with combustion were far too short to match the relatively long time scale of dissipation. Perhaps the most straightforward manner in which the time scale of the exhaust processes can be shortened to match those of injection and mixing is by lifting the constraint of constant-annular area ducts. By allowing the flow to expand through an area expansion, the flow can travel, supersonically, away from the combustion zone. This is not necessarily the case for constant-area annular ducts, where a strong

pressure gradient is required to push the flow away from the combustion zone towards a mechanical or thermal choke point, increasing the residence time of a fluid particle as it travels through the RDE [100, 101].

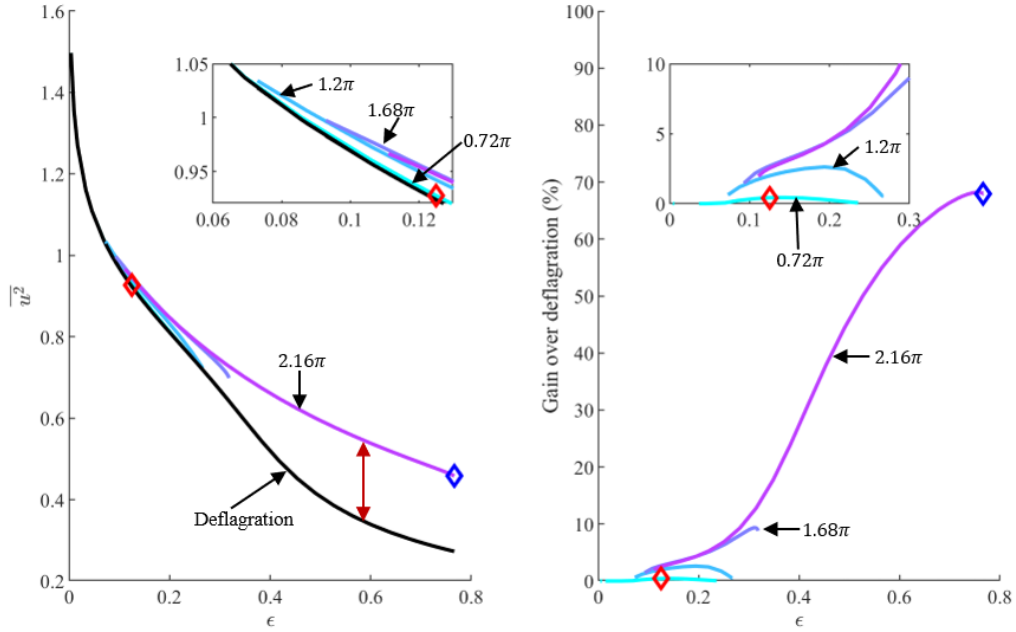

Figure 4.10: In (a), $\overline{u^2}$ is displayed for both the deflagration and single-wave solution branches for varying domain lengths as a function of the dissipation coefficient. The percent improvement over the deflagration branch (taken as the magnitude of the red arrow in (a) normalized by the value of the deflagration branch at that location) is shown in (b). In the limit of weakly dissipative rotating detonation mode, the traveling wave branches merge with the deflagration branch.

To mimic such an area constriction or expansion in the RDE analog, the loss coefficient can be modified. In Fig. 4.10, displayed are several modeled systems with parameters as listed in Table 3.1. Fixing the chemical potential of the modeled fluid ($q = 1$) and the injection sensitivity threshold ($u_p = 0.65$), the domain length and loss coefficient ϵ are varied. In (a), these single-wave branches are displayed along side the deflagration branch for the system. As the loss coefficient is reduced (corresponding to a weak pressure gradient, perhaps because of a long flowpath or the addition of a geometric choke), the traveling wave branches merge with the deflagration branch: there is no discernible difference in $\overline{u^2}$. Physically, by increasing chamber pressure, the time scale associated with the kinetics becomes increasingly small, meaning deflagration is promoted

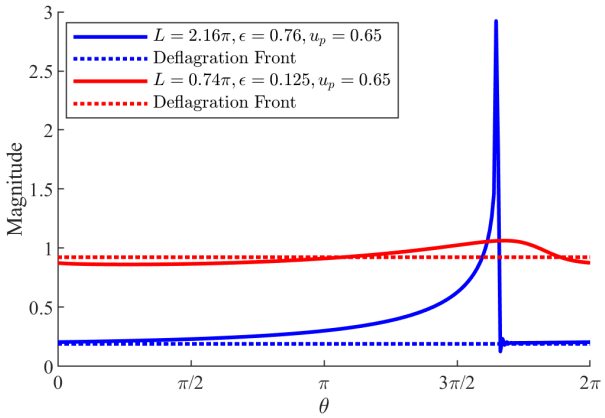

Figure 4.11: Two traveling wave profiles corresponding to the diamond markers in Fig. 4.10. In the limit of large dissipation, the detonation wave beginning and end states are exactly equal to the magnitude of the deflagration branch. Implied is a loss of mode-locking properties, since the pulse is now isolated from its environment. The displayed weak wave has a negligible difference in $\overline{u^2}$ compared to that of the associated deflagration state.

in the entirety of the domain. The percent difference of $\overline{u^2}$ between the traveling wave and deflagration branches are displayed in (b). The domain lengths ($L = 0.72\pi$ and $L = 2.16\pi$) were empirically determined to be the shortest and longest (respectively) domain lengths to support a single traveling wave for the chosen model parameters. For the shortest round-trip distance (domain length of $L = 0.782\pi$), $\overline{u^2}$ is the highest, but there is a negligible difference between it and a planar deflagration. For the longest round-trip distance (domain length of $L = 2.16\pi$), $\overline{u^2}$ can attain the lowest value of the displayed systems, but the magnitude of $\overline{u^2}$ is nearly 70% higher than that of the planar deflagration. A trade-off therefore exists: for propulsion systems, a general goal is to increase chamber pressure ($\overline{u^2}$ as presented here). However, this corresponds to *decreasing* ϵ, which in turn limits the strength of the waves, or in the extreme limit, eliminates all traveling waves. To increase dissipation corresponds to *decreasing* chamber pressure, as one might expect. To do so would create a decidedly worse-performing engine than a deflagration-based system. But curiously, the chamber pressure for the rotating detonation mode can nearly double that of the trivial deflagration mode - a significant improvement can be had for these specific conditions.

The curves associated with traveling waves in Fig. 4.10 terminate for increasing ϵ. At the terminus marks the condition where dissipation now is the dominant physical process

in the chamber - beyond this point, the wave is no longer in communication with its tail and it loses its mode-locking properties. This is shown in Fig. 4.11. The traveling wave profile for $L = 2.16\pi$ and $\epsilon = 0.76$ (corresponding to the blue diamond marker in Fig. 4.10) is plotted along with the associated planar deflagration front. The time required to dissipate the wave tail dissipates to the state of the deflagration branch is identical to the transit time of the detonation wave. To contrast the properties of this wave, a weak wave (corresponding to the red diamond marker in Fig. 4.10) is additionally plotted. The weaker wave travels at 50% of the Chapman-Jouguet speed of the system while the stronger wave travels at 78% of this benchmark speed. Although the base-to-peak amplitudes of the stronger wave is approximately 14 times greater than that of the weaker wave, their wave speeds are of the same order.

To conclude this chapter, a novel rotating detonation engine design is presented. The intent of the design is to better match the time scales of the unit processes of the RDE, with an emphasis on the dissipative processes. Recall the major findings of Chapter 2: for a RDE with a choked exit condition, the mass flux and propellant chemistry *completely define the operating profile of the combustor*. The choke point acts as a pseudo-boundary condition that backpressuizes the combustor and plenum chambers. To alleviate this constraint, proposed is a non-constant area rotating detonation engine. A section view of the concept is shown in Fig. 4.12. The pseudo-boundary condition imposed by thermally choking the flow is eliminated in this design. Because of the continuous area expansion, after attainment of a thermal choke, the flow can (radially) expand supersonically. The effects are twofold: (i) the combustor operating profile can be changed (corresponding to ϵ in Eq. 3.19), and (ii) the backpressuization of the combustor and plenum chambers is reduced. Now, should mass flux or energy content of the flow be increased, the resulting operating profile will exhibit a sonic line moving radially outward. This contrasts the behavior of long, constant-area annular ducts - the location of the sonic line remains at the duct exit, no matter the energy flux through the engine. Any increase would further backpressurize the engine and plenum chambers, eventually precluding the existence of traveling waves, as per Fig. 4.10.

The concept design of Fig. 4.12 has no net thrust as the exhaust travels radially. Similarly, building appreciable chamber pressure in such a design would be a significant

challenge. Nevertheless, the concept would provide a fantastic setting to study the properties of detonation waves in an environment in which dissipation *can* dominate.

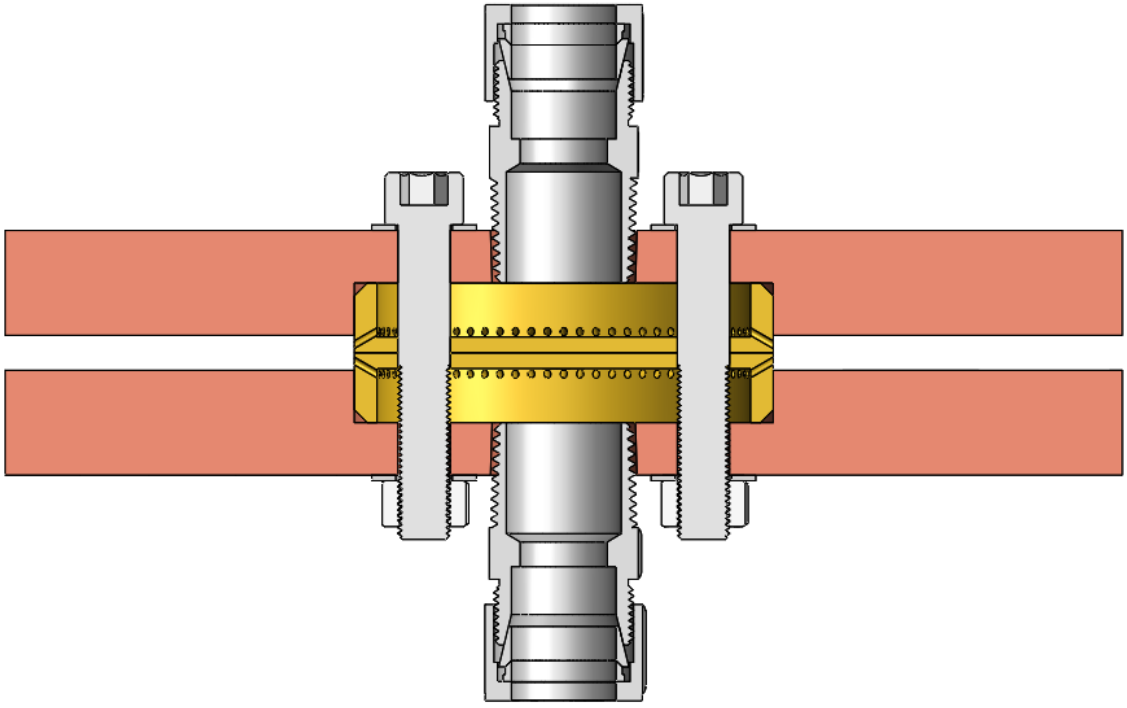

Figure 4.12: A section view of a disk-type RDE conceptual design. Fuel and oxidizer enter the separate supply lines and are injected into a disk-shaped chamber. The exhaust flow travels outward radially. The area expansion of the flowpath eliminates the restriction of developing a sonic point at the exit of the combustor.

Chapter 5

Conclusion

The rotating detonation engine is a fantastic example of the coupling and interplay of physical processes across a broad set of length and time scales. Indeed, the length scales vary from the length of the combustor (10^{-1} meters) to the thickness of a detonation wave ($< 10^{-5}$ meters). But remarkably, the physical processes occuring at these scales interact in a very clear and direct way; that is, as described by the reduced-order rotating detonation analog presented within this dissertation. The behavior of the collection of rotating detonation waves is the manifestation of the interaction of these multi-scale physics.

The waves exhibit a remarkable set of properties, including mode-locking and modulation. In examining the kinematic traces of the detonation waves, they are observed to undergo nonlinear interactions characteristic of solitons, including phase shifting and the exchanging of amplitude. However, these waves differ from the canonical solitonic structure of nonlinear wave theory in that the behavior is resultant of the *global gain dynamics*, not the *local* balance of nonlinearity and dispersion, subject to either Hamiltonian dynamics (the Kortewag-de Vries equation [102], for example) or *local* gain-loss dynamics (passively mode-locked lasers [103], for example).

Furthermore, the behavior stemming from these multi-scale physics *fundamental* to the rotating detonation engine. As a result of the competing physical processes, the steadily propagating pulse train can undergo a Hopf bifurcation to time-periodic modulation - this

bifurcation to modulation is termed the *fundamental instability* of rotating detonation waves, as this is the bifurcation from which transient phenomena originate.

Bibliography

[1] L. He and J. H. S. Lee, "The dynamical limit of one-dimensional detonations," *Physics of Fluids*, vol. 7, pp. 1151–1158, May 1995.

[2] A. R. Kasimov and D. S. Stewart, "On the dynamics of self-sustained one-dimensional detonations: A numerical study in the shock-attached frame," *Physics of Fluids*, vol. 16, pp. 3566–3578, Oct. 2004.

[3] S. P. Borisov and A. N. Kudryavtsev, "Numerical simulation of nonlinear dynamics of 1d pulsating detonations," *Journal of Physics: Conference Series*, vol. 894, p. 012013, Oct. 2017.

[4] A. P. Dowling, "A kinematic model of a ducted flame," *Journal of Fluid Mechanics*, vol. 394, pp. 51–72, Sep. 1999.

[5] F. Chacon and M. Gamba, "Detonation wave dynamics in a rotating detonation engine," in *AIAA Scitech 2019 Forum*, American Institute of Aeronautics and Astronautics, Jan. 2019.

[6] M. Bohon, R. Bluemner, C. Paschereit, and E. Gutmark, "High-speed imaging of wave modes in an RDC," *Experimental Thermal and Fluid Science*, vol. 102, pp. 28–37, Apr. 2019.

[7] R. D. Smith and S. Stanley, "Experimental investigation of continuous detonation rocket engines for in-space propulsion," in *52nd AIAA/SAE/ASEE Joint Propulsion Conference*, American Institute of Aeronautics and Astronautics, Jul. 2016.

[8] D. Schwer and K. Kailasanath, "Numerical investigation of rotating detonation

engines," in *46th AIAA Joint Propulsion Conference*, American Institute of Aeronautics and Astronautics, Jul. 2010.

[9] C. Lietz, Y. Desai, W. A. Hargus, and V. Sankaran, "Parametric investigation of rotating detonation rocket engines using large eddy simulations," in *AIAA Propulsion and Energy 2019 Forum*, American Institute of Aeronautics and Astronautics, Aug. 2019.

[10] D. E. Paxson and D. A. Schwer, "Operational stability limits in rotating detonation engine numerical simulations," in *AIAAScitech 2019 Forum*, American Institute of Aeronautics and Astronautics, Jan. 2019.

[11] M. O. Gani and T. Ogawa, "Instability of periodic traveling wave solutions in a modified FitzHugh–nagumo model for excitable media," *Applied Mathematics and Computation*, vol. 256, pp. 968–984, Apr. 2015.

[12] F. Li, P. K. A. Wai, and J. N. Kutz, "Geometrical description of the onset of multi-pulsing in mode-locked laser cavities," *Journal of the Optical Society of America B*, vol. 27, p. 2068, Sep. 2010.

[13] A. G. Merzhanov and E. N. Rumanov, "Physics of reaction waves," *Reviews of Modern Physics*, vol. 71, pp. 1173–1211, Jul. 1999.

[14] J. P. Keener and J. J. Tyson, "Spiral waves in the belousov-zhabotinskii reaction," *Physica D: Nonlinear Phenomena*, vol. 21, pp. 307–324, Sep. 1986.

[15] I. R. Epstein, "Predicting complex biology with simple chemistry," *Proceedings of the National Academy of Sciences*, vol. 103, pp. 15727–15728, Oct. 2006.

[16] M. I. Radulescu and J. Tang, "Nonlinear dynamics of self-sustained supersonic reaction waves: Fickett's detonation analogue," *Physical Review Letters*, vol. 107, Oct. 2011.

[17] L. Crocco, D. T. Harrje, and F. H. Reardon, "Transverse combustion instability in liquid propellant rocket motors," *ARS Journal*, vol. 32, pp. 366–373, Mar. 1962.

[18] R. M. Clayton, R. S. Rogero, and J. G. Sotter, "An experimental description

of destructive liquid rocket resonant combustion.," *AIAA Journal*, vol. 6, pp. 1252–1259, Jul. 1968.

[19] B. T. Zinn, "A theoretical study of nonlinear combustion instability in liquid-propellant rocket engines.," *AIAA Journal*, vol. 6, pp. 1966–1972, Oct. 1968.

[20] B. T. Zinn and E. A. Powell, "Nonlinear combustion instability in liquid-propellant rocket engines," *Symposium (International) on Combustion*, vol. 13, pp. 491–503, Jan. 1971.

[21] W. E. Anderson and V. Yang, eds., *Liquid Rocket Engine Combustion Instability*. American Institute of Aeronautics and Astronautics, Jan. 1995.

[22] J. C. Oefelein and V. Yang, "Comprehensive review of liquid-propellant combustion instabilities in f-1 engines," *Journal of Propulsion and Power*, vol. 9, pp. 657–677, Sep. 1993.

[23] B. Voitsekhovsky, "Stazionarnaia detonatsia (maintained detonation)," *Doklady Akad. Nauk SSSR*, 1960.

[24] J. A. Nicholls, R. E. Cullen, and K. W. Ragland, "Feasibility studies of a rotating detonation wave rocket motor.," *Journal of Spacecraft and Rockets*, vol. 3, pp. 893–898, Jun. 1966.

[25] J. Koch, M. Kurosaka, C. Knowlen, and J. N. Kutz, "Mode-locked rotating detonation waves: Experiments and a model equation," *Physical Review E*, vol. 101, Jan. 2020.

[26] V. Anand and E. Gutmark, "Rotating detonation combustors and their similarities to rocket instabilities," *Progress in Energy and Combustion Science*, vol. 73, pp. 182–234, Jul. 2019.

[27] J. W. Bennewitz, B. R. Bigler, J. J. Pilgram, and W. A. Hargus, "Modal transitions in rotating detonation rocket engines," *International Journal of Energetic Materials and Chemical Propulsion*, vol. 18, no. 2, pp. 91–109, 2019.

[28] A. S. George, R. Driscoll, V. Anand, and E. Gutmark, "On the existence and

multiplicity of rotating detonations," *Proceedings of the Combustion Institute*, vol. 36, no. 2, pp. 2691–2698, 2017.

[29] C. K. Law, *Combustion Physics*. Cambridge University Press, 2006.

[30] D. L. Chapman, "VI. on the rate of explosion in gases," *The London, Edinburgh, and Dublin Philosophical Magazine and Journal of Science*, vol. 47, pp. 90–104, Jan. 1899.

[31] J. J. Erpenbeck, "Stability of idealized one-reaction detonations," *Physics of Fluids*, vol. 7, no. 5, p. 684, 1964.

[32] H. D. Ng, M. I. Radulescu, A. J. Higgins, N. Nikiforakis, and J. H. S. Lee, "Numerical investigation of the instability for one-dimensional chapman–jouguet detonations with chain-branching kinetics," *Combustion Theory and Modelling*, vol. 9, pp. 385–401, Aug. 2005.

[33] L. M. Faria, A. R. Kasimov, and R. R. Rosales, "Theory of weakly nonlinear self-sustained detonations," *Journal of Fluid Mechanics*, vol. 784, pp. 163–198, Nov. 2015.

[34] D. Bull, J. Elsworth, P. Shuff, and E. Metcalfe, "Detonation cell structures in fuel/air mixtures," *Combustion and Flame*, vol. 45, pp. 7–22, Jan. 1982.

[35] J. Von Neumann, "Theory of detonation waves," tech. rep., Institute for Advanced Study, Princeton University, 1942.

[36] L. F. D. Silva and B. Deshaies, "Stabilization of an oblique detonation wave by a wedge: a parametric numerical study," *Combustion and Flame*, vol. 121, pp. 152–166, Apr. 2000.

[37] P. A. Urtiew, "Experimental observations of the transition to detonation in an explosive gas," *Proceedings of the Royal Society of London. Series A. Mathematical and Physical Sciences*, vol. 295, pp. 13–28, Nov. 1966.

[38] B. V. Voitsekhovskii, V. V. Mitrofanov, and M. E. Topchiyan, "Structure of the detonation front in gases (survey)," *Combustion, Explosion, and Shock Waves*, vol. 5, pp. 267–273, Jul. 1969.

[39] J. J. Erpenbeck, "Theory of detonation stability," *Symposium (International) on Combustion*, vol. 12, pp. 711–721, Jan. 1969.

[40] H. I. Lee and D. S. Stewart, "Calculation of linear detonation instability: one-dimensional instability of plane detonation," *Journal of Fluid Mechanics*, vol. 216, p. 103, Jul. 1990.

[41] W. Fickett and W. Davis, *Detonation: Theory and Experiment*. Dover Publications, 1979.

[42] G. Sharpe, "Linear stability of pathological detonations," *Journal of Fluid Mechanics*, vol. 401, pp. 311–338, Dec. 1999.

[43] K. Schadow and E. Gutmark, "Combustion instability related to vortex shedding in dump combustors and their passive control," *Progress in Energy and Combustion Science*, vol. 18, pp. 117–132, Jan. 1992.

[44] K. C. Schadow, E. Gutmark, T. P. Parr, D. M. Parr, K. J. Wilson, and J. E. Crump, "Large-scale coherent structures as drivers of combustion instability," *Combustion Science and Technology*, vol. 64, pp. 167–186, Apr. 1989.

[45] T. Lieuwen and Y. Neumeier, "Nonlinear pressure-heat release transfer function measurements in a premixed combustor," *Proceedings of the Combustion Institute*, vol. 29, pp. 99–105, Jan. 2002.

[46] D. Paxson, "A sectored-one-dimensional model for simulating combustion instabilities in premix combustbrs," in *38th Aerospace Sciences Meeting and Exhibit*, 1999.

[47] J. M. Cohen, B. E. Wake, and D. Choi, "Investigation of instabilities in a lean, premixed step combustor," *Journal of Propulsion and Power*, vol. 19, pp. 81–88, Jan. 2003.

[48] M. Summerfield, "A theory of unstable combustion in liquid propellant rocket systems," *Journal of the American Rocket Society*, vol. 21, pp. 108–114, Sep. 1951.

[49] L. Crocco and S.-I. Cheng, "Theory of combustion instability in liquid propellant rocket motors," tech. rep., Princeton University, 1956.

[50] T. Bussing and G. Pappas, "An introduction to pulse detonation engines," in *32nd Aerospace Sciences Meeting and Exhibit*, American Institute of Aeronautics and Astronautics, Jan. 1994.

[51] M. Fotia, J. Hoke, and F. Schauer, "Propellant plenum dynamics in a two-dimensional rotating detonation experiment," in *52nd Aerospace Sciences Meeting*, American Institute of Aeronautics and Astronautics, Jan. 2014.

[52] M. Fotia, T. A. Kaemming, J. Hoke, and F. Schauer, "Study of the experimental performance of a rotating detonation engine with nozzled exhaust flow," in *53rd AIAA Aerospace Sciences Meeting*, American Institute of Aeronautics and Astronautics, Jan. 2015.

[53] V. Anand, A. S. George, R. Driscoll, and E. Gutmark, "Analysis of air inlet and fuel plenum behavior in a rotating detonation combustor," *Experimental Thermal and Fluid Science*, vol. 70, pp. 408–416, Jan. 2016.

[54] D. Schwer and K. Kailasanath, "Feedback into mixture plenums in rotating detonation engines," in *50th AIAA Aerospace Sciences Meeting including the New Horizons Forum and Aerospace Exposition*, American Institute of Aeronautics and Astronautics, Jan. 2012.

[55] D. Schwer, A. Corrigan, B. Taylor, and K. Kailasanath, "On reducing feedback pressure in rotating detonation engines," in *51st AIAA Aerospace Sciences Meeting including the New Horizons Forum and Aerospace Exposition*, American Institute of Aeronautics and Astronautics, Jan. 2013.

[56] V. Anand, A. S. George, R. Driscoll, and E. Gutmark, "Characterization of instabilities in a rotating detonation combustor," *International Journal of Hydrogen Energy*, vol. 40, pp. 16649–16659, Dec. 2015.

[57] V. Anand and E. Gutmark, "Types of low frequency instabilities in rotating detonation combustors," in *Notes on Numerical Fluid Mechanics and Multidisciplinary Design*, pp. 197–213, Springer International Publishing, Aug. 2018.

[58] D. E. Paxson, "Numerical analysis of a rotating detonation engine in the relative

reference frame," in *52nd Aerospace Sciences Meeting*, American Institute of Aeronautics and Astronautics, Jan. 2014.

[59] D. Schwer and K. Kailasanath, "Numerical investigation of the physics of rotating-detonation-engines," *Proceedings of the Combustion Institute*, vol. 33, pp. 2195–2202, Jan. 2011.

[60] J. Humble, S. V. Sardeshmukh, and S. D. Heister, "Reduced order modeling of rotational detonation engines," in *AIAA Scitech 2019 Forum*, American Institute of Aeronautics and Astronautics, Jan. 2019.

[61] R. T. Fievisohn and K. H. Yu, "Steady-state analysis of rotating detonation engine flowfields with the method of characteristics," *Journal of Propulsion and Power*, vol. 33, pp. 89–99, Jan. 2017.

[62] R. Kawashima, I. Funaki, J. Fujii, A. Matsuo, K. Ishihara, and J. Kasahara, "A quasi-one-dimensional analytic model of rotating detonation combustors," 2017.

[63] J. Heath, "Generating detonation waves in an annulus via phased adiabatic shocks," Master's thesis, University of Washington, 2015.

[64] J. Boening, "Initiation of orderly spinning detonation waves via phased sparking," Master's thesis, University of Washington, 2016.

[65] J. A. Boening, E. A. Wheeler, J. D. Heath, J. V. Koch, A. T. Mattick, R. E. Breidenthal, C. Knowlen, and M. Kurosaka, "Rotating detonation engine using a wave generator and controlled mixing," *Journal of Propulsion and Power*, pp. 1–12, Aug. 2018.

[66] J. W. Bennewitz, B. R. Bigler, W. A. Hargus, S. A. Danczyk, and R. D. Smith, "Characterization of detonation wave propagation in a rotating detonation rocket engine using direct high-speed imaging," in *2018 Joint Propulsion Conference*, American Institute of Aeronautics and Astronautics, Jul. 2018.

[67] M. Washington, "Radial injector mixing effects on detonation zone position in rotating detonation engine," Master's thesis, University of Washington, 2019.

[68] P. M. Stocker, "The transients arising from the addition of heat to a gas flow,"

Mathematical Proceedings of the Cambridge Philosophical Society, vol. 48, p. 482, Jul. 1952.

[69] M. Fotia, T. A. Kaemming, J. R. Codoni, J. Hoke, and F. Schauer, "Experimental thrust sensitivity of a rotating detonation engine to various aerospike plug-nozzle configurations," in *AIAA Scitech 2019 Forum*, American Institute of Aeronautics and Astronautics, Jan. 2019.

[70] J. Koch, L. Chang, C. Upadhye, K. Chau, M. Kurosaka, and C. Knowlen, "Influence of injector-to-annulus area ratio on rotating detonation engine operability," in *AIAA Propulsion and Energy 2019 Forum*, American Institute of Aeronautics and Astronautics, Aug. 2019.

[71] A. Majda, "A qualitative model for dynamic combustion," *SIAM Journal on Applied Mathematics*, vol. 41, pp. 70–93, Aug. 1981.

[72] E. M. de Jager, "On the origin of the Korteweg-de Vries equation,"

[73] P. J. Olver, "Evolution equations possessing infinitely many symmetries," *Journal of Mathematical Physics*, vol. 18, pp. 1212–1215, Jun. 1977.

[74] N. Akhmediev and A. Ankiewicz, eds., *Dissipative Solitons: From Optics to Biology and Medicine*. Springer Berlin Heidelberg, 2008.

[75] R. FitzHugh, "Mathematical models of threshold phenomena in the nerve membrane," *The Bulletin of Mathematical Biophysics*, vol. 17, pp. 257–278, Dec. 1955.

[76] D. Horn and I. Opher, "Solitary waves of integrate-and-fire neural fields," *Neural Computation*, vol. 9, pp. 1677–1690, Nov. 1997.

[77] A. N. Burkitt, "A review of the integrate-and-fire neuron model: I. homogeneous synaptic input," *Biological Cybernetics*, vol. 95, pp. 1–19, Apr. 2006.

[78] J. N. Kutz, "Mode-locked soliton lasers," *SIAM Review*, vol. 48, pp. 629–678, Jan. 2006.

[79] B. G. Bale, K. Kieu, J. N. Kutz, and F. Wise, "Transition dynamics for multi-pulsing in mode-locked lasers," *Optics Express*, vol. 17, p. 23137, Dec. 2009.

[80] F. A. Bykovskii, S. A. Zhdan, and E. F. Vedernikov, "Continuous spin detonations," *Journal of Propulsion and Power*, vol. 22, pp. 1204–1216, Nov. 2006.

[81] D. A. Frank-Kamenetskii, "Towards temperature distributions in a reaction vessel and the stationary theory of thermal explosion," *Doklady Akademii Nauk SSSR*, 1938.

[82] D. Frank-Kamenetskii and N. Thon, *Diffusion and Heat Exchange in Chemical Kinetics*. Princeton University Press, 1955.

[83] R. LITCHFORD, "Comment on tangential wave motion in unstable combustors," in *29th Joint Propulsion Conference and Exhibit*, American Institute of Aeronautics and Astronautics, Jun. 1993.

[84] A. Kasimov, "Detonation analogs revisited," in *25th ICDERS*, 2015.

[85] W. Fickett, "Detonation in miniature," *American Journal of Physics*, vol. 47, pp. 1050–1059, Dec. 1979.

[86] G. Lyng and K. Zumbrun, "A stability index for detonation waves in majda's model for reacting flow," *Physica D: Nonlinear Phenomena*, vol. 194, pp. 1–29, Jul. 2004.

[87] S. Jung and J. Yao, "Stability of ZND detonations for majda's model," *Quarterly of Applied Mathematics*, vol. 70, pp. 69–76, Jan. 2012.

[88] J. Humpherys, G. Lyng, and K. Zumbrun, "Stability of viscous detonations for majda's model," *Physica D: Nonlinear Phenomena*, vol. 259, pp. 63–80, Sep. 2013.

[89] L. M. Faria and A. R. Kasimov, "Qualitative modeling of the dynamics of detonations with losses," *Proceedings of the Combustion Institute*, vol. 35, no. 2, pp. 2015–2023, 2015.

[90] X. Mi and A. J. Higgins, "Influence of discrete sources on detonation propagation in a burgers equation analog system," *Physical Review E*, vol. 91, May 2015.

[91] D. I. Ketcheson, K. Mandli, A. J. Ahmadia, A. Alghamdi, M. Q. de Luna, M. Parsani, M. G. Knepley, and M. Emmett, "PyClaw: Accessible, extensible, scalable tools for wave propagation problems," *SIAM Journal on Scientific Computing*, vol. 34, pp. C210–C231, Jan. 2012.

[92] C. Christov and M. Velarde, "Dissipative solitons," *Physica D: Nonlinear Phenomena*, vol. 86, pp. 323–347, Sep. 1995.

[93] H.-G. Purwins, H. Bödeker, and S. Amiranashvili, "Dissipative solitons," *Advances in Physics*, vol. 59, pp. 485–701, Sep. 2010.

[94] H. Uecker, D. Wetzel, and J. Rademacher, "pde2path - a matlab package for continuation and bifurcation in 2d elliptic systems," *Numerical Mathematics: Theory, Methods, and Applications*, 2015.

[95] H. Uecker, "User guide on hopf bifurcation and time periodic orbits with pde2path," 2019.

[96] P. Wolanski, "Rotating detonation wave stability," in *23rd ICDERS*, 2011.

[97] P. Wolański, "Detonative propulsion," *Proceedings of the Combustion Institute*, vol. 34, pp. 125–158, Jan. 2013.

[98] A. K. Henrick, T. D. Aslam, and J. M. Powers, "Simulations of pulsating one-dimensional detonations with true fifth order accuracy," *Journal of Computational Physics*, vol. 213, pp. 311–329, Mar. 2006.

[99] I. Q. Andrus, P. King, M. D. Polanka, F. Schauer, and J. Hoke, "Experimentation of a premixed rotating detonation engine utilizing a variable slot feed plenum," in *54th AIAA Aerospace Sciences Meeting*, American Institute of Aeronautics and Astronautics, Jan. 2016.

[100] M. L. Fotia, F. Schauer, T. Kaemming, and J. Hoke, "Experimental study of the performance of a rotating detonation engine with nozzle," *Journal of Propulsion and Power*, vol. 32, pp. 674–681, May 2016.

[101] J. Koch, M. R. Washington, M. Kurosaka, and C. Knowlen, "Operating characteristics of a CH4/o2 rotating detonation engine in a backpressure controlled facility," in *AIAA Scitech 2019 Forum*, American Institute of Aeronautics and Astronautics, Jan. 2019.

[102] C. S. Gardner, "Korteweg-de Vries equation and generalizations. IV. the

Korteweg-de Vries equation as a Hamiltonian system," *Journal of Mathematical Physics*, vol. 12, pp. 1548–1551, Aug. 1971.

[103] P. Grelu and N. Akhmediev, "Dissipative solitons for mode-locked lasers," *Nature Photonics*, vol. 6, pp. 84–92, Feb. 2012.

Appendix A

Drawings

A.1 76mm Engine

The 76mm-RDE was designed to undergo several significant machining and fabrication steps. The first of these (not shown) is the welding of the front and rear flanges to the containment cylinder. The post-weld assembly is shown here with all pertinent features. Materials and tolerances are as noted.

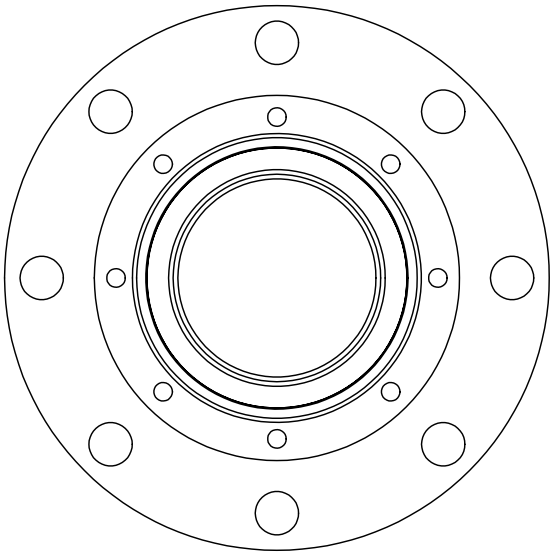

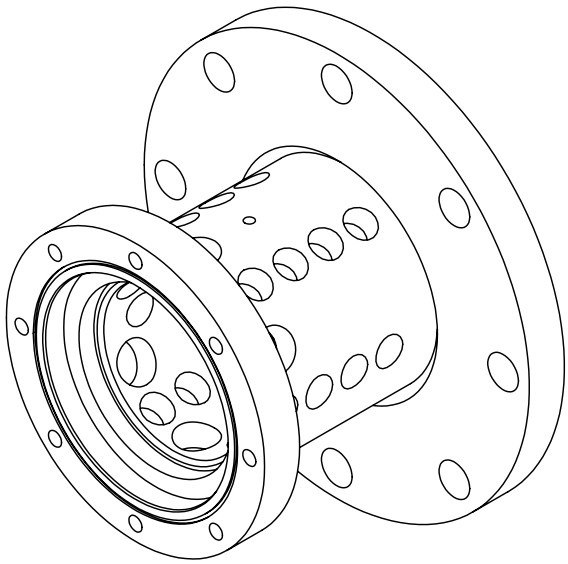

		UNLESS OTHERWISE SPECIFIED:		NAME	DATE
		DIMENSIONS ARE IN INCHES BREAK ALL SHARP CORNERS TOLERANCES: ANGULAR: ± 1DEG TWO PLACE DECIMAL ± 0.01" THREE PLACE DECIMAL ± 0.005"	DRAWN	JVK	10/22/18
			CHECKED		
			ENG APPR.		
			MFG APPR.		
		INTERPRET GEOMETRIC TOLERANCING PER:	Q.A.		
		MATERIAL SS304L	COMMENTS:		
NEXT ASSY	USED ON	FINISH			
APPLICATION		DO NOT SCALE DRAWING			

ROTATING DETONATION ENGINE

TITLE:

Post-weld Assembly

SIZE	DWG. NO.	REV
A	205	01

SCALE: 1:3 | WEIGHT: | SHEET 1 OF 3

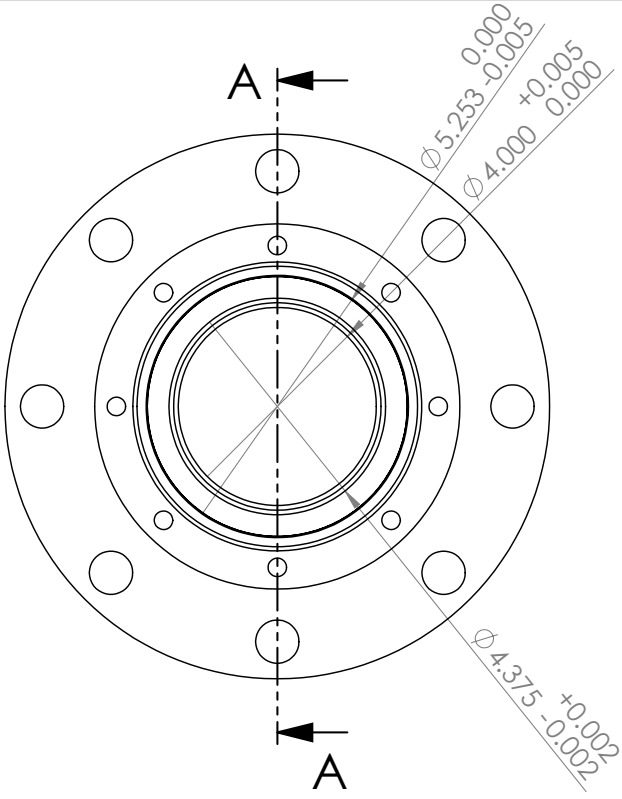

SECTION A-A

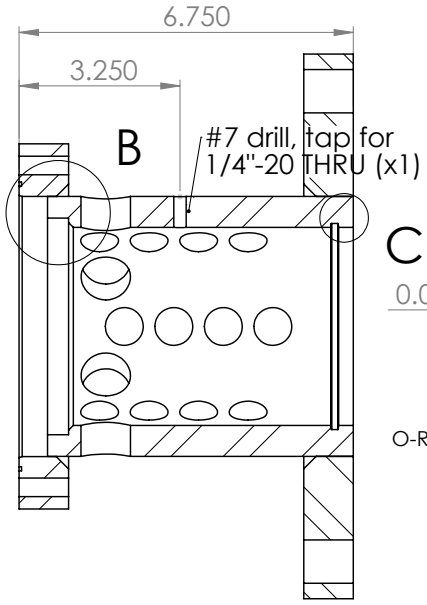

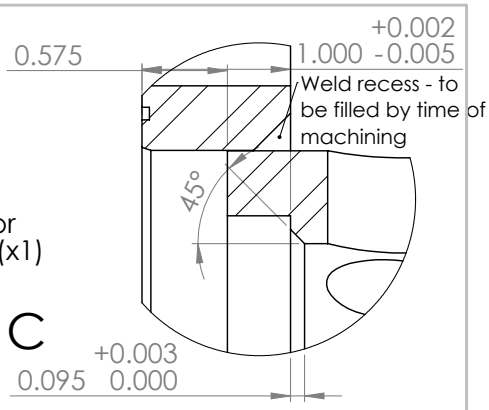

DETAIL B

SCALE 1 : 1

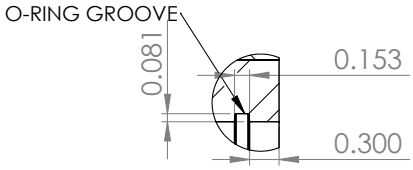

DETAIL C

SCALE 2 : 3

Dimensions not labeled remain in post-welded state.

NEXT ASSY	USED ON	
APPLICATION		

UNLESS OTHERWISE SPECIFIED:

DIMENSIONS ARE IN INCHES
BREAK ALL SHARP CORNERS
TOLERANCES:
ANGULAR: ± 1deg
TWO PLACE DECIMAL ± 0.01"
THREE PLACE DECIMAL ± 0.005"

INTERPRET GEOMETRIC TOLERANCING PER:

MATERIAL: SS304L

FINISH

DO NOT SCALE DRAWING

	NAME	DATE
DRAWN	JVK	10/22/18
CHECKED		
ENG APPR.		
MFG APPR.		
Q.A.		

COMMENTS:

ROTATING DETONATION ENGINE

TITLE:

Post-weld Assembly

SIZE	DWG. NO.	REV
A	205	01

SCALE: 1:3 | WEIGHT: | SHEET 2 OF 3

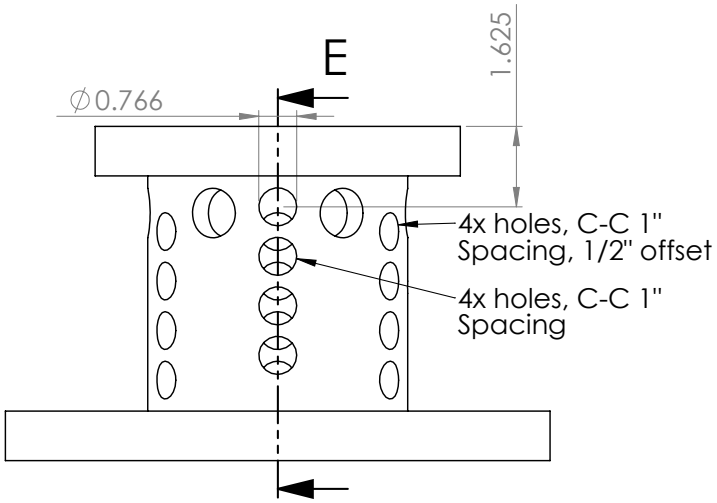

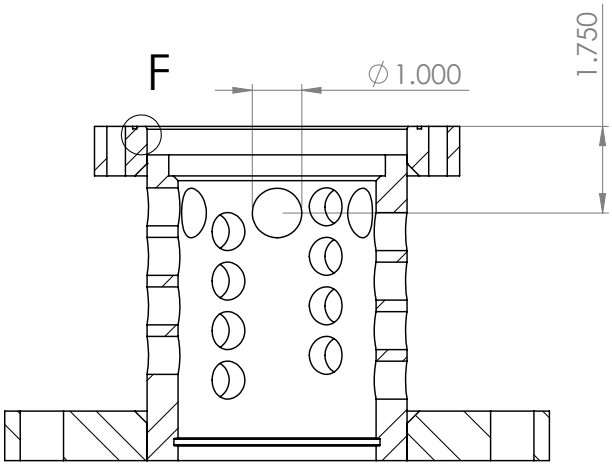

SECTION E-E

Instrumentation ports every 60deg. Spark plug ports (x6, or every 60deg) between (15deg offset) instrument port columns.

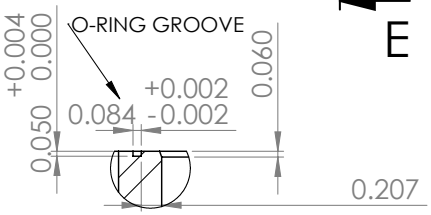

DETAIL F

SCALE 2 : 3

		UNLESS OTHERWISE SPECIFIED:		NAME	DATE
		DIMENSIONS ARE IN INCHES BREAK ALL SHARP CORNERS TOLERANCES: ANGULAR: ± 1deg TWO PLACE DECIMAL ± 0.01" THREE PLACE DECIMAL ± 0.005"	DRAWN	JVK	10/22/18
			CHECKED		
			ENG APPR.		
			MFG APPR.		
		INTERPRET GEOMETRIC TOLERANCING PER:	Q.A.		
		MATERIAL SS304L	COMMENTS:		
NEXT ASSY	USED ON	FINISH			
APPLICATION		DO NOT SCALE DRAWING			

ROTATING DETONATION ENGINE

TITLE:

Post-weld Assembly

SIZE	DWG. NO.	REV
A	205	01

SCALE: 1:3	WEIGHT:	SHEET 3 OF 3

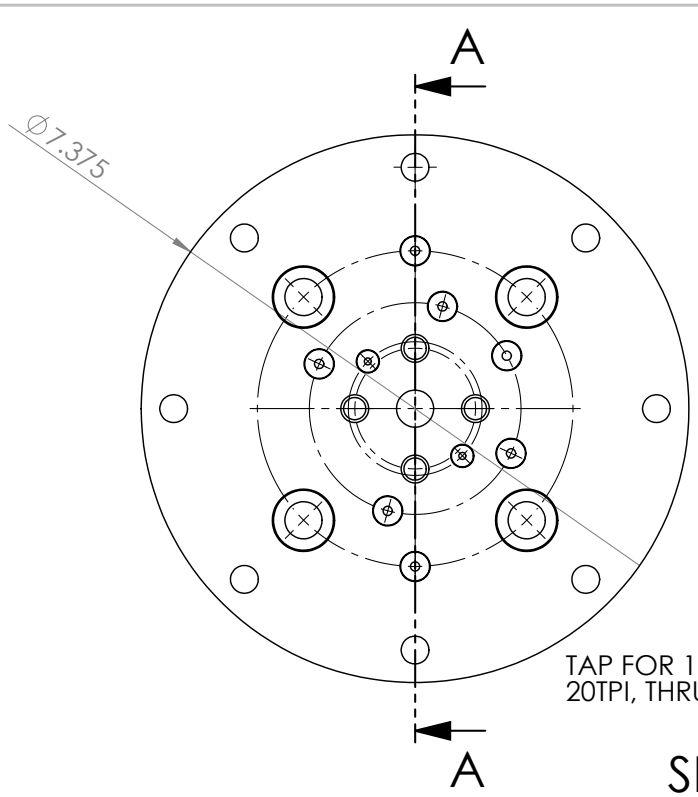

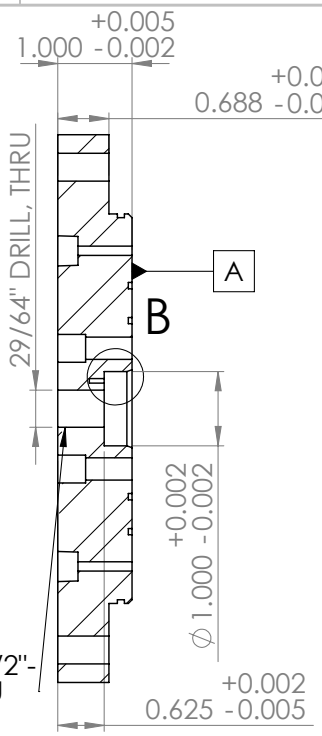

SECTION A-A

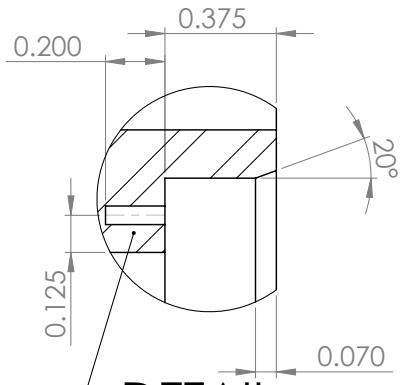

DETAIL B

SCALE 2 : 1

Hole for 1/16"
dia x 0.25"
long locating
dowel pin

		UNLESS OTHERWISE SPECIFIED:		NAME	DATE	ROTATING DETONATION ENGINE
		DIMENSIONS ARE IN INCHES BREAK ALL CORNERS TOLERANCES: ANGULAR: ± 1deg TWO PLACE DECIMAL ± 0.01" THREE PLACE DECIMAL ± 0.005"	DRAWN	JVK	10/22/18	TITLE: Front Plate
			CHECKED			
			ENG APPR.			
			MFG APPR.			
		INTERPRET GEOMETRIC TOLERANCING PER:	Q.A.			
		MATERIAL: SS304L	COMMENTS:			SIZE: A / DWG. NO.: 206 / REV: 01
NEXT ASSY	USED ON	FINISH				
APPLICATION		DO NOT SCALE DRAWING				SCALE: 1:2 / WEIGHT: / SHEET 1 OF 5

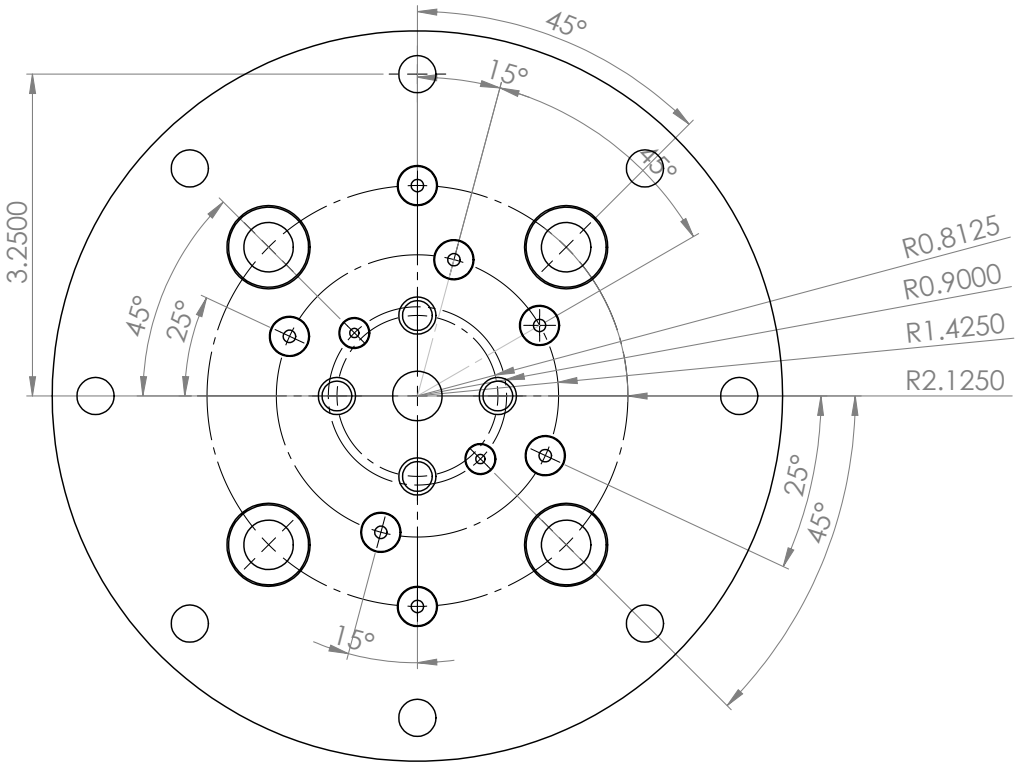

		UNLESS OTHERWISE SPECIFIED:		NAME	DATE
		DIMENSIONS ARE IN INCHES BREAK ALL SHARP CORNERS TOLERANCES: ANGULAR: ± 1deg TWO PLACE DECIMAL ± 0.01" THREE PLACE DECIMAL ± 0.005"	DRAWN	JVK	10/22/18
			CHECKED		
			ENG APPR.		
			MFG APPR.		
		INTERPRET GEOMETRIC TOLERANCING PER:	Q.A.		
		MATERIAL SS304L	COMMENTS:		
NEXT ASSY	USED ON	FINISH			
APPLICATION		DO NOT SCALE DRAWING			

ROTATING DETONATION ENGINE

TITLE:

Front Plate

SIZE	DWG. NO.	REV
A	206	01

SCALE: 1:1.5 WEIGHT: SHEET 2 OF 5

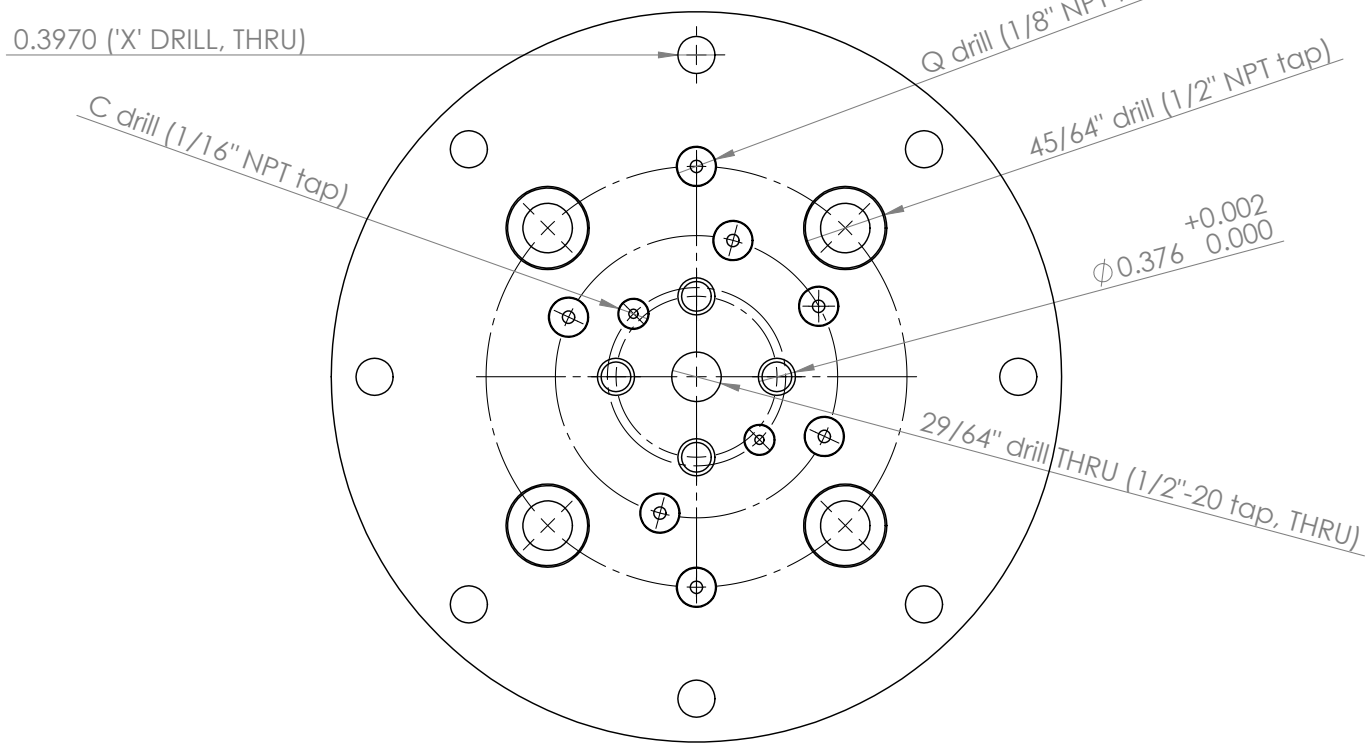

		UNLESS OTHERWISE SPECIFIED:		NAME	DATE
		DIMENSIONS ARE IN INCHES BREAK ALL SHARP CORNERS TOLERANCES: ANGULAR: ± 1deg TWO PLACE DECIMAL ± 0.01" THREE PLACE DECIMAL ± 0.005"	DRAWN	JVK	10/22/18
			CHECKED		
			ENG APPR.		
			MFG APPR.		
		INTERPRET GEOMETRIC TOLERANCING PER:	Q.A.		
		MATERIAL SS304L	COMMENTS:		
NEXT ASSY	USED ON	FINISH			
APPLICATION		DO NOT SCALE DRAWING			

ROTATING DETONATION ENGINE

TITLE:

Front Plate

SIZE	DWG. NO.	REV
A	206	01

SCALE: 1:1.5 WEIGHT: SHEET 3 OF 5

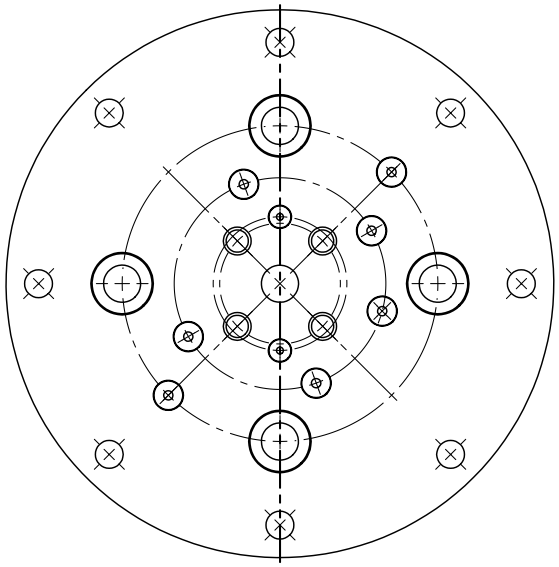

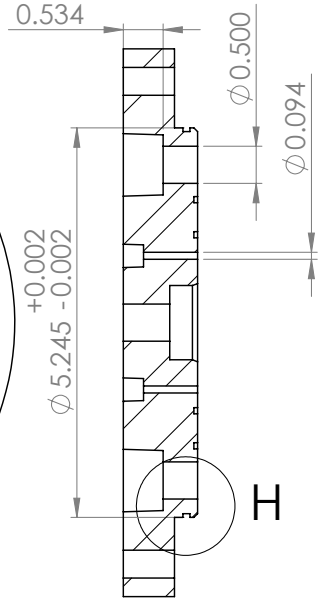

SECTION D-D

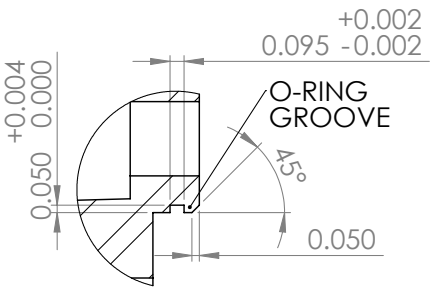

DETAIL H

SCALE 1 : 1

		UNLESS OTHERWISE SPECIFIED:		NAME	DATE
		DIMENSIONS ARE IN INCHES BREAK ALL SHARP CORNERS TOLERANCES: ANGULAR: ± 1deg TWO PLACE DECIMAL ± 0.01" THREE PLACE DECIMAL ± 0.005"	DRAWN	JVK	10/22/18
			CHECKED		
			ENG APPR.		
			MFG APPR.		
		INTERPRET GEOMETRIC TOLERANCING PER:	Q.A.		
		MATERIAL SS304L	COMMENTS:		
NEXT ASSY	USED ON	FINISH			
APPLICATION		DO NOT SCALE DRAWING			

ROTATING DETONATION ENGINE

TITLE:

Front Plate

SIZE	DWG. NO.	REV
A	206	01
SCALE: 1:2	WEIGHT:	SHEET 4 OF 5

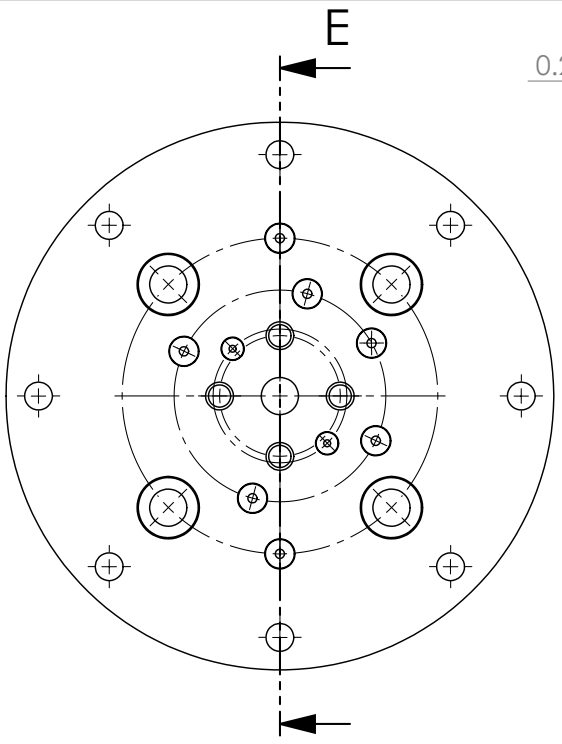

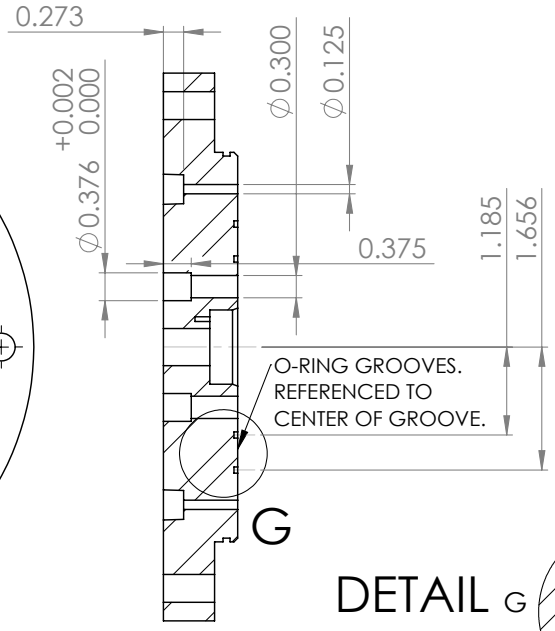

SECTION E-E

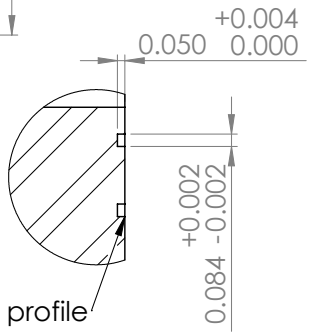

DETAIL G

SCALE 1 : 1

		UNLESS OTHERWISE SPECIFIED:		NAME	DATE
		DIMENSIONS ARE IN INCHES BREAK ALL SHARP CORNERS TOLERANCES: ANGULAR: ± 1deg TWO PLACE DECIMAL ± 0.01" THREE PLACE DECIMAL ± 0.005"	DRAWN	JVK	10/22/18
			CHECKED		
			ENG APPR.		
			MFG APPR.		
		INTERPRET GEOMETRIC TOLERANCING PER:	Q.A.		
		MATERIAL SS304L	COMMENTS:		
NEXT ASSY	USED ON	FINISH			
APPLICATION		DO NOT SCALE DRAWING			

ROTATING DETONATION ENGINE

TITLE:

Front Plate

SIZE	DWG. NO.	REV
A	206	01
SCALE: 1:2	WEIGHT:	SHEET 5 OF 5

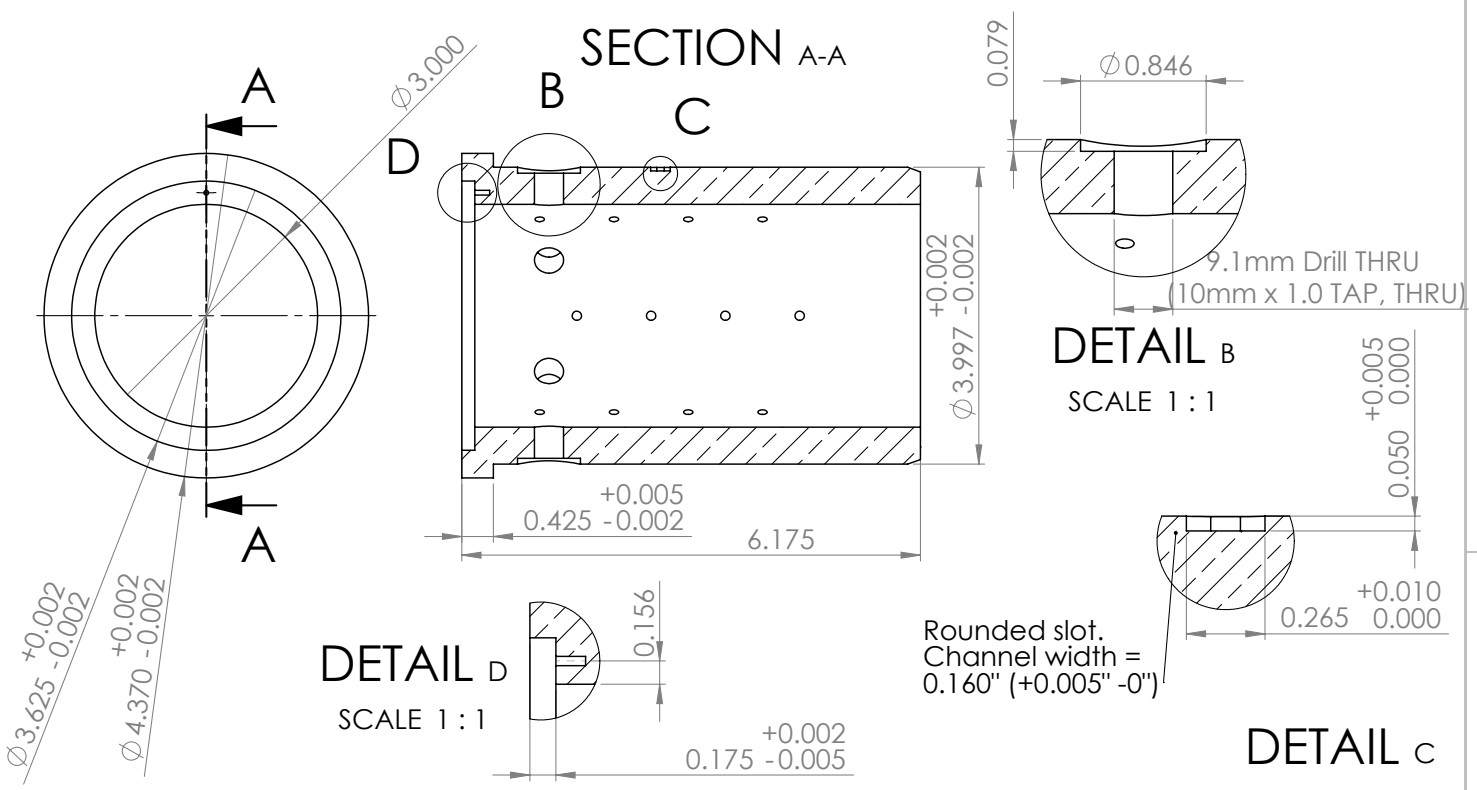

		UNLESS OTHERWISE SPECIFIED:		NAME	DATE	ROTATING DETONATION ENGINE
		DIMENSIONS ARE IN INCHES BREAK ALL SHARP CORNERS TOLERANCES: ANGULAR: ± 1deg TWO PLACE DECIMAL ± 0.01" THREE PLACE DECIMAL ± 0.005"	DRAWN	JVK	10/22/18	TITLE: Sleeve
			CHECKED			
			ENG APPR.			
			MFG APPR.			
		INTERPRET GEOMETRIC TOLERANCING PER:	Q.A.			
		MATERIAL C10100 - OFHC	COMMENTS:			SIZE A | DWG. NO. 207 | REV 01
NEXT ASSY	USED ON	FINISH				
APPLICATION		DO NOT SCALE DRAWING				SCALE: 1:2 | WEIGHT: | SHEET 1 OF 2

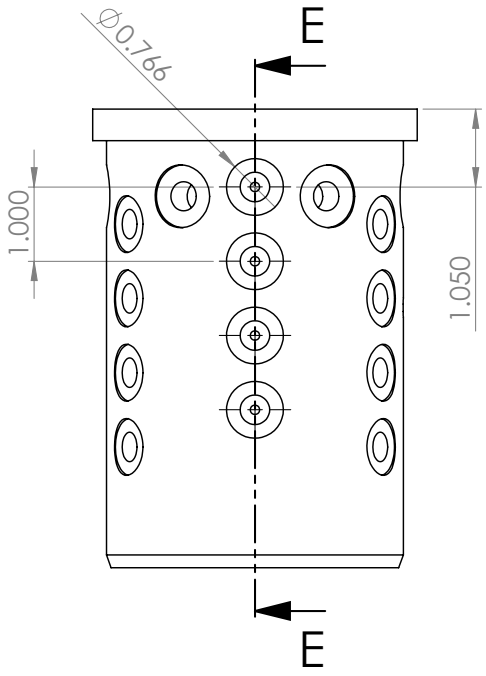

SECTION E-E

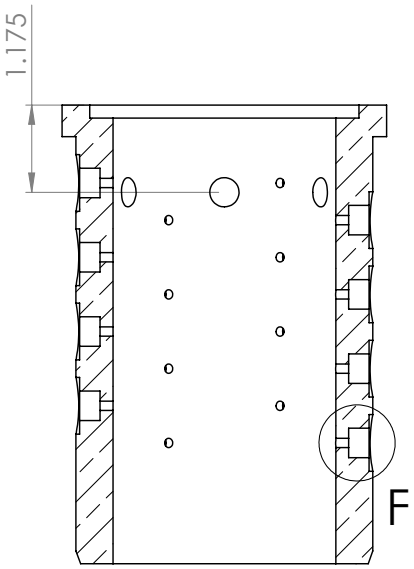

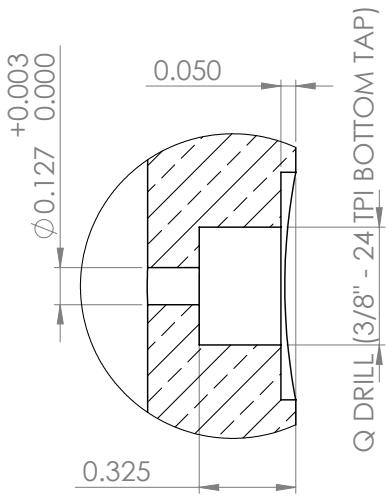

DETAIL F

SCALE 2 : 1

		UNLESS OTHERWISE SPECIFIED:		NAME	DATE
		DIMENSIONS ARE IN INCHES BREAK ALL SHARP CORNERS TOLERANCES: ANGULAR: ± 1deg TWO PLACE DECIMAL ± 0.01" THREE PLACE DECIMAL ± 0.005"	DRAWN	JVK	10/22/18
			CHECKED		
			ENG APPR.		
			MFG APPR.		
		INTERPRET GEOMETRIC TOLERANCING PER:	Q.A.		
		MATERIAL C10100 - OFHC	COMMENTS:		
NEXT ASSY	USED ON	FINISH			
APPLICATION		DO NOT SCALE DRAWING			

ROTATING DETONATION ENGINE

TITLE:

Sleeve

SIZE	DWG. NO.	REV
A	207	01
SCALE: 1:2	WEIGHT:	SHEET 2 OF 2

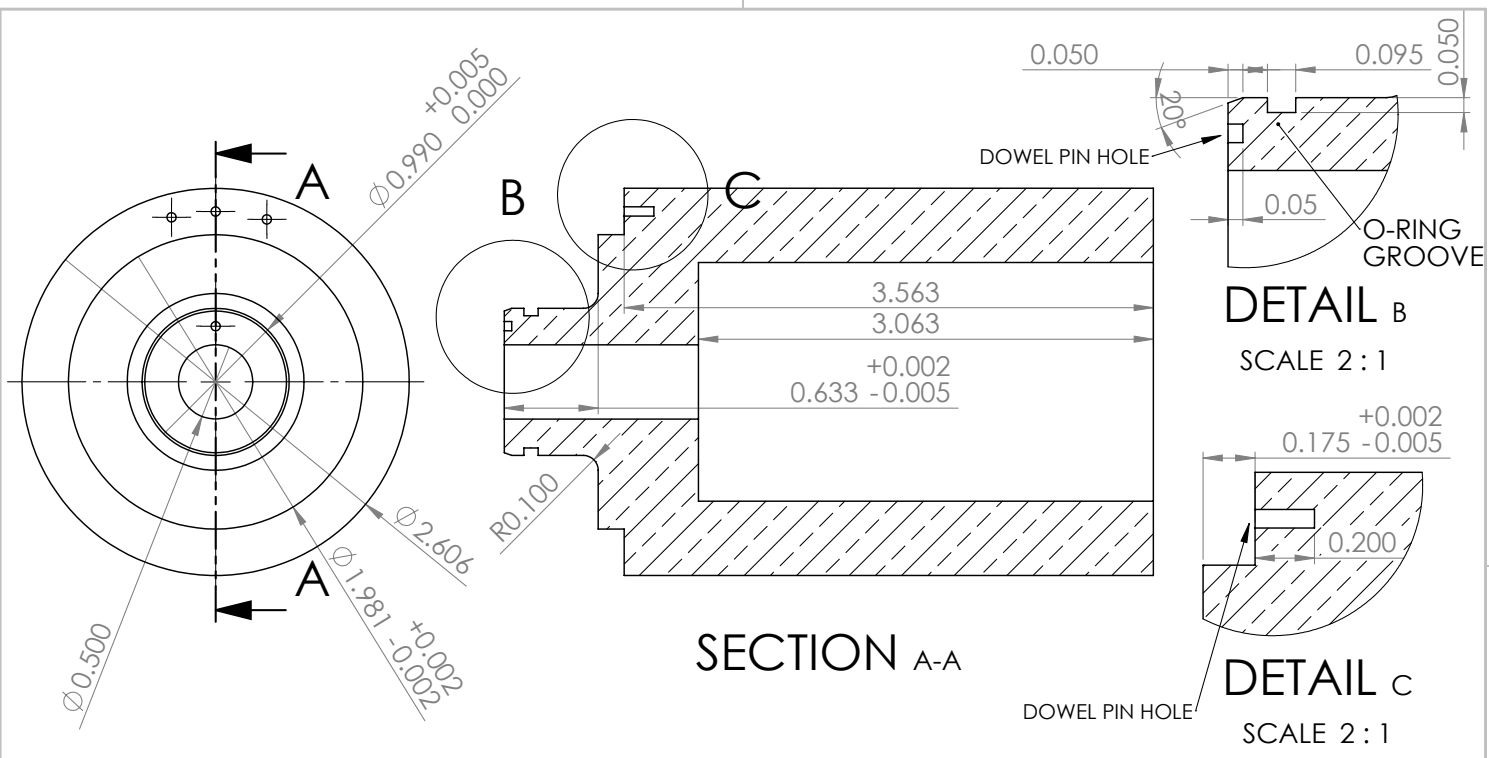

		UNLESS OTHERWISE SPECIFIED:		NAME	DATE	ROTATING DETONATION ENGINE
		DIMENSIONS ARE IN INCHES BREAK ALL SHARP CORNERS TOLERANCES: ANGULAR: ± 1deg TWO PLACE DECIMAL ± 0.01" THREE PLACE DECIMAL ± 0.005"	DRAWN	JVK	10/22/18	TITLE: Core
			CHECKED			
			ENG APPR.			
			MFG APPR.			
		INTERPRET GEOMETRIC TOLERANCING PER:	Q.A.			
		MATERIAL C10100 - OFHC	COMMENTS:			SIZE A | DWG. NO. 208 | REV 01
NEXT ASSY	USED ON	FINISH				
APPLICATION		DO NOT SCALE DRAWING				SCALE: 1:1 | WEIGHT: | SHEET 1 OF 2

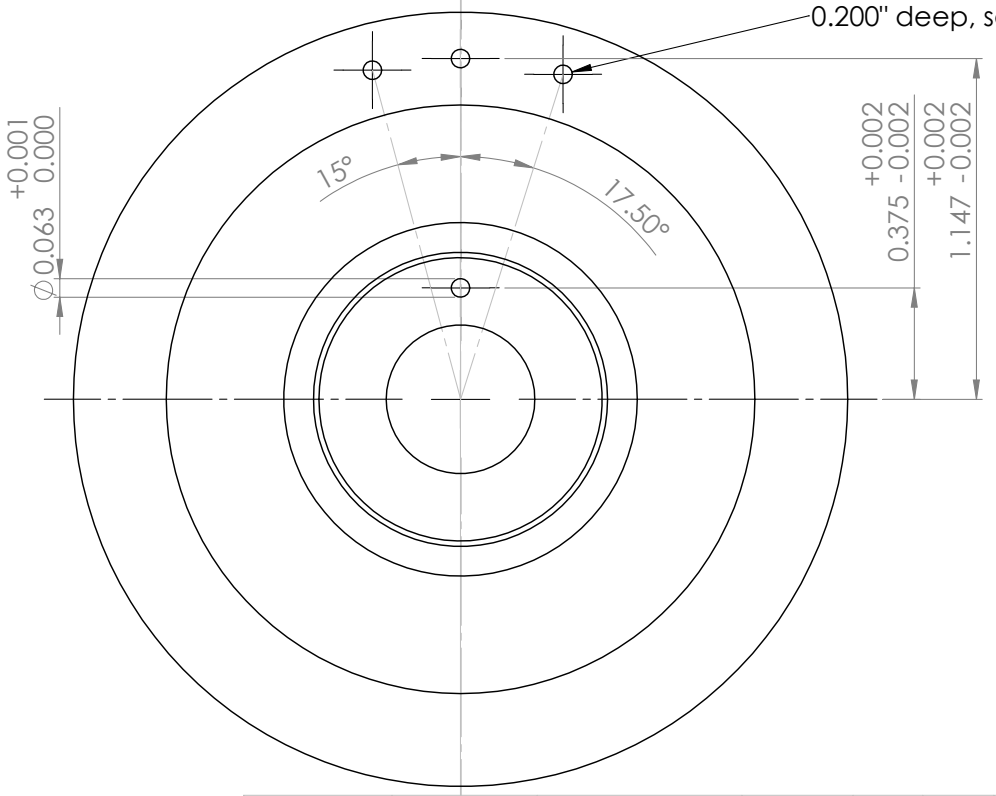

		UNLESS OTHERWISE SPECIFIED:		NAME	DATE
		DIMENSIONS ARE IN INCHES BREAK ALL SHARP CORNERS TOLERANCES: ANGULAR: ± 1deg TWO PLACE DECIMAL ± 0.01" THREE PLACE DECIMAL ± 0.005"	DRAWN	JVK	10/22/18
			CHECKED		
			ENG APPR.		
			MFG APPR.		
		INTERPRET GEOMETRIC TOLERANCING PER:	Q.A.		
		MATERIAL C10100 - OFHC	COMMENTS:		
NEXT ASSY	USED ON	FINISH			
APPLICATION		DO NOT SCALE DRAWING			

ROTATING DETONATION ENGINE

TITLE:

Core

SIZE	DWG. NO.	REV
A	208	01

SCALE: 2:1	WEIGHT:	SHEET 2 OF 2

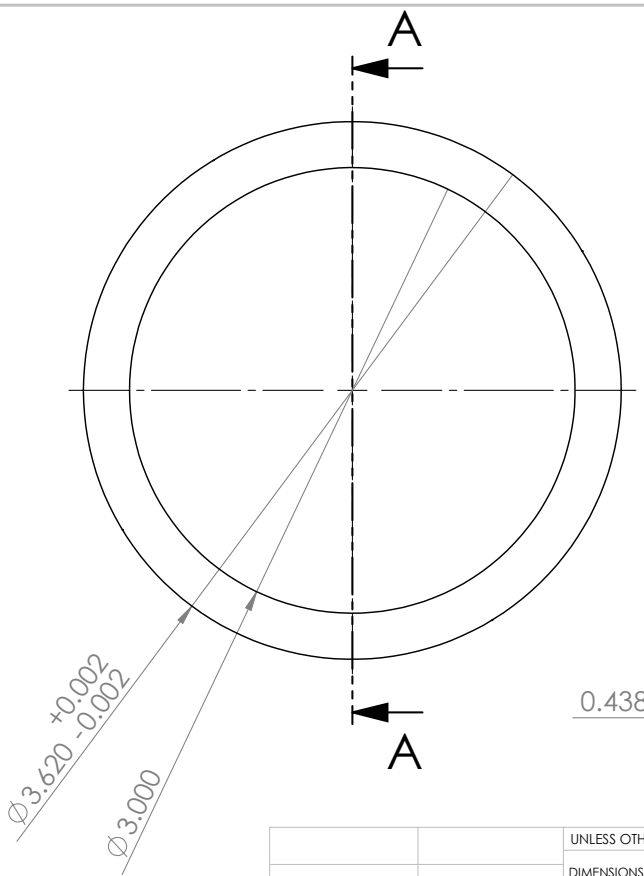

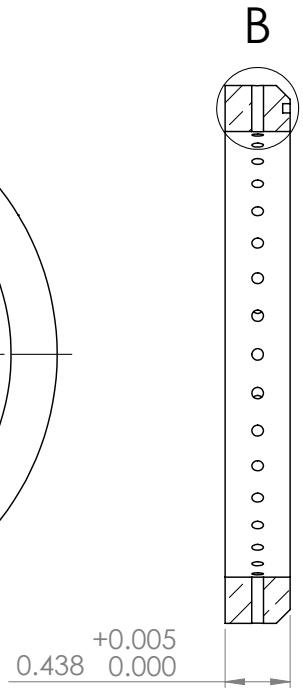

SECTION A-A

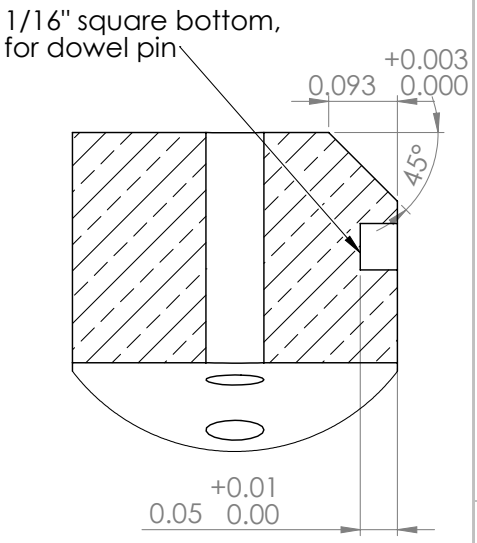

DETAIL B

SCALE 5 : 1

		UNLESS OTHERWISE SPECIFIED:		NAME	DATE
		DIMENSIONS ARE IN INCHES BREAK ALL SHARP CORNERS TOLERANCES: ANGULAR: ± 1deg TWO PLACE DECIMAL ± 0.01" THREE PLACE DECIMAL ± 0.005"	DRAWN	JVK	10/22/18
			CHECKED		
			ENG APPR.		
			MFG APPR.		
		INTERPRET GEOMETRIC TOLERANCING PER:	Q.A.		
		MATERIAL C10100 - OFHC	COMMENTS:		
NEXT ASSY	USED ON	FINISH			
APPLICATION		DO NOT SCALE DRAWING			

ROTATING DETONATION ENGINE

TITLE:

Oxidizer Injection Ring

SIZE	DWG. NO.	REV
A	209	01
SCALE: 1:1	WEIGHT:	SHEET 1 OF 2

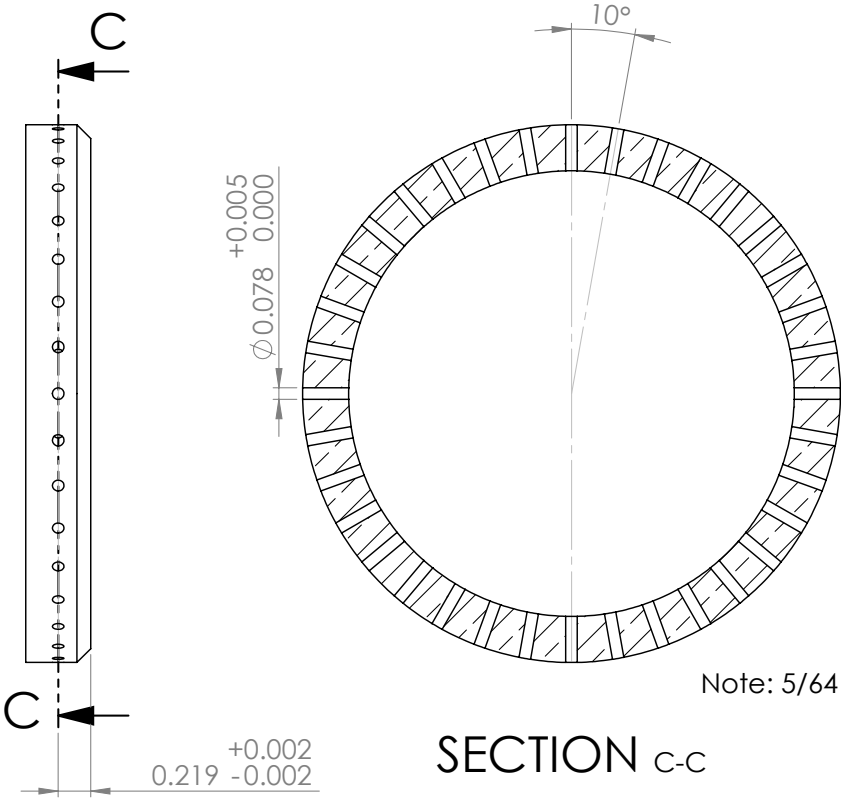

Note: 5/64 drill on orifices is OK

SECTION C-C

		UNLESS OTHERWISE SPECIFIED:		NAME	DATE
		DIMENSIONS ARE IN INCHES BREAK ALL SHARP CORNERS TOLERANCES: ANGULAR: ± 1deg TWO PLACE DECIMAL ± 0.01" THREE PLACE DECIMAL ± 0.005"	DRAWN	JVK	10/22/18
			CHECKED		
			ENG APPR.		
			MFG APPR.		
		INTERPRET GEOMETRIC TOLERANCING PER:	Q.A.		
		MATERIAL C10100 - OFHC	COMMENTS:		
NEXT ASSY	USED ON	FINISH			
APPLICATION		DO NOT SCALE DRAWING			

ROTATING DETONATION ENGINE

TITLE:

Oxidizer Injection Ring

SIZE	DWG. NO.	REV
A	209	01

SCALE: 1:1	WEIGHT:	SHEET 2 OF 2

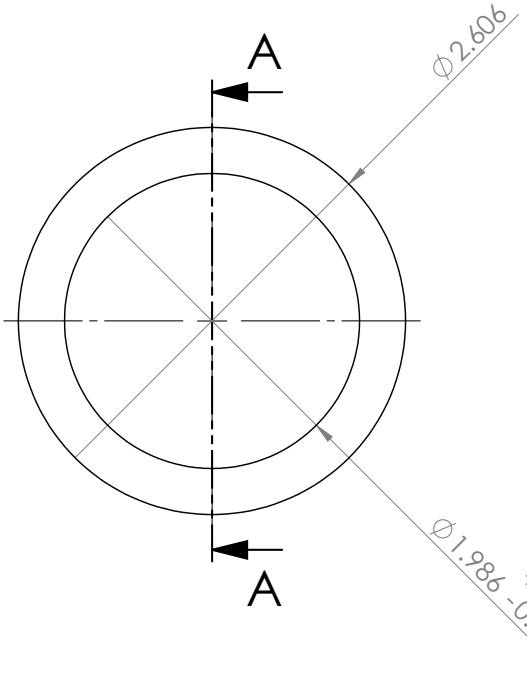

SECTION A-A

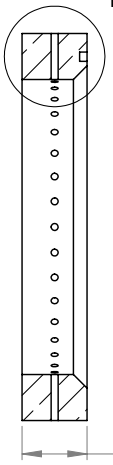

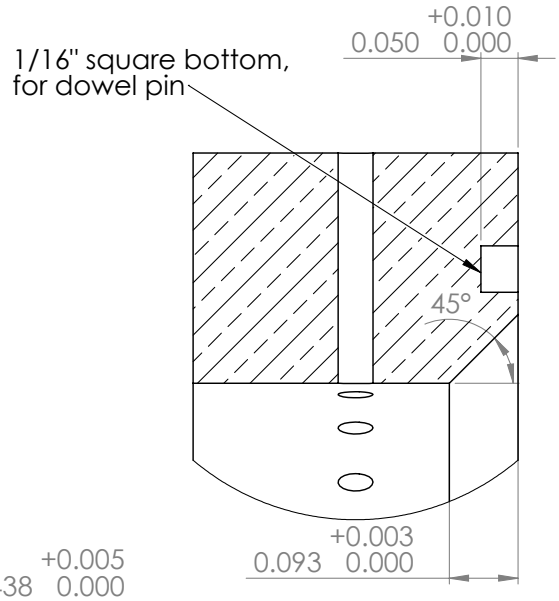

DETAIL B

SCALE 5 : 1

		UNLESS OTHERWISE SPECIFIED:		NAME	DATE
		DIMENSIONS ARE IN INCHES BREAK ALL SHARP CORNERS TOLERANCES: ANGULAR: ± 1deg TWO PLACE DECIMAL ± 0.01" THREE PLACE DECIMAL ± 0.005"	DRAWN	JVK	10/22/18
			CHECKED		
			ENG APPR.		
			MFG APPR.		
		INTERPRET GEOMETRIC TOLERANCING PER:	Q.A.		
		MATERIAL C10100 - OFHC	COMMENTS:		
NEXT ASSY	USED ON	FINISH			
APPLICATION		DO NOT SCALE DRAWING			

ROTATING DETONATION ENGINE

TITLE:

Fuel Injection Ring

SIZE	DWG. NO.	REV
A	210	01
SCALE: 1:1	WEIGHT:	SHEET 1 OF 2

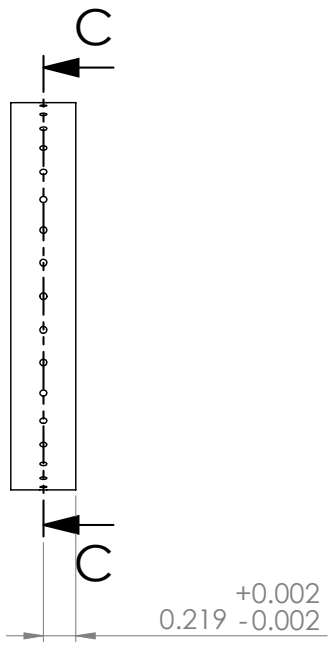

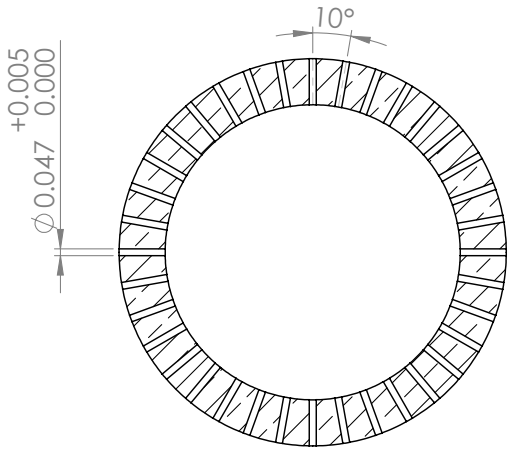

SECTION C-C

Note: 3/64" drill OK for orifices

		UNLESS OTHERWISE SPECIFIED:		NAME	DATE
		DIMENSIONS ARE IN INCHES BREAK ALL SHARP CORNERS TOLERANCES: ANGULAR: ± 1deg TWO PLACE DECIMAL ± 0.01" THREE PLACE DECIMAL ± 0.005"	DRAWN	JVK	10/22/18
			CHECKED		
			ENG APPR.		
			MFG APPR.		
		INTERPRET GEOMETRIC TOLERANCING PER:	Q.A.		
		MATERIAL C10100 - OFHC	COMMENTS:		
NEXT ASSY	USED ON	FINISH			
APPLICATION		DO NOT SCALE DRAWING			

ROTATING DETONATION ENGINE

TITLE:

Fuel Injection Ring

SIZE	DWG. NO.	REV
A	210	01

SCALE: 1:1	WEIGHT:	SHEET 2 OF 2

A.2 Impinging Injector

The 72-element impinging injector design is adapted from that of the United Stated Air Force Reesarch Laboratory. The injector was designed to undergo two major machining steps so that the injector could be manufactured out of a single piece of brass. The first step leaves a 'v'-groove in the injector where the sides of the groove are tangent to the injection orifices. This facilitates drilling the orifices without specialized tooling. The second step removes the 'v'-groove and leaves the injector face flat.

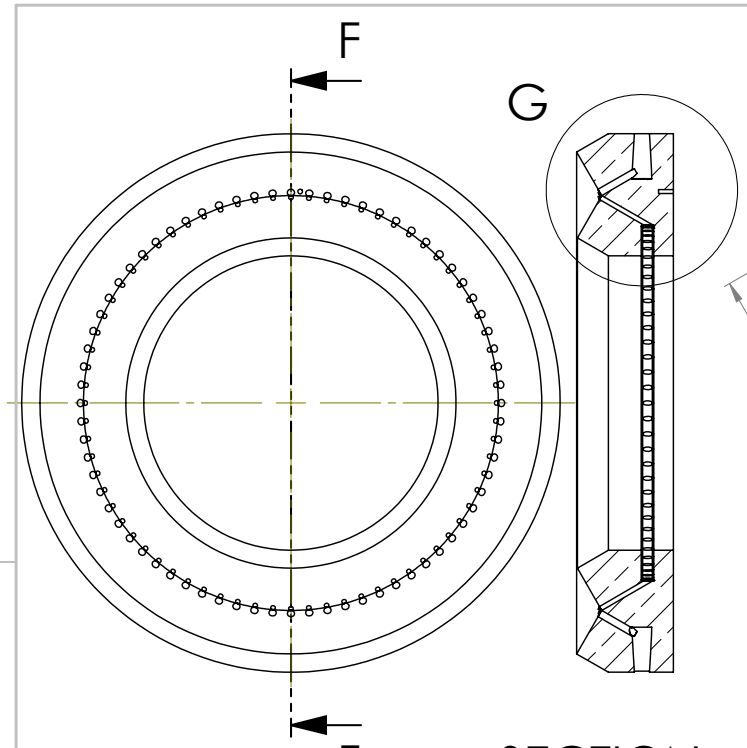

SECTION F-F

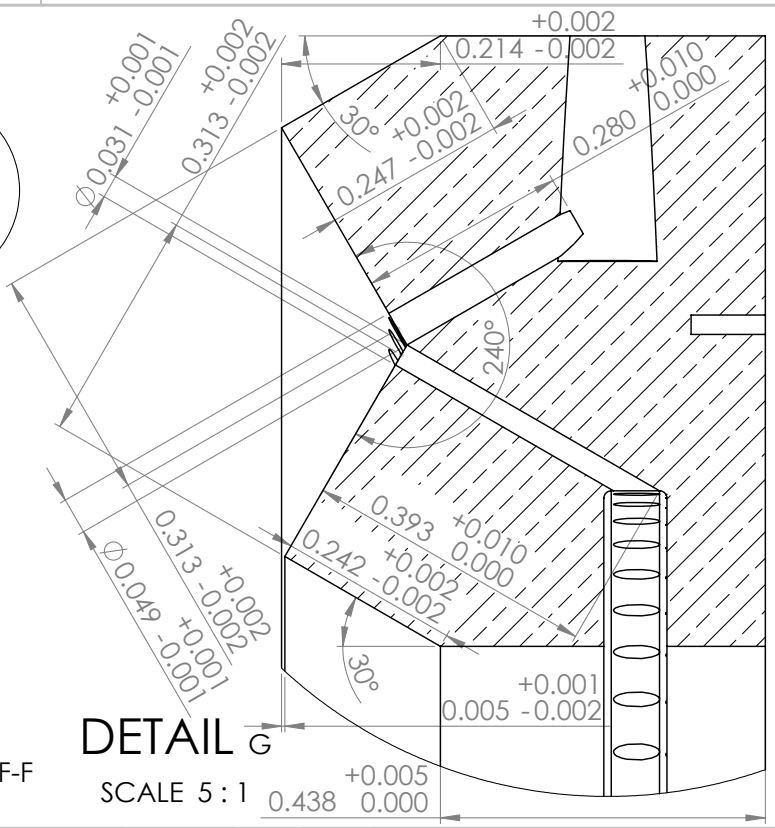

DETAIL G

SCALE 5 : 1

		UNLESS OTHERWISE SPECIFIED:		NAME	DATE
		DIMENSIONS ARE IN INCHES TOLERANCES: ANGULAR: ± 1deg TWO PLACE DECIMAL ± 0.01" THREE PLACE DECIMAL ± 0.005"	DRAWN		
			CHECKED		
			ENG APPR.		
			MFG APPR.		
		INTERPRET GEOMETRIC TOLERANCING PER:	Q.A.		
		MATERIAL C360	COMMENTS:		
NEXT ASSY	USED ON	FINISH			
APPLICATION		DO NOT SCALE DRAWING			

ROTATING DETONATION ENGINE

TITLE:

Impinging Injector

SIZE	DWG. NO.	REV
A	211	03

SCALE: 1:1	WEIGHT:	SHEET 1 OF 4

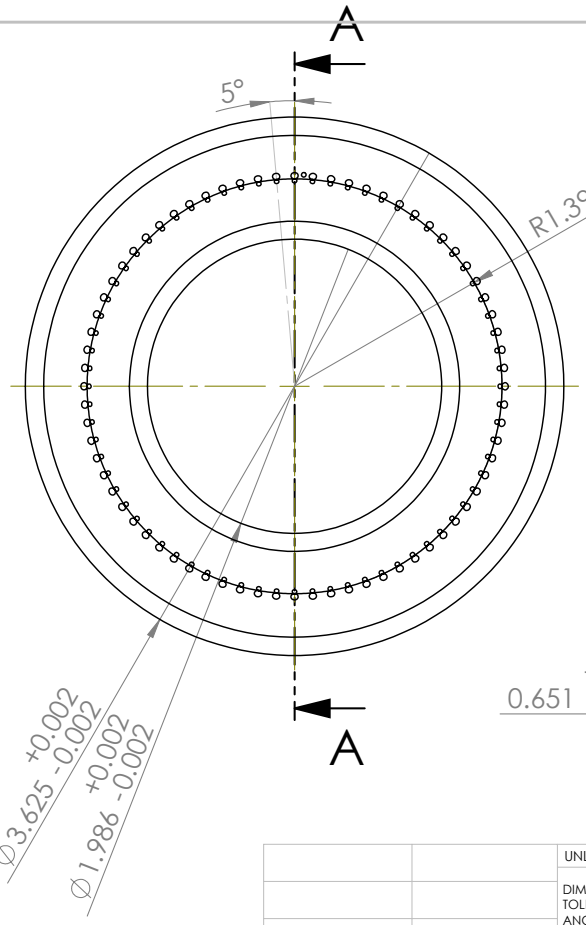

SECTION A-A

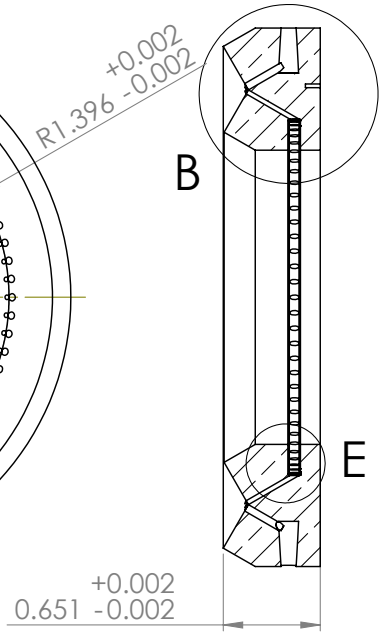

DETAIL B

SCALE 2 : 1

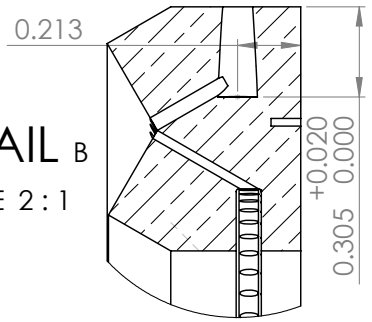

DETAIL E

SCALE 5 : 1

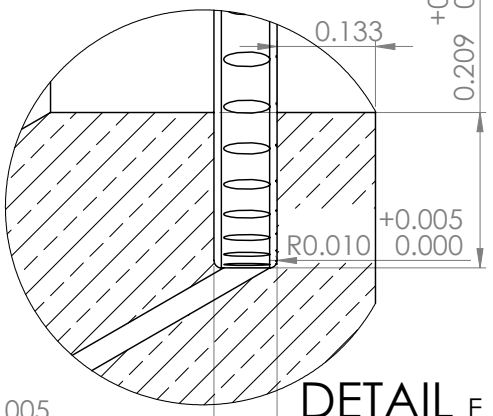

		UNLESS OTHERWISE SPECIFIED:		NAME	DATE
		DIMENSIONS ARE IN INCHES TOLERANCES: ANGULAR: ± 1deg TWO PLACE DECIMAL ± 0.01" THREE PLACE DECIMAL ± 0.005"	DRAWN		
			CHECKED		
			ENG APPR.		
			MFG APPR.		
		INTERPRET GEOMETRIC TOLERANCING PER:	Q.A.		
		MATERIAL C360	COMMENTS:		
NEXT ASSY	USED ON	FINISH			
APPLICATION		DO NOT SCALE DRAWING			

ROTATING DETONATION ENGINE

TITLE:

Impinging Injector

SIZE	DWG. NO.	REV
A	211	03

SCALE: 1:1	WEIGHT:	SHEET 2 OF 4

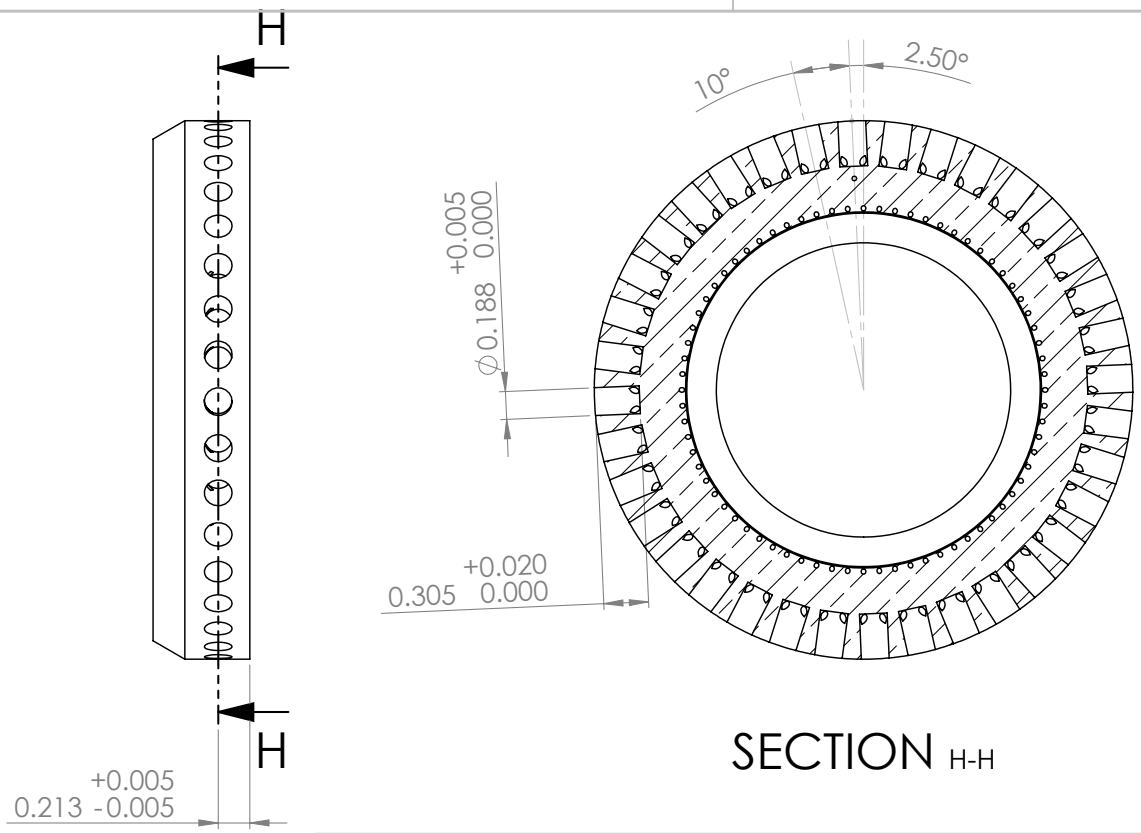

SECTION H-H

		UNLESS OTHERWISE SPECIFIED:		NAME	DATE
		DIMENSIONS ARE IN INCHES TOLERANCES: ANGULAR: ± 1deg TWO PLACE DECIMAL ±0.01" THREE PLACE DECIMAL ±0.005"	DRAWN		
			CHECKED		
			ENG APPR.		
			MFG APPR.		
		INTERPRET GEOMETRIC TOLERANCING PER:	Q.A.		
		MATERIAL C360	COMMENTS:		
NEXT ASSY	USED ON	FINISH			
APPLICATION		DO NOT SCALE DRAWING			

ROTATING DETONATION ENGINE

TITLE:

Impinging Injector

SIZE	DWG. NO.	REV
A	211	03

SCALE: 1:1	WEIGHT:	SHEET 3 OF 4

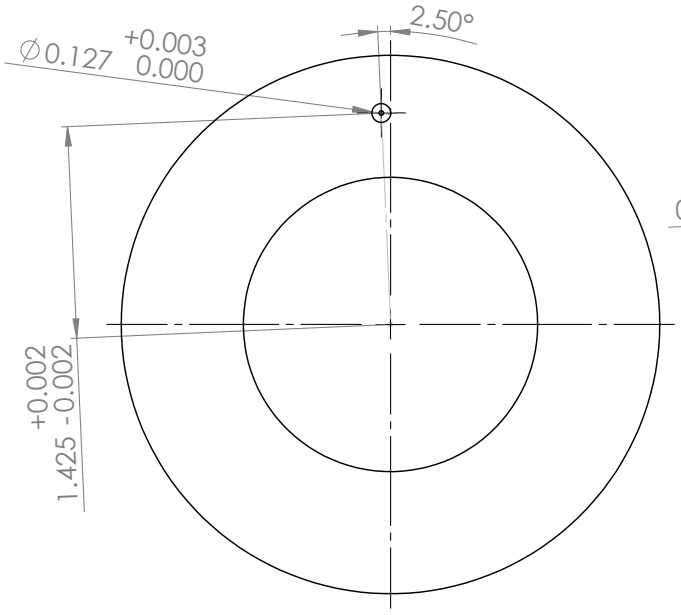

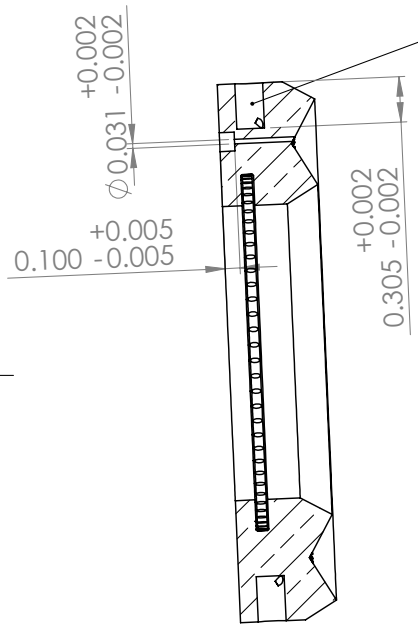

Sqare hole required for only this radial 3/16" port aso as to not penetrate into instrument port.

SECTION I-I

		UNLESS OTHERWISE SPECIFIED:		NAME	DATE
		DIMENSIONS ARE IN INCHES TOLERANCES: FRACTIONAL ± ANGULAR: MACH ± BEND ± TWO PLACE DECIMAL ± THREE PLACE DECIMAL ±	DRAWN		
			CHECKED		
			ENG APPR.		
			MFG APPR.		
		INTERPRET GEOMETRIC TOLERANCING PER:	Q.A.		
		MATERIAL	COMMENTS:		
NEXT ASSY	USED ON	FINISH			
APPLICATION		DO NOT SCALE DRAWING			

ROTATING DETONATION ENGINE

TITLE:

Impinging Injector

SIZE	DWG. NO.	REV
A	211	03

SCALE: 1:1	WEIGHT:	SHEET 4 OF 4

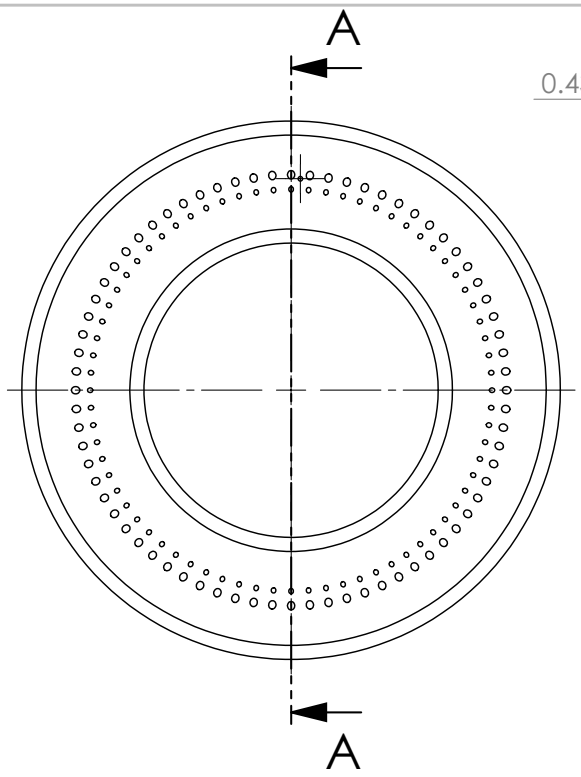

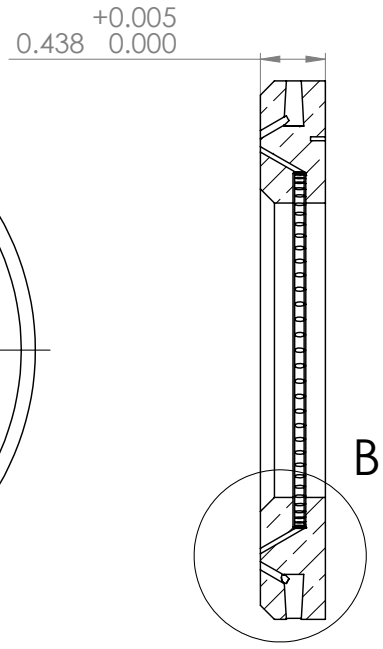

SECTION A-A

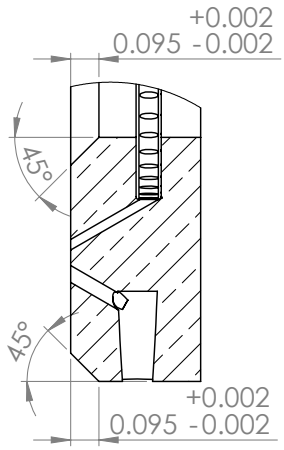

DETAIL B

SCALE 2 : 1

		UNLESS OTHERWISE SPECIFIED:		NAME	DATE
		DIMENSIONS ARE IN INCHES TOLERANCES: ANGULAR: ±1deg TWO PLACE DECIMAL ± 0.01" THREE PLACE DECIMAL ± 0.005"	DRAWN		
			CHECKED		
			ENG APPR.		
			MFG APPR.		
		INTERPRET GEOMETRIC TOLERANCING PER:	Q.A.		
		MATERIAL C360	COMMENTS:		
NEXT ASSY	USED ON	FINISH			
APPLICATION		DO NOT SCALE DRAWING			

ROTATING DETONATION ENGINE

TITLE:

Impinging Injector

SIZE	DWG. NO.	REV
A	212	03

SCALE: 1:1	WEIGHT:	SHEET 1 OF 1